

國立交通大學  
光電工程研究所  
博士論文

以增益開關法布里-珀羅雷射二極體為  
基礎的全光通訊信號格式轉換元件研究

All Optical NRZ-to-RZ Format Converter  
by a Fabry-Perot Semiconductor Laser  
Diode



研究生：張詠誠

指導教授：林恭如 教授

中華民國九十五年六月

以增益開關法布里-珀羅雷射二極體為  
基礎的全光通訊信號格式轉換元件研究

All Optical NRZ-to-RZ Format Converter  
by a Fabry-Perot Semiconductor Laser  
Diode

研究生：張詠誠  
指導教授：林恭如

Student: Yung-Cheng Chang  
Advisor: Gong-Ru Lin



國立交通大學 電機資訊學院  
光電工程研究所  
博士論文

A Dissertation  
Submitted in Partial Fulfillment of the Requirements  
for the Degree of Doctor of Philosophy in  
The Institute of Electro-Optical Engineering  
College of Electrical Engineering and Computer Science  
National Chiao-Tung University  
Hsin-Chu, Taiwan, R.O.C.

中華民國九十五年六月

# 摘 要

論文名稱：以增益開關法布里-珀羅雷射二極體為基礎的全光通訊信號格式轉換元件  
研究

校所別：國立交通大學光電工程研究所

頁數：1 頁

畢業時間：九十四學年度第二學期

學位：博士

研究生：張詠誠

指導教授：林恭如 教授

關鍵詞：法布里-珀羅雷射二極體, NRZ-to-RZ 格式轉換, 光注入鎖定引起的閾值電流  
降低現象, 光纖通訊, 全光邏輯或閘, 啁啾

本論文的主旨在利用半導體雷射中光注入鎖定會造成雷射的閾值電流降低現象來實現一全光式非歸零轉歸零之格式轉換器。閾值電流在注入鎖定半導體雷射情況下所造成的閾值電流降低現象也做了詳細的理論推導。在實驗上，我們成功地展示全光非歸零轉歸零的格式轉換器，同時這種利用光注入鎖定的技術可以使法布里-珀羅雷射二極體同時具備單縱模輸出、啁啾降低與頻寬延展等好處。在應用上，以此種全光格式轉換器實現之全光或閘也首度被展示。進一步，我們評估輸出歸零光訊號的啁啾特性，並以日本 NTT 研究群所提出的動態光固子傳輸架構為基礎提出傳輸此格式轉換後的歸零訊號之傳輸架構。

# ABSTRACT

Title : All Optical NRZ-to-RZ Format Converter by a Fabry-Perot Semiconductor Laser Diode

Pages : 1 Page

School : National Chiao Tung University

Department : Institute of Electro-Optical Engineering

Time : June, 2006

Degree : Doctor of Philosophy

Researcher : Yung-Cheng Chang

Advisor : Prof. Gong-Ru Lin

Keywords : Fabry Perot laser diode, NRZ-to-RZ format conversion, optical injection-locking-induced threshold current reduction, fiber-optic communication, optical OR logic gate, chirp.

In this dissertation, a reduction in the threshold current of a Fabry-Perot laser diode (FPLD) is first used to convert a nonreturn-to-zero (NRZ) to return-to-zero (RZ) formatted data stream. The threshold current reduction in external injection locking condition is derived by using a phenomenological approach to diode lasers and Li's theory. Such a reduction in the threshold current by the injection locking technique can reduce the linewidth/chirping and enhance the modulation bandwidth of the FPLD. In applications, an NRZ-to-RZ-based all-optical OR logic gate is also demonstrated. Furthermore, by using a spectral windowing, linear dispersion compensation, and a preemphasis technique we believe that a soliton transmission for the RZ-formatted data stream may be expected.

# Acknowledgements

博士論文終於完成了。首先要特別對我的指導教授 林恭如 老師在研究的過程中不斷的給予支持與耐心的指導表達敬意與感謝之意，使我在求學態度受益良多。

感謝實驗室歷年學弟士雄、世剴、忠嶸、百勝、鈺晃、銘忠、奕祥、齊冠、家陽、昆潔與博士班同學俊榮、育聖的陪伴。天下無不散之宴席，我終於要離開這個實驗室了，期盼接下來的實驗室環境會更好，有更多的研究成果以及積極的研究風氣。最後我要感謝我最摯愛的家人，尤其是在背後默默支持我的爺爺、爸爸、媽媽、弟弟、妹妹、叔叔、嬸嬸、姑姑、姑丈等，以及我的女友佩誼及其他關心我的好朋友，對於你們長期以來的支持與關愛，在此獻上誠摯的感謝。



# CONTENTS

	Page
<b>Chinese Abstract</b>	<b>I</b>
<b>English Abstract</b>	<b>II</b>
<b>Acknowledgements</b>	<b>III</b>
<b>Contents</b>	<b>IV</b>
<b>List of Figures</b>	<b>VII</b>
<b>List of Tables</b>	<b>XII</b>
<b>Chapter 1</b>	<b>1</b>
<b>Introduction</b>	
<b>1.1 Introduction of Semiconductor Lasers</b>	<b>1</b>
<b>1.1.1 Historical Review of Semiconductor Lasers</b>	<b>1</b>
<b>1.1.2 Operating Principles of Semiconductor Lasers</b>	<b>5</b>
◆ <b>p-n Junction</b>	<b>5</b>
◆ <b>Dielectric Waveguide</b>	<b>7</b>
◆ <b>Recombination Mechanisms</b>	<b>8</b>
◆ <b>Laser Threshold</b>	<b>8</b>
<b>1.2 Enabling Technology for Data Format Conversion</b>	<b>10</b>
<b>1.2.1 All-optical Non-Return-to-Zero (NRZ) to Return-to-Zero (RZ) Data Format Conversion by using Fabry-Perot laser diodes (FPLDs)</b>	<b>11</b>
<b>1.2.2 Techniques for Generating Short Pulse</b>	<b>12</b>
<b>1.2.3 Introduction of Injection Locking</b>	<b>14</b>
<b>1.3 Motivation of an novel FPLD-based NRZ-to-RZ Data Format Converter</b>	<b>15</b>
<b>1.4 Organization of Dissertation</b>	<b>16</b>
<b>Figures</b>	<b>18</b>
<b>Chapter 2</b>	<b>27</b>
<b>Theory of Threshold Current Reduction under External Light Injection Locking</b>	
<b>2.1 Introduction</b>	<b>27</b>
<b>2.2 A Phenomenological Approach to Diode Lasers</b>	<b>29</b>
<b>2.2.1 Carrier Generation and Recombination in Active Region</b>	<b>30</b>

2.2.2 Spontaneous Photon Generation in LEDs	33
2.2.3 Photon Generation and Loss in Laser Cavities	36
2.2.4 Threshold or Steady-State Gain in Lasers	39
2.2.5 Threshold Current and Output Power vs. Current	43
2.2.6 Relaxation Resonance and Frequency Response	50
2.3 Threshold Current Reduction Under External Light Injection	55
Table	64
Figures	65
<b>Chapter 3</b>	<b>72</b>
<b>All-optical NRZ-to-RZ Data Format Converter with An Injection-locked Fabry-Perot Laser Diode in Unlasing Condition</b>	
Abstract	72
3.1 Introduction	72
3.2 Operating Principle of Injection-locking-induced gain-switching in a Synchronously-modulated FPLD just below Threshold Current	73
3.3 Experimental Setup and Results	74
3.3.1 Threshold Current Reduction under External Injection Locking	74
3.3.2 Injection-locking-induced Gain Switching	75
3.3.3 FPLD-based All-optical NRZ-to-PRZ Data Format Converter	78
Table	83
Figures	84
<b>Chapter 4</b>	<b>100</b>
<b>Injection-locking Laser Diode based OC-192 optical NRZ-to-RZ OR Logic Gate</b>	
Abstract	100
4.1 Introduction	100
4.2 FPLD-based All-optical NRZ-to-RZ OR logic gate	101
Figures	104
<b>Chapter 5</b>	<b>107</b>
<b>Dynamic Chirp Characteristics in FPLD-based All-optical NRZ-to-RZ Data Format Converter</b>	
Abstract	107

<b>5.1 Introduction</b>	<b>107</b>
<b>5.2 Evaluation of Chirp in FPLD-based NRZ-to-RZ Data Format Converter</b>	<b>109</b>
<b>5.3 Results and Discussion</b>	<b>111</b>
<b>Table</b>	<b>114</b>
<b>Figures</b>	<b>115</b>
<b>Chapter 6</b>	<b>122</b>
<b>Conclusions</b>	
<b>6.1 Summary</b>	<b>122</b>
<b>6.2 Suggestions for Future Work</b>	<b>124</b>
<b>References</b>	<b>125</b>
<b>Curriculum Vitae</b>	
<b>Publication List</b>	





## List of Figures

- Fig. 1.1 Schematic illustration of (a) homostructure and (b) double-heterostructure semiconductor lasers with their typical physical dimensions. The dotted area represents the depletion region in the vicinity of the homojunction. The hatched area shows the thin ( $\sim 0.2 \mu\text{m}$ ) active layer of a semiconductor material whose band gap is slightly lower than that of the surrounding cladding layers. [G. P. Agrawal, and N. K. Dutta, *Long-wavelength Semiconductor Lasers*, New York: Van Nostrand Reinhold, 1986.]
- Fig. 1.2 Schematic illustration of the simultaneous confinement of the charge carriers and the optical mode to the active region occurring in a double-heterostructure semiconductor laser. The active layer has a lower band gap and a higher refractive index than those of the cladding layers. [H. C. Casey, Jr., and M. B. Panish. *Heterostructure Lasers*, Parts A and B. New York: Academic Press, 1978.]
- Fig. 1.3 Basic  $p^+nn^+$  laser structure showing the stripe geometry contact which confines the active portion of the junction to a narrow region. The xyz axes are also defined. [J. C. Dymont, "Hermite-gaussian Mode Patterns in GaAs Junction Lasers," *Appl. Phys. Lett.* **10**, 84 (1967).]
- Fig. 1.4 Two types of diode lasers with strong transverse confinement: (a) a gain-guided laser with poor lateral confinement; (b) an index-guided laser for strong lateral confinement. The current flow is laterally restricted by a strip of width  $w$ . [Peter Vasil'ev, *Ultrafast Diode Lasers: Fundamentals and Applications*, Boston: Artech House Publishers, 1995]
- Fig. 1.5 Energy-band diagram of a  $p$ - $n$  junction at (a) zero bias and (b) forward bias. (c) Schematic representation of the electron and hole densities under forward bias. Radiative recombination of electrons and holes in the narrow overlapping region generates light. [G. P. Agrawal, and N. K. Dutta, *Long-wavelength Semiconductor Lasers*, New York: Van Nostrand Reinhold, 1986.]
- Fig. 1.6 Energy-band diagram of a double-heterostructure semiconductor laser at (a) zero bias and (b) forward bias. (c) The band-gap discontinuities at the two heterojunctions help to confine electrons and holes inside the active region, where they recombine to produce light. [G. P. Agrawal, and N. K. Dutta, *Long-wavelength Semiconductor Lasers*, New York: Van Nostrand Reinhold, 1986.]
- Fig. 1.7 Dielectric waveguiding in a heterostructure semiconductor laser. The relatively

higher refractive index ( $\mu_2 > \mu_1$ ) of the active layer allows total internal reflection to occur at the two interfaces for angles such that  $\sin \theta > \mu_1/\mu_2$ .

[G. P. Agrawal, and N. K. Dutta, *Long-wavelength Semiconductor Lasers*, New York: Van Nostrand Reinhold, 1986.]

Fig. 1.8 Schematic illustration of (a) spontaneous-emission and (b) stimulated-emission processes wherein an electron-hole pair recombines to generate a photon. In the case of stimulated emission the two outgoing photons match in their frequency and direction of propagation.

[G. P. Agrawal, and N. K. Dutta, *Long-wavelength Semiconductor Lasers*, New York: Van Nostrand Reinhold, 1986.]

Fig. 1.9 Experimental setup. PC: polarization controller; SMF: single mode fiber; APD: avalanche photodiode; EDFA: erbium-doped fiber amplifier; BERT: bit-error tester.

[C. W. Chow, C. S. Wong, H. K. Tsang, "All-optical NRZ to RZ format and wavelength converter by dual-wavelength injection locking," *Opt. Commun.* **209**, 329 (2002).]

Fig. 1.10 Experimental setup for NRZ-to-PRZ converter; EDFA: erbium-doped fiber amplifier; PC: polarization controller; OBF: optical bandpass filter; PBS: polarization beam splitter.

[Y. D. Jeong, H. J. Lee, H. Yoo, and Y. H. Won, "All-optical NRZ-to-PRZ converter at 10 Gb/s based on self-phase modulation of Fabry-Perot laser diode," *IEEE Photon. Technol. Lett.* **16**, 1179 (2004).]

Fig. 1.11 Experimental setup. The gain-switched DFB3 is used to manipulate the gain in SOA1 and SOA2.

[J. P. R. Lacey, M. V. Chan, R. S. Tucker, A. J. Lowery and M. A. Summerfield, "All-optical WDM to TDM transmultiplexer," *Electron. Lett.* **30**, 1612 (1994).]

Fig. 1.12 (a) All-optical WDM-to-TDM node incorporating the modular functions of: (1) NRZ-to-RZ conversion; (2) extinction ratio enhancement; and (3) wavelength shifting. (b) Conceptual operation of the WDM-to-TDM node.

[D. Norte and A. E. Willner, "Demonstration of an all-optical data format transparent WDM-to-TDM network node with extinction ratio enhancement for reconfigurable WDM networks," *IEEE Photon. Technol. Lett.* **8**, 715 (1996).]

Fig. 2.1 Light-current graph for free running, injected locked laser and the difference of the two.

[S. Sivaprakasam and Ranjit Singh, "Gain change and threshold reduction of diode laser by injection locking," *Optics Communications*, **151**, 253 (1998).]

Fig. 2.2 Electronic transitions between the conduction and valence bands. The first

three (a-c) represent radiative transitions in which the energy to free or bind an electron is supplied by or given to a photon. The fourth illustrates two nonradiative processes.

[L. A. Coldren, and S. W. Corzine, *Diode Lasers and Photonic Integrated Circuits*, New York: Wiley Interscience, 1995.]

Fig. 2.3 Band diagram of forward biased double-heterostructure diode.

[L. A. Coldren, and S. W. Corzine, *Diode Lasers and Photonic Integrated Circuits*, New York: Wiley Interscience, 1995.]

Fig. 2.4 Reservoir with continuous supply and leakage as an analog to a DH active region with current injection for carrier generation and radiative and nonradiative recombination (LED or laser below threshold).

[L. A. Coldren, and S. W. Corzine, *Diode Lasers and Photonic Integrated Circuits*, New York: Wiley Interscience, 1995.]

Fig. 2.5 Schematics of in-plane and vertical-cavity lasers illustrating the active (cross-hatched) and cavity (within dashed lines) volume as well as the coordinate systems.

[L. A. Coldren, and S. W. Corzine, *Diode Lasers and Photonic Integrated Circuits*, New York: Wiley Interscience, 1995.]

Fig. 2.6 Schematic of LED showing how only a small portion of the generated light reaches a desired detector.

[L. A. Coldren, and S. W. Corzine, *Diode Lasers and Photonic Integrated Circuits*, New York: Wiley Interscience, 1995.]

Fig. 2.7 Definition of gain in terms of the increase in photon number across a small segment of gain material.

Fig. 2.8 Maximum gain  $g_{\max}$  and gain at a specific photon energy.

[K. Petermann, *Laser Diode Modulation and Noise*, 1991]

Fig. 2.9 Generic laser cavity cross section showing active and passive sections and the guided-mode profile.

[L. A. Coldren, and S. W. Corzine, *Diode Lasers and Photonic Integrated Circuits*, New York: Wiley Interscience, 1995.]

Fig. 2.10 Reservoir analogy above threshold where water level has risen to the spillway so that an increased input results in an increased output ( $R_{st}$ ) but no increase in carrier density (water level). The flows  $R_{nr}$  and  $R_{sp}$  do not change above threshold.

[L. A. Coldren, and S. W. Corzine, *Diode Lasers and Photonic Integrated Circuits*, New York: Wiley Interscience, 1995.]

Fig. 2.11 Gain vs. carrier density and carrier density vs. input current. The carrier density clamps at threshold causing the gain to clamp also.

[L. A. Coldren, and S. W. Corzine, *Diode Lasers and Photonic Integrated Circuits*, New York: Wiley Interscience, 1995.]

Fig. 2.12 Illustration of output power vs. current for a diode laser. Below threshold only spontaneous emission is important; above threshold the stimulated emission power increases while the spontaneous emission is clamped at its threshold value.

[L. A. Coldren, and S. W. Corzine, *Diode Lasers and Photonic Integrated Circuits*, New York: Wiley Interscience, 1995.]

Fig. 2.13 Schematic illustration of modal gain versus injected carrier density with values labeled from the two-parameter logarithmic fit of Eq. (2.41).

[L. A. Coldren, and S. W. Corzine, *Diode Lasers and Photonic Integrated Circuits*, New York: Wiley Interscience, 1995.]

Fig. 2.14 Frequency response of an idealized diode laser for several different output powers.

[L. A. Coldren, and S. W. Corzine, *Diode Lasers and Photonic Integrated Circuits*, New York: Wiley Interscience, 1995.]

Fig. 3.1 The principle of gain switching. (a) The time dependence of the applied current; (b) The time dependence of the carrier density; (c) The time dependence of output pulses.

Fig. 3.2 (a) The 'general' gain-switching; (b) The injection-locking-induced gain-switching: (A) without external injection; (B) with external injection.

Fig. 3.3 Experimental setup for the observation of the power-current curve with and without external light injection locking. FPLD: Fabry-Perot laser diode; OC: optical circulator; TEC: thermoelectric cooler controller; TL: tunable laser.

Fig. 3.4 Light-current (L-I) curves with and without external light injection locking.

Fig. 3.5 Experimental setup for injection-locking-induced gain-switching. AMP: RF amplifier; EDFA: erbium-doped fiber amplifier; FPLD: Fabry-Perot laser diode; TL: tunable laser; OBPF: optical bandpass filter; OC: optical circulator.

Fig. 3.6 The injection-locking-induced gain switching. (a) with external injection; (b) without external injection.

Fig. 3.7 Wavelength detuning of the tunable laser from one longitudinal mode to another.

Fig. 3.8 Temporal traces versus the detuning range.

Fig. 3.9 The injection-locking-induced pulse: (a) with injection locking at wavelength  $\lambda$ ; (b) with injection locking at wavelength  $\lambda + 0.6$  nm; (c) without injection. The repetition rate of the pulse train is 1 GHz.

Fig. 3.10 Optical spectra of the FPLD modulated by a large sinusoidal signal at just below threshold: (a) injection locking; (b) injection with detuned

wavelength,  $\lambda + 0.6$  nm; (c) without injection. It is noted that the red peak in trace (b) is the signal of the external injection light. The FPLD is not locked in this condition.

- Fig. 3.11 Optical spectra: (a) modulated FPLD; (b) CW tunable laser; (c) CW FPLD injection-locked FPLD.
- Fig. 3.12 The extinction ratio of the injection-locked FPLD at different RF driving and external injection power.
- Fig. 3.13 The peak power and the SMSR of the single-mode gain-switched FPLD in injection-locking condition.
- Fig. 3.14 The SSB phase noise density and the associated timing jitter of the injection-locking-induced pulses.
- Fig. 3.15 Timing jitter and pulsewidth versus external injection power.
- Fig. 3.16 Experimental setup for NRZ-to-RZ data format conversion. AMP: RF amplifier; EDFA: erbium-doped fiber amplifier; FPLD: Fabry-Perot laser diode; MZM: Mach-Zehnder intensity modulator; TL: tunable laser; OBPF: optical bandpass filter; OC: optical circulator; PG: pattern generator.
- Fig. 3.17 The characteristic transmission coefficient of MZM at different DC bias.
- Fig. 3.18 RZ data streams (a) without OBPF (b) with OBPF.
- Fig. 3.19 The patterns: (a) the electrical NRZ data before the MZM; (b) the PG-encoded optical NRZ data; (c) the transformed RZ signal generated from the single-mode FPLD. The data rate is 2.488 Gbit/s.
- Fig. 3.20 The corresponding eye diagrams: (a) the electrical NRZ data before the MZM; (b) the PG-encoded optical NRZ data; (c) the transformed RZ data. The data rate is 2.488 Gbit/s.
- Fig. 3.21 The BER performance at 2.488 Gbit/s.
- Fig. 3.22 The BER versus the external injection power.
- Fig. 3.23 The dependence of operation data rate on FPLD's DC bias current.
- Fig. 3.24 The patterns: (a) the electrical NRZ data before the MZM; (b) the PG-encoded external injection light; (c) the converted RZ signal generated from the injection-locked FPLD. The data rate is 9.953 Gbit/s.
- Fig. 3.25 The corresponding eye diagrams: (a) the electrical NRZ data before the MZM; (b) the PG-encoded external injection light; (c) the converted RZ signal generated from the single-mode FPLD. The data rate is 9.953 Gbit/s.
- Fig. 3.26 The BER against the received optical power for NRZ-encoded external injection light and converted RZ signal at data rate of 9.953 Gbit/s.
- Fig. 3.27 The BERs for different external injection powers at data rate of 9.953 Gbit/s.
- Fig. 4.1 Experimental setup and the truth table of the FPLD-based logic OR gate. AMP: rf amplifier; CDR: clock/data recovery unit; Ch1: input channel 1; Ch2: input

channel 2; EDFA: erbium-doped fiber amplifier; FPLD: Fabry-Perot laser diode; OBPF: optical bandpass filter; OC: optical coupler.

- Fig. 4.2 The monitored data patterns. (a) and (b): two input NRZ data-streams; (c): passively combined data-stream; (d) the output data-stream (with the FPLD modulated at below threshold condition).
- Fig. 4.3 The power dependent extinction ratio of the RZ-formatted data at rf-modulating power of (i) 24.4 dBm and (ii) 24.7 dBm. Inset: the conceptual diagrams of (i) the power-dependent and (ii) the power-independent OR gating operations.
- Fig. 4.4 P-I curves and of the rf-modulated and injection-locked FPLD for different injection power.
- Fig. 4.5 P-I slope of the rf-modulated and injection-locked FPLD for different injection power.
- Fig. 4.6 The power-dependent (dotted trace) and power-independent (solid trace) logic OR output.
- Fig. 5.1 Experimental setup for measurement of the dynamic chirp of the RZ-formatted data stream. DCM: dispersion compensation module.
- Fig. 5.2 Experimental setup for 20-GHz soliton amplification and transmission.  
[M. Nakazawa, K. Suzuki, and Y. Kimura, *Opt. Lett.* 14, 1065 (1989).]
- Fig. 5.3 Experimental setup for soliton transmission with a preemphasis technique using erbium-doped fiber amplifiers and repeaters.  
[M. Nakazawa, K. Suzuki, and Y. Kimura, "3.2-5 Gb/s, 100 km Error-Free Soliton Transmissions with Erbium Amplifiers and Repeaters," *IEEE Photon. Technol. Lett.* 2, 216 (1990).]
- Fig. 5.4 Temporal trace of our RZ-formatted data by injection-locking the synchronously-modulated FPLD just below threshold current.
- Fig. 5.5 Optical spectrum of the RZ-formatted data stream.
- Fig. 5.6 Proposed experimental setup for soliton transmission for NRZ-to-RZ data format converter.
- Fig. 5.7 Chirp characteristic in conventional gain-switching pulse.
- Fig. 5.8 Chirp characteristic of an injection-locking-induced pulse train.
- Fig. 5.9 Dynamic chirp of an injection-locking-induced data stream.
- Fig. 5.10 Curves of the dispersion versus the wavelength for standard single mode fiber, Corning MetroCor fiber, and dispersion compensation fiber.
- Fig. 5.11 Chirping results of RZ-formatted data stream after passing through different fibers.
- Fig. 5.12 Pulse widths of RZ-formatted data stream after passing through different fibers.

## List of Tables

- Table 2.1 Typical parameter values for a 1.55  $\mu\text{m}$  semiconductor laser in a injection-locking condition.
- Table 3.1 Comparison among versatile NRZ-to-RZ techniques.
- Table 5.1 Formulas of calculation for exciting  $N = 1.4$  soliton.



# Chapter 1

## Introduction

### 1.1 Introduction of Semiconductor Lasers

To date semiconductor lasers have been considered the best light sources for high-bit-rate optical communication lines and fast optical data-processing systems. Compared to solid-state, gas, and dye lasers, the diode laser offers a considerably smaller size, higher efficiency, lower cost, and the unique ability to be modulated up to gigahertz rates by simply changing the driving current through the device. One of the main advantages of lightwave systems over electronic ones is their high speed and transmission capacity. The fundamental reason for this is the much higher carrier frequency of light ( $10^{14}$  to  $10^{15}$  Hz) in a lightwave system. To realize the potentially very high capacity of lightwave system, the light source used should be able to generate short pulses at high repetition rates and capable of being modulated and encoded. These requirements are completely satisfied by using semiconductor laser diodes.

#### 1.1.1 Historical Review of Semiconductor Lasers [1]

The advent of the laser dates back to 1958, the year in which the seminal paper of Schawlow and Townes appeared [2]. It was followed by the successful operation of a solid-state ruby laser [3] in May 1960 and of a He-Ne gas laser [4] in December 1960. The feasibility of stimulated emission in semiconductor lasers was considered during this period [5-7], and in 1962 several groups [8-11] reported the lasing action in semiconductors. The device consisted of a forward-biased GaAs *p-n* junction [8-10]. Electron-hole recombination in the depletion region of the *p-n* junction provided the optical gain, and the polished facets



perpendicular to the junction plane provided the optical feedback (by forming a resonant cavity)—the two necessary ingredients for any laser. Soon  $p$ - $n$  junction of other direct-band-gap semiconductor materials such as InAs, InP, GaAsP, and InPAs were used to obtain semiconductor lasers at different wavelengths. Practical utility of these earlier devices was, however, limited since a large value of the threshold current density ( $J_{th} \geq 50 \text{ kA/cm}^2$ ) inhibited their continuous operation at room temperature.

As early as 1963 it was suggested [12, 13] that semiconductor lasers might be improved if a layer of one semiconductor material were sandwiched between two cladding layers of another semiconductor that has a relatively wider band gap. Such a device consisting of two dissimilar semiconductors is commonly referred to as a *heterostructure laser*, in contrast to the single-semiconductor devices, which are labeled as *homostructure lasers*. Both of these structures are shown schematically in Fig. 1.1, which also indicates their typical physical dimensions. Heterostructure lasers are further classified as *single-heterostructure* or *double-heterostructure* devices depending on whether the active region, where lasing occurs, is surrounded on one or both sides by a cladding layer of higher band gap. The use of a heterostructure, however, requires a careful matching of the lattice constants of the two semiconductors. It was only in 1969 that the successful room-temperature operation of a heterostructure laser was demonstrated [14-16] using the liquid-phase epitaxial technique [17] for the growth of GaAs and  $\text{Al}_x\text{Ga}_{1-x}\text{As}$  layers. However, these lasers operated in the pulsed mode. Further work led in 1970 to heterostructure lasers operating continuously at room temperature [18, 19]. Notation such as (Ga,Al)As or AlGaAs/GaAs is often used to emphasize the heterostructure nature of these GaAs lasers.

Already in 1969 double-heterostructure GaAs lasers with room-temperature value of  $J_{th} \cong 5 \text{ kA/cm}^2$  were reported [16]. This value was reduced [18] to about  $1.6 \text{ kA/cm}^2$  in 1970, and by 1975 AlGaAs lasers with  $J_{th} \cong 0.5 \text{ kA/cm}^2$  were demonstrated using thin

( $\sim 0.1 \mu\text{m}$  thick) active layers [20]. This was an improvement by more than two orders of magnitude over the simple homostructure lasers first made in 1962. It converted the semiconductor laser from a laboratory curiosity to a practical, compact, coherent light source useful for numerous applications.

The physical reason for the reduction in the threshold current density with the use of a heterostructure device is twofold [12, 13]. The cladding layers surrounding the active layer have a higher band gap and at the same time a lower refractive compared with those of the active layer (see Fig. 1.2). The band-gap difference helps to confine electrons and holes to the active layer, where they recombine to produce the optical gain. At the same time the refractive-index difference confines the optical mode close to the active layer, which acts as a dielectric waveguide. The optical-mode confinement significantly reduces the internal loss [14] that would otherwise occur in the absence of index guiding due to the spreading of the optical mode in the lossy regions.

A double-heterostructure semiconductor laser such as shown in Fig. 1.1 is sometimes called a *broad-area laser* since it does not incorporate any mechanism for the lateral (parallel to the junction plane) confinement of the injected current or the optical mode. As early as 1967, stripe-geometry homostructure lasers were proposed [21] to limit the lateral spread of the injected carriers inside the active layer, as shown in Fig. 1.3. In these lasers the current is injected over a narrow ( $\sim 10 \mu\text{m}$ ) central region using a stripe contact. The stripe geometry was adopted for heterostructure lasers [22] in 1971. Such lasers are also referred to as gain-guided (see Fig. 1.4a) since it is the lateral variation of the optical gain that confines the optical mode to the stripe vicinity [23]. By contrast, heterostructure lasers where the optical mode confinement occurs mainly through lateral variations of the refractive index are termed index-guided (see Fig. 1.4b). A large number of index-guided structures have been proposed and demonstrated over past decades. The literature is too vast to cite them individually, and a discussion of their relative merits can be found in several books [24-26] that also describe

the research and development effort for AlGaAs lasers up to 1980.

GaAs lasers are of continued interest. Using the growth techniques of vapor-phase epitaxy [27] and molecular-beam epitaxy [28], multi-quantum-well laser structures have been developed [29]. In these devices the active region is not a single GaAs layer but rather consists of several thin ( $\sim 0.01 \mu\text{m}$ ) layers composed alternatively of GaAs and AlGaAs materials. Recently the emphasis has shifted toward high-power GaAs lasers and phased-array semiconductor lasers [30, 31]. In one approach, multiple stripes are used to generate distinct regions of optical gain in the junction plane and the near field consists of several spots. However, since the stripes are not widely separated, the optical field in the gain region of each emitter overlaps with that of the neighboring emitter. Such a coupling leads to a phase-locked array of emitters providing well-collimated high power output. Whereas the output power from a conventional GaAs laser is usually below 50 mW, more than 2 W of power has been obtained [31] by this technique of phase-locked arrays.

So far we have followed the development of GaAs lasers operating usually in the wavelength range of 0.8—0.9  $\mu\text{m}$ . Long-wavelength semiconductor lasers in the range of 1.1—1.6  $\mu\text{m}$  are of considerable interest for optical fiber communications [32]. Although several material systems were considered, the combination InGaAsP-InP turned out to be most suitable in view of its nearly perfect lattice match [33]. The active layer is composed of the  $\text{In}_{1-x}\text{Ga}_x\text{As}_y\text{P}_{1-y}$  quaternary alloy. By varying the mole fractions  $x$  and  $y$ , almost any wavelength in the 1.1—1.6  $\mu\text{m}$  range can be selected. The cladding layers in this heterostructure layer (see Fig. 1.1b) consist of either InP or InGaAsP itself with different mole fractions  $x$  and  $y$ .

Room-temperature operation of a 1.1- $\mu\text{m}$  InGaAsP laser in the pulsed mode [34] was reported in 1975. The adoption of stripe geometry led to continuous operation [35] of such lasers in 1976. In 1977 the wavelength was extended [36] to 1.3  $\mu\text{m}$ . Since low-loss dispersion-free fibers at 1.3  $\mu\text{m}$  were already available [37], considerable attention was

focused to develop a practical InGaAsP laser at this wavelength. Motivated by the realization [38] of an ultra-low-loss ( $\sim 0.2$  dB/km) fiber at the  $1.55\text{-}\mu\text{m}$  wavelength, several groups [39-44] in 1979 reported on InGaAsP lasers operating in the vicinity of  $1.55\ \mu\text{m}$ . Since then the development effort for InGaAsP lasers operating in the wavelength range of  $1.3\text{--}1.6\ \mu\text{m}$  has proceeded at an enormous pace [45-47]. The primary motivation is due to their application in optical fiber communications, and the use of InGaAsP lasers in long-haul optical communication systems has already reached the commercial stage [48].

### 1.1.2 Operating Principles of Semiconductor Lasers

This subsection is to provide a qualitative understanding of the physics behind the semiconductor laser. To form a laser, a gain medium and a feedback mechanism are both necessary. A gain medium, which is a semiconductor material in a semiconductor laser, can amplify the electromagnetic radiation propagating inside it and provide the spontaneous-emission noise input. A feedback mechanism, which is obtained using the cleaved facets of the semiconductor material that form a Fabry-Perot (FP) cavity, can confine the electromagnetic field through the well-defined optical modes. The mode confinement is achieved through dielectric waveguiding. A semiconductor laser needs to be externally pumped to obtain the optical gain, and both electrical and optical pumping techniques have been used for this purpose. A simple, practical, and most commonly used method employs current injection through the use of a forward-biased  $p\text{-}n$  junction. Such semiconductor lasers are sometimes referred to as injection lasers or laser diodes.

#### ◆ **p-n Junction**

A  $p\text{-}n$  junction [49] is formed by bringing a  $p$ -type and an  $n$ -type semiconductor into contact with each other. When they first come in contact, their quasi-Fermi levels do not match

since the two are not in equilibrium. Equilibrium is, however, quickly established through diffusion of electrons from the  $n$  side to the  $p$  side, while the reverse occurs for holes. These diffusing electrons and holes recombine in the junction region. Eventually a steady state is reached in such a way that further diffusion of electrons and holes is opposed by the built-in electric field across the  $p$ - $n$  junction arising from the negatively charged acceptors on the  $p$  side and the positively charged donors on the  $n$  side. The Fermi level is then continuous across the  $p$ - $n$  junction, as shown in Fig. 1.5, where the energy-band diagram of the  $p$ - $n$  *homojunction* (junction between two similar semiconductors) is shown.

When a  $p$ - $n$  junction is forward-biased by applying an external voltage, the built-in electric field is reduced, making possible a further diffusion of electrons and holes across the junction. As Fig. 1.5b shows, in a narrow depletion region both electrons and holes are present simultaneously and can recombine either radiatively or nonradiatively. Photons of energy  $h\nu \cong E_g$  are emitted during radiative recombination. However, these photons can also be absorbed through a reverse process that generates electron-hole pairs. When the external voltage exceeds a critical value, a condition known as *population inversion* is achieved, in which the rate of photon emission exceeds that of absorption. The  $p$ - $n$  junction is then able to amplify the electromagnetic radiation, whose wavelength satisfies

$$\lambda \cong \frac{1.24}{E_g} \quad (1.1)$$

where  $E_g$  is the band gap of the semiconductor material in electron volts and the lasing wavelength  $\lambda$  is in micrometers. Therefore, the  $p$ - $n$  junction is said to exhibit *optical gain*. However, for a *homojunction* the thickness of the region where gain is sufficiently high is very small ( $\sim 0.01 \mu\text{m}$ ) since there is no mechanism to confine the charge carriers, as shown in Fig. 1.1a.

To solve the carrier-confinement problem, the use of a  $p$ - $n$  *heterojunction* is proposed [12, 13], as shown in Fig. 1.1b. Figure 1.6 shows the energy-band diagram for a

double-heterostructure laser wherein the thin  $p$ -type active region has a lower band gap compared to that of the two  $p$ -type and  $n$ -type cladding layers. Electrons and holes can move freely to the active region under forward bias. However, once there, they cannot cross over to the other side because of the potential barrier resulting from the band-gap difference. This allows for a substantial build-up of the electron and hole population inside the active region, where they can recombine to produce optical gain. The width of the gain region is determined by the active-layer thickness, typically  $0.1\text{-}0.3\ \mu\text{m}$ . As mentioned earlier, it was the adoption of the heterostructure scheme that resulted in significantly lower threshold current densities (compared with a homojunction) and led to the room-temperature operation of semiconductor lasers.

#### ◆ Dielectric Waveguide

The successful operation of a laser requires that the generated optical field should remain confined in the vicinity of the gain region. In double-heterostructure semiconductor lasers the optical confinement occurs by virtue of a fortunate coincidence. The active layer with a smaller band gap also has a higher refractive index compared with that of the surrounding cladding layers (see Fig. 1.2). Because of the index difference, the active layer in effect acts as a dielectric waveguide. The physical mechanism behind the confinement is total internal reflection, as illustrated in Fig. 1.7. When a ray traveling at an angle  $\theta$  (measured from the interface normal) hits the interface, it is reflected back if the angle  $\theta$  exceeds the critical angle  $\theta_c$  given by

$$\theta_c = \sin^{-1} \frac{\mu_1}{\mu_2} \quad (\text{critical angle}) \quad (1.2)$$

where  $\mu_1$  and  $\mu_2$  are the refractive indices of the cladding and active layers, respectively. Thus, rays traveling nearly parallel to the interface are trapped and constitute the waveguide mode.

## ◆ Recombination Mechanisms

When the current flowing through a semiconductor laser is increased, charge carriers (electrons and holes) are injected into the thin active region, where they recombine through radiative or nonradiative mechanisms. As one may expect, nonradiative recombinations are not helpful for laser operation, and attempts are made to minimize their occurrence by controlling point defects and dislocations. However, a nonradiative recombination mechanism, known as the *Auger process*, is intrinsic and becomes particularly important for long-wavelength semiconductor lasers operating at room temperature and above. Physically speaking, during the Auger process the energy released by the electron-hole recombination is taken by a third charge carrier and is eventually lost to lattice phonons.

During a radiative recombination, the energy  $E_g$  released by the electron-hole pair appears in the form of a photon whose frequency  $\nu$  or wavelength  $\lambda$  satisfies the energy conservation relation  $E_g = h\nu = hc/\lambda$ . This can happen through two optical processes known as spontaneous emission and stimulated emission. These are shown schematically in Fig. 1.8. In the case of *spontaneous* emission, photons are emitted in random directions with no phase relationship among them. Stimulated emission, by contrast, is initiated by an already existing photon. The remarkable feature is that the emitted photon matches the original photon not only in its wavelength but also in direction of propagation. It is this relationship between the incident and emitted photons that renders the light emitted by a laser coherent.

## ◆ Laser Threshold

Although stimulated emission can occur as soon as current is applied to the semiconductor laser, the laser does not emit coherent light until the current exceeds a critical value, known as the *threshold current* ( $I_{th}$ ). This is so because stimulated

emission has to compete against the absorption processes during which an electron-hole pair is generated at the expense of an absorbed photon. Since the electron population in the valence band generally far exceeds that of the conduction band, absorption dominates. At a certain value of the external current, a sufficient number of electrons are present in the conduction band to make the semiconductor optically transparent. With a further increase in current, the active region of the semiconductor laser exhibits optical gain and can amplify the electromagnetic radiation passing through it. Spontaneously emitted photons serve as the noise input for the amplification process.

However, as mentioned above, a laser is formed by two necessary elements. The other necessary ingredient is *optical feedback*. In semiconductor lasers it is provided by the cleaved facets that form a Fabry-Perot (FP) cavity. The role of the FP cavity is twofold. First, it provides a directional selectivity for the process of stimulated emission, since only photons traveling along its axis are reflected back and forth. Second, it provides a wavelength selectivity since the feedback is strongest for wavelengths corresponding to the longitudinal modes of the FP cavity.

Because of the optical feedback, the number of photons traveling perpendicular to the facets increases when the current is large enough to satisfy the condition of net stimulated emission. However, some photons are lost through the partially transmitting facets and some get scattered or absorbed inside the cavity. If the loss exceeds the gain, stimulated emission cannot sustain a steady supply of photons. This is precisely what happens below threshold, when the laser output consists of mainly spontaneously emitted photons. At threshold, gain equals loss and stimulated emission begins to dominate. Over a narrow current range in the vicinity of the threshold current, the output power jumps by several orders of magnitude and the spectral width of the emitted radiation narrows considerably because of the coherent nature of stimulated emission.

In the above-threshold regime, laser output increases almost linearly with the current.



Almost all electrons and holes injected into the active region now recombine through stimulated emission, and the internal quantum efficiency approaches 100%. The performance of a semiconductor laser is governed by a large number of emission characteristics related to the static, dynamic, and spectral behavior of the light output.

## 1.2 Enabling Technology for Data Format Conversion

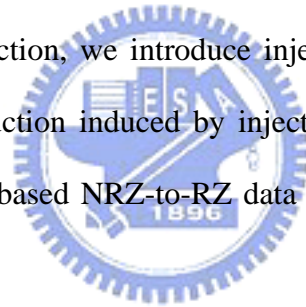
Ultrafast all-optical signal processing techniques are expected to play a major role in future communications systems in order to avoid any optoelectronic speed bottlenecks. In future all-optical networks (AONs), relatively low bit rates (e.g. 1-2.5 Gbit/s) will be used preferably with non-return-to-zero (NRZ) format which requires minimal electronic bandwidth and has greater timing tolerance, as compared to the return-to-zero (RZ) format. However, the RZ data format is quite useful in applications including passive time-division-multiplexing (TDM) for increasing the network throughput, soliton generation, and the suppression of stimulated Brillouin scattering [50, 51]. For these purposes, NRZ-to-RZ conversion is required. On the other hand, RZ-to-NRZ data format conversion is also necessary for reverse operation. There are versatile converters capable of transforming one format to the other [52-77]. In general, we divide these converters into two categories: RZ-to-NRZ and NRZ-to-RZ converters.

In RZ-to-NRZ converters, it has been realized using many methods, including a nonlinear optical loop mirror (NOLM) [52], a semiconductor optical amplifier based wavelength converter [53], a cross-phase modulation in an SOA-based Mach-Zehnder interferometric wavelength converter [54, 55], a dual-wavelength injection locking in a Fabry-Perot laser diode (FPLD) [56], the spectral filtering from a cross-phase modulated signal in a dispersion-shifted fiber [57], and the spectral line-by-line control [58].

In NRZ-to-RZ converters, it has been realized using many methods, including a

nonlinear active loop mirror (NALM) [59], a cross-gain compression-based wavelength converter [60], a nonlinear optical loop mirror (NOLM) [61, 62], a cross-phase modulation based single travelling wave semiconductor laser amplifier (TWSLA) [63], a gain-modulated semiconductor optical amplifier (SOA) [64], self-phase modulation (SPM) of SOA [65], a dual-wavelength injection locking in a FPLD [66], a cross-phase modulation in an SOA-based Mach-Zehnder interferometric wavelength converter [67], an optoelectronic oscillator (OEO) [68, 69], the transverse-magnetic mode absorption and SPM in a FPLD [70], an injection-locked FPLD at un-lasing condition [71-73], an SOA-loop-mirror [74], a Mach-Zehnder delay interferometer [75], and a dark-optical-comb injected SOA [76, 77].

In the following subsections, we will review two FPLD-based NRZ-to-RZ data format converters. In addition, techniques for generating short pulse (*i.e.* RZ format) in FPLDs are introduced. In the last subsection, we introduce injection locking in semiconductor lasers and the threshold current reduction induced by injection locking. These introductions are prepared for our novel FPLD-based NRZ-to-RZ data format converter, as shown in Section 1.3.



### **1.2.1 All-optical Non-Return-to-Zero (NRZ) to Return-to-Zero (RZ) Data Format Conversion Technology by Using FPLDs**

The Fabry-Perot laser diode (FPLD) based ultrafast all-optical signal processing techniques are expected to play important roles in future all-optical networks [66, 70, 78-81]. Versatile techniques such as the clock frequency division [79, 80], the wavelength conversion [81], and a nonreturn-to-zero (NRZ) to return-to-zero (RZ) format transformation [66, 70], have been demonstrated. Two featured works on the all-optical NRZ-to-RZ data format converters by using FPLDs are discussed. First, in 2002, Chow *et al.* [66] demonstrated an all-optical NRZ to RZ data format converter by using a cw-operated Fabry-Perot laser diode. They

used a dual-wavelength injection locking technique to achieve both wavelength and format conversion, as shown in Fig. 1.9. Later on, in 2004, Jeong *et al.* [70] used transverse-magnetic (TM) mode absorption of an FPLD and the self-phase modulation (SPM) technique to achieve NRZ-to-PRZ data format conversion for the aim to recover the data clock, as shown in Fig. 1.10.

### **1.2.2 Techniques for Generating Short Pulse**

The first short pulse generation in diode lasers was the observation of irregular pulse trains emitted by a single-contact laser in 1966 [82]. Later on, the generation of regular picosecond pulses was first demonstrated in a double-section device in 1967 [83]. Since then, progress has continued both in experimental techniques and in theoretical understanding. In particular, significant progress has been made since 1978 when the first successful demonstration of the active mode locking of a laser with an external cavity was realized. In general, there are two reasons why one wants to pulse a laser light. One is that, although there may be less power on average in the beam, the instantaneous power in one of the laser flashes may be thousands of times greater than the power in a continuous wave light. The other is that a pulsed laser light can give information on very rapidly-occurring processes, rather like a photo-finish in a race. It's a little like a very fast flash.

To obtain a pulsating light output, additional experimental manipulation must be performed with the laser. The simplest idea for generating laser pulses is to switch rapidly either gain or losses of the laser. Historically, the switching of diode-laser resonator quality or losses (Q-switching) was the first technique used to generate short light pulses [83]. Q-switching works in the following way. While the laser population inversion is building up, the switch is held in the “off” or high-loss state, ensuring a low Q. As the carrier density in the laser reaches its peak, the cavity is suddenly switched to the

high-Q condition, and the stored energy is rapidly emitted in an output optical pulse. The switching process can be initiated in one of two ways—active or passive. If the switching is caused by external influence, the technique is called as active Q-switching. However, there exists the possibility of passive/self-Q-switching of a laser by a bleachable (saturable) absorber. One feature of diode lasers is their ability to allow the ready incorporation of saturable absorbers of the same material as the active medium of the laser. As contrasted with other types of lasers, it is not necessary to have any external saturable absorber, but it is possible simply divide the diode into several sections and apply different currents to them. The parts of the laser with high current injection acts as the gain medium, while the unpumped sections or sections with a low pumping rate act as absorbers. Experimental Q-switched pulsewidths that have been obtained so far lie in the range of 2 to 30 ps at repetition rates above 10 GHz.

Another way for generating short pulses is gain switching [84-91]. Gain switching can be easily achieved in a diode laser by driving the laser with pulses or RF electrical currents. The first observations of relaxation oscillation when turning on a laser from below threshold have shown that short light pulses can be generated by direct modulation of the laser, with the optical pulsewidth considerably shorter than the applied electrical pulses. The fundamental reason for this is an extremely short photon lifetime in a diode-laser cavity due to very small cavity length and relatively high cavity losses. The basic idea of gain switching consisted of the excitation of the first spike of relaxation oscillation and termination of the driving current before the onset of the following spikes. This can be achieved by applying either short electrical pulses or strong sine wave modulation on the laser. A typical pulsewidth of gain-switched pulses lies in the range of 10 to 30 ps at repetition rates up to several GHz.

Although gain switching and Q-switching are simple and attractive techniques for generating short pulses, the shortest laser pulses can be generated using another technique

known as mode locking. The term “mode locking” originates from the fact that, when the optical field is written in terms of the modes of the laser cavity, under mode-locked conditions all modes in the laser spectrum are in phase. In the case of the active mode locking of a diode laser, the pumping current is modulated at a frequency that corresponds accurately to the spacing of the cavity modes. The first attempt to initiate active mode locking by current modulation was made in 1971 but met only limited success that resulted in the generation of pulses of a few hundred picoseconds in duration [92]. Similar to self-Q-switching, passive mode locking can be achieved through the action of a saturable absorber without any external intervention (the first demonstration in 1968 [93]). A significant step forward in generating extremely short pulses in the femtosecond range was made with the introduction of colliding-pulse mode locking, which, in fact, is a modification of passive mode locking [94]. It was colliding-pulse mode locking of a diode laser with an external cavity that resulted in the significant reduction of pulsewidths of generated pulses in 1981. Another important step was made in 1989 when the monolithic (without external cavity) mode locking of a laser diode was demonstrated for the first time [95]. Using monolithic mode-locking diode lasers, it is possible to generate short optical pulses with very high repetition rates in excess of 100 GHz. Optical pulses of few hundred femtoseconds at repetition rates of 350 GHz can be obtained by mode-locked diode lasers [96].

### **1.2.3 Introduction of Injection Locking [97]**

Injection locking of a semiconductor laser, with external coherent radiation injected into the laser cavity, appears to be drawing increasing attention [98-104]. Semiconductor diode lasers have a low Q factor cavity with the passband width as broad as several tens GHz and the gain spectrum several times broader, which is advantageous in achieving injection locking.

Recent progress in the diode laser fabrication technology has greatly improved the lasing characteristics, such as the mode stability and spectral purity, making injection locking a realistic subject for investigation. In one of the earlier reports it has been shown [99] that the waveform of the output response to a modulated exciting current can be greatly improved with light injection because the transient relaxation oscillation can be severely damped. Remarkable effects of the injection locking in controlling the spectrum and the frequency stability under direct modulation have recently been demonstrated [100, 101] and detailed experimental investigation on GaAs laser injection locking properties has been reported [102]. In 1994, Li [105] predicted that the gain is enhanced and hence threshold is decreased by including the spontaneous emission term. Later on, in 1998, Sivaprakasam and Singh [106] demonstrated the threshold current reduction experimentally by using two identical, single mode AlGaAs laser diodes (SDL 5412-H1,  $\lambda=850$  nm ).



### **1.3 Motivation of a novel FPLD-based NRZ-to-RZ Converter**

According to previous researches [60, 64], we know that the format conversion from NRZ to RZ can be obtained by manipulating the gain of device through an optical [60] (see Fig. 1.11) or an electrical [64] (see Fig. 1.12) method. Such a concept will be employed in an FPLD-based NRZ-to-RZ data format converter. First, it is well-known that the manipulation of the gain in FPLDs can be achieved by controlling the injection current. When the FPLD is gain-switched by using a sinusoidal wave or a short electrical pulse, it will generate an optical pulse, which is like the RZ signal. On the other hand, we experimentally observed that the threshold current of FPLDs can be reduced under external injection locking. Therefore, we combine these ideas and propose a new scheme to translate an NRZ-formatted optical data into an RZ-formatted optical data by biasing a synchronously-modulated FPLD at

un-lasing condition. In contrast to previous approaches, the FPLD used in our converter is operated just below threshold current by minimizing the DC driving current and appropriately setting the RF driving power. The FPLD becomes gain-switching when its threshold current is reduced by an external injection. That is, the FPLD receives the incoming NRZ data with high level (“1” bit), resulting in the generation of RZ data, whereas the low-level (“0” bit) data, ceasing the lasing of the FPLD. Such an external injection-locking not only achieves the NRZ-to-RZ conversion, but also helps to suppress the gain of side modes and the spontaneous emission, providing the FPLD output data stream a higher side mode suppression ratio (SMSR) and lower noise level.

## 1.4 Organization of Dissertation

The work described in this dissertation concentrates on the derivation of the reduction of the threshold current under external light injection locking condition and the application of this particular phenomenon in NRZ-to-RZ data format converter.

This dissertation is organized as follows: Chapter 2 derives the formula of the threshold current reduction. First, we will give a phenomenological approach, which is introduced by Coldren and Corzine, to diode lasers to derive the expression of the threshold current of diode lasers. Furthermore, by introducing the Li’s theory, we can derive the threshold current reduction under external light injection locking. Chapter 3 is the experimental setup and results of the FPLD-based NRZ-to-RZ converter. First, we use a continuous-wave (CW) light injection into the FPLD to observe the external light-injection-induced gain-switching. That is, the synchronously-modulated Fabry-Perot laser diode at below threshold condition becomes gain-switching when its threshold current is reduced by an external injection locking. Furthermore, we inject an incoming NRZ data stream into the FPLD, which receives the high level (“1” bit), resulting in the generation of a

RZ data, whereas receives the low-level (“0” bit), ceasing the lasing of the FPLD. Such an external injection-locking not only achieves the NRZ-to-RZ conversion, but also helps to suppress the gain of side modes and spontaneous emission, providing the FPLD output data-stream with a high side mode suppression ratio (SMSR) and low noise level. Chapter 4 is the experimental setup and results of an all-optical OR logic gate, which is realized by using such an FPLD-based NRZ-to-RZ converter. In such an OR gate, the issue of pulse inequality is solved by slightly enlarging the amplitude of the RF modulating power. In Chapter 5, we propose a transmission configuration by using a preemphasis technique (proposed by Nakazawa *et al.*) to transmit the converted RZ data stream. The corresponding parameters for realizing this configuration are calculated. In addition, for evaluation of chirp of such a data format converter, a dynamic relative chirp measurement is constructed for observation of the results of chirp compensation and the chirp after transmission. Finally, Chapter 6 summarizes the dissertation and gives some future directions.





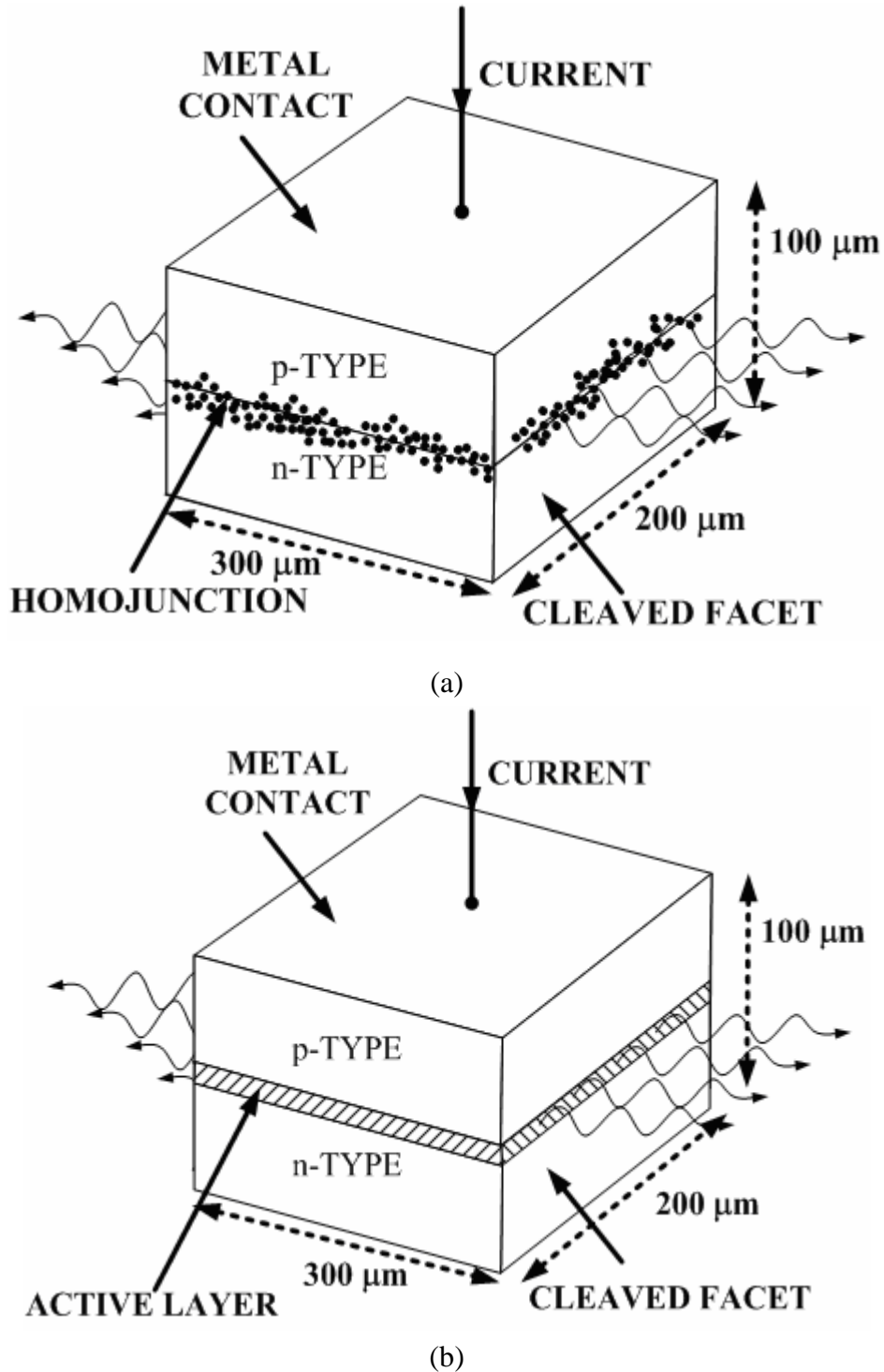


Fig. 1.1 Schematic illustration of (a) homostructure and (b) double-heterostructure semiconductor lasers with their typical physical dimensions. The dotted area represents the depletion region in the vicinity of the homojunction. The hatched area shows the thin ( $\sim 0.2 \mu\text{m}$ ) active layer of a semiconductor material whose band gap is slightly lower than that of the surrounding cladding layers.

[G. P. Agrawal, and N. K. Dutta, *Long-wavelength Semiconductor Lasers*, New York: Van Nostrand Reinhold, 1986.]

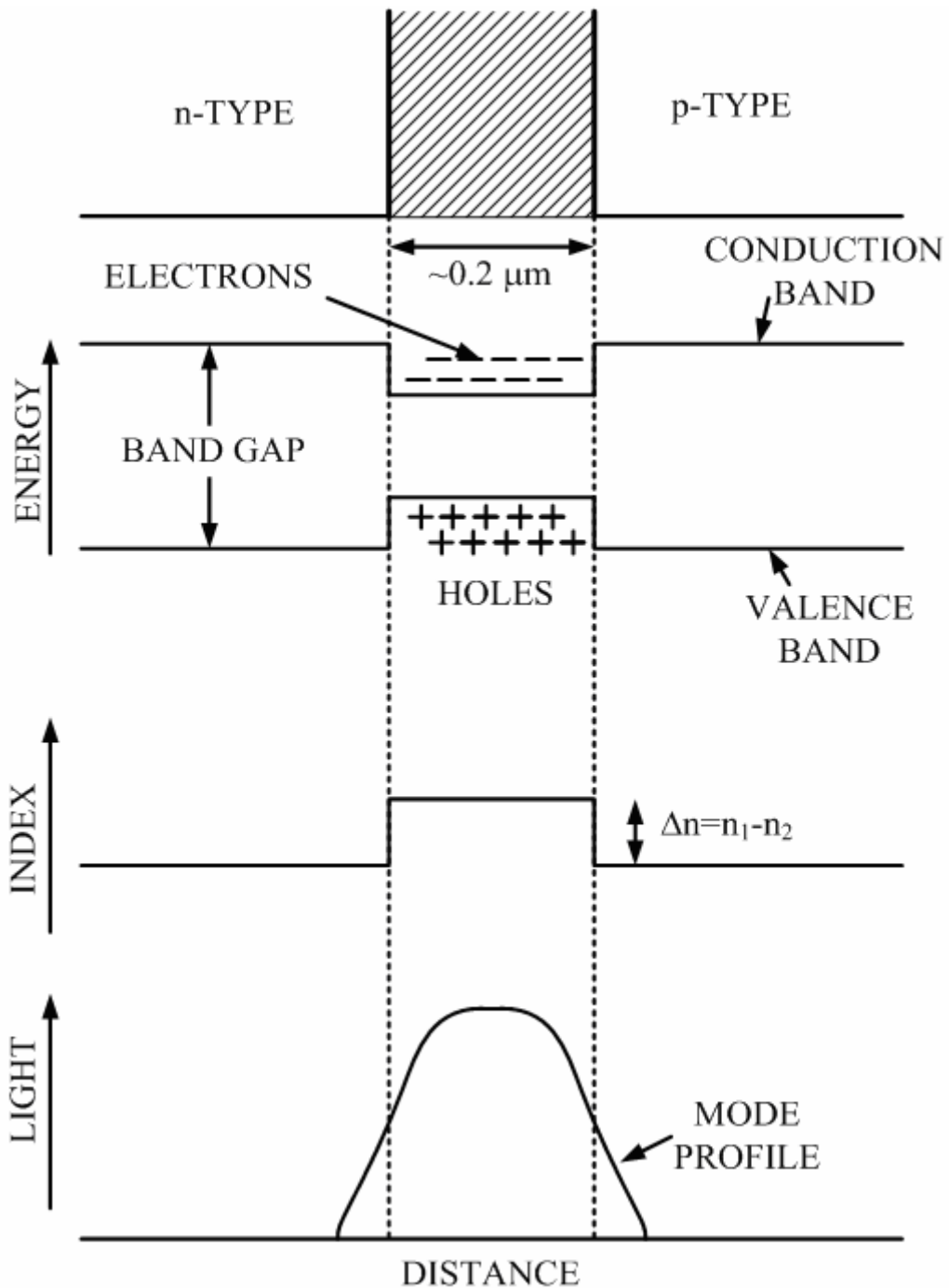


Fig. 1.2 Schematic illustration of the simultaneous confinement of the charge carriers and the optical mode to the active region occurring in a double-heterostructure semiconductor laser. The active layer has a lower band gap and a higher refractive index than those of the cladding layers.

[H. C. Casey, Jr., and M. B. Panish. *Heterostructure Lasers*, Parts A and B. New York: Academic Press, 1978.]

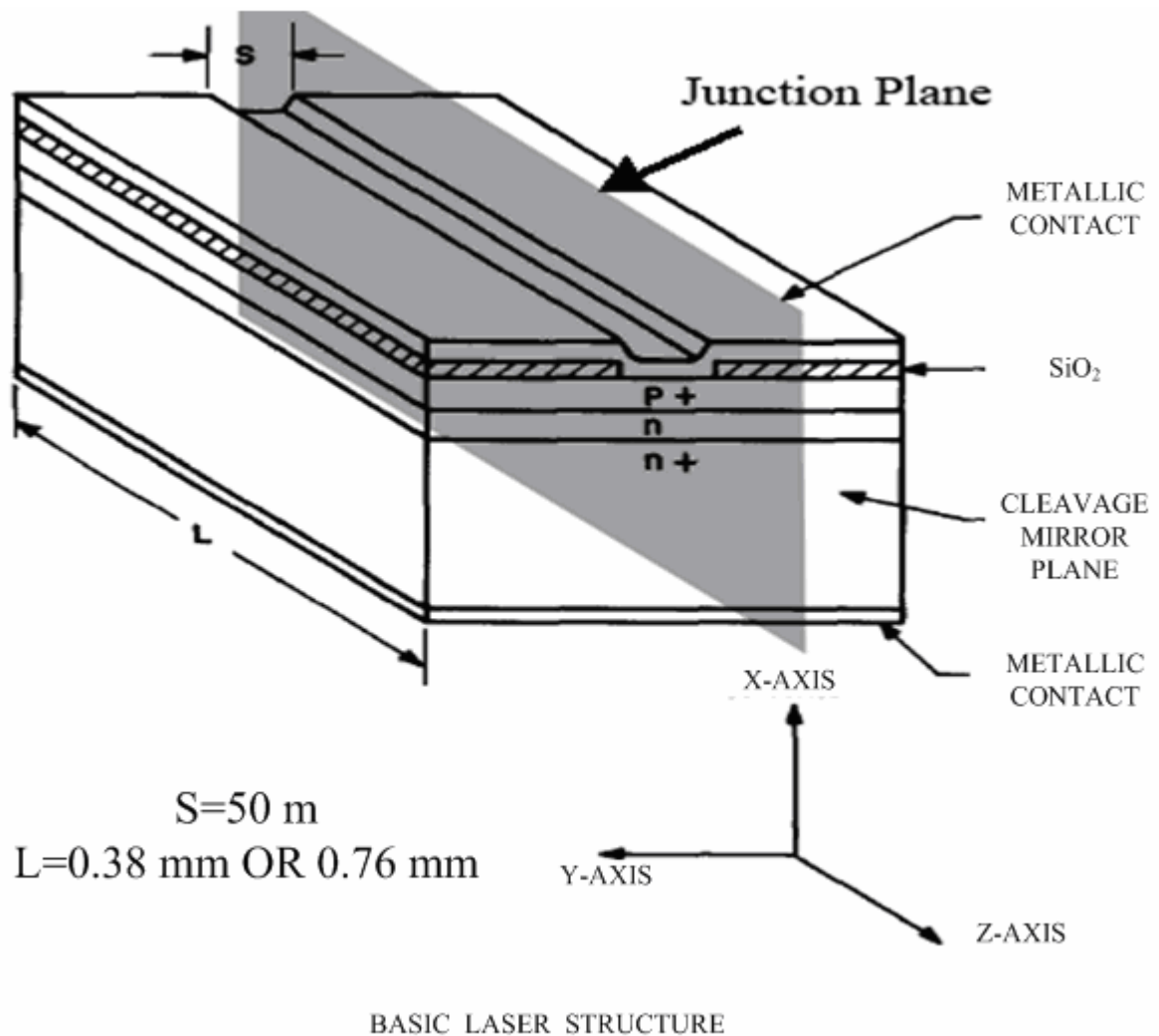


Fig. 1.3 Basic  $p^+nn^+$  laser structure showing the stripe geometry contact which confines the active portion of the junction to a narrow region. The xyz axes are also defined.  
 [J. C. Dymont, "Hermite-gaussian Mode Patterns in GaAs Junction Lasers," *Appl. Phys. Lett.* **10**, 84 (1967).]

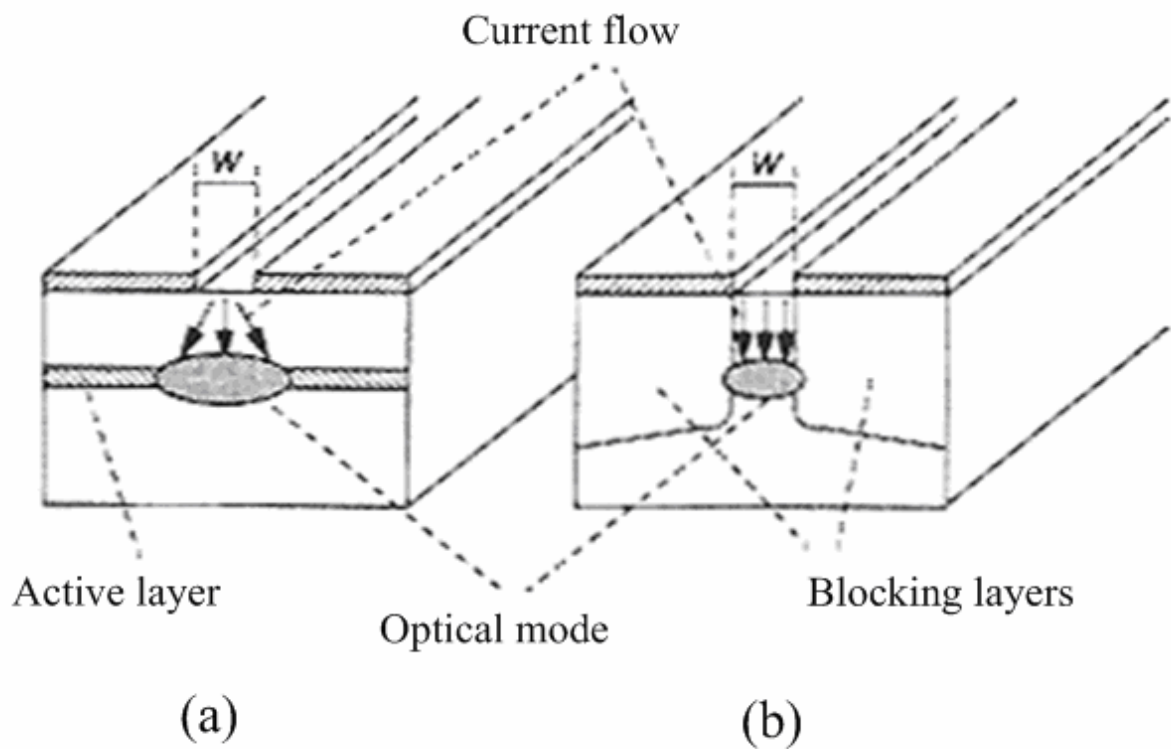


Fig. 1.4 Two types of diode lasers with strong transverse confinement: (a) a gain-guided laser with poor lateral confinement; (b) an index-guided laser for strong lateral confinement. The current flow is laterally restricted by a strip of width  $w$ .

[Peter Vasil'ev, *Ultrafast Diode Lasers: Fundamentals and Applications*, Boston: Artech House Publishers, 1995]

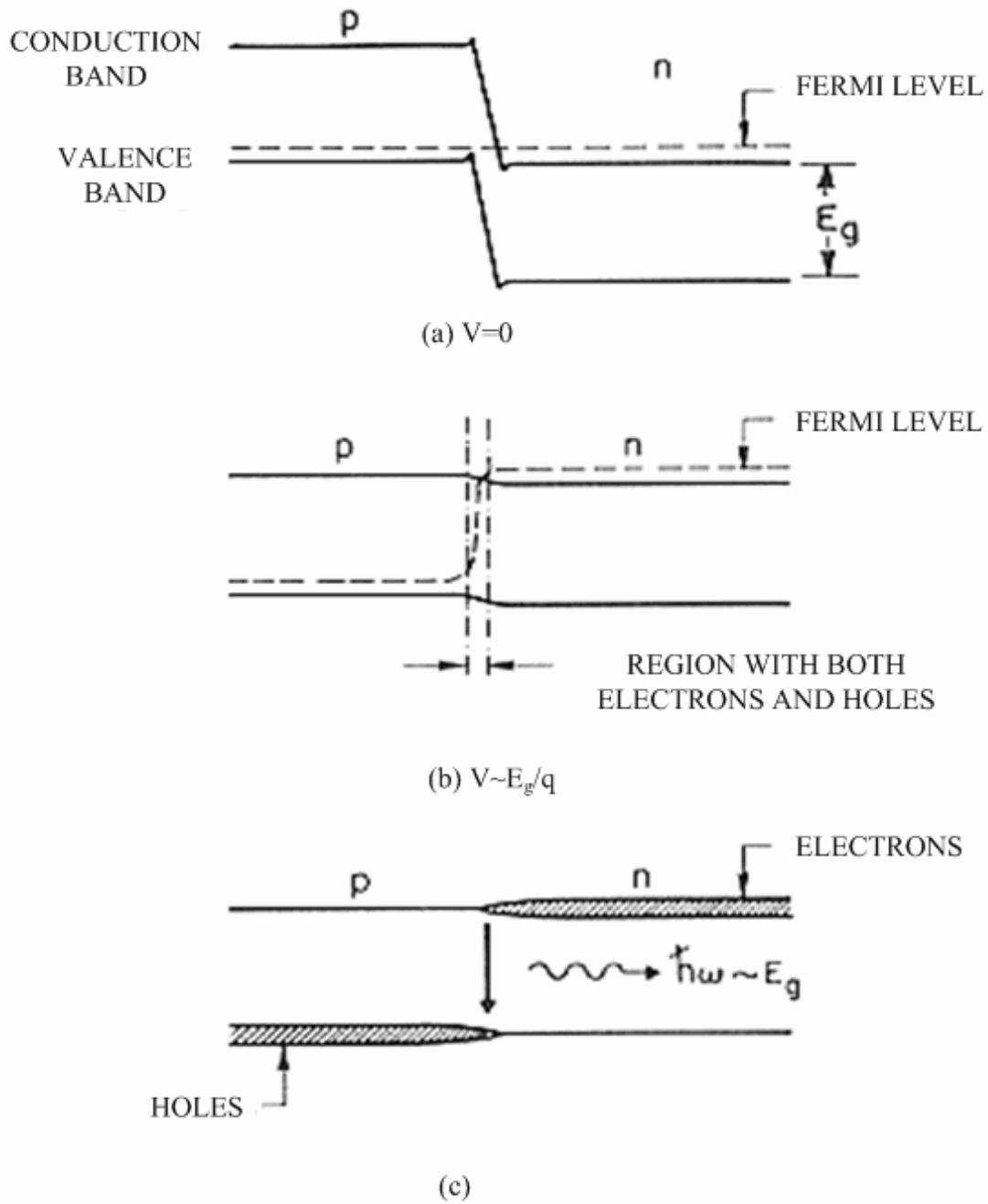


Fig. 1.5 Energy-band diagram of a  $p$ - $n$  junction at (a) zero bias and (b) forward bias. (c) Schematic representation of the electron and hole densities under forward bias. Radiative recombination of electrons and holes in the narrow overlapping region generates light. [G. P. Agrawal, and N. K. Dutta, *Long-wavelength Semiconductor Lasers*, New York: Van Nostrand Reinhold, 1986.]

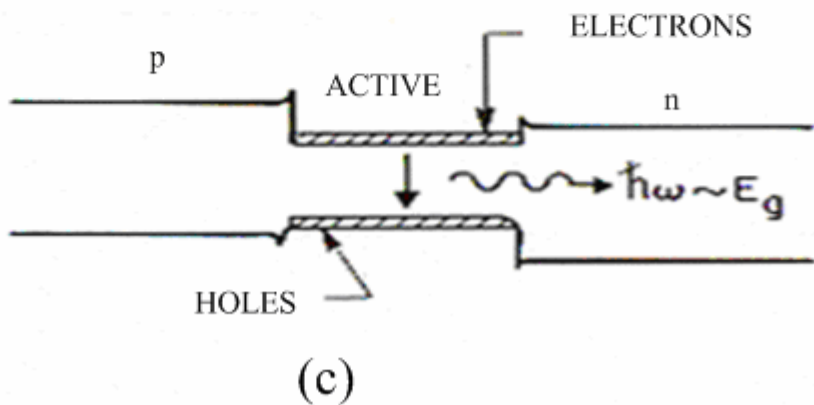
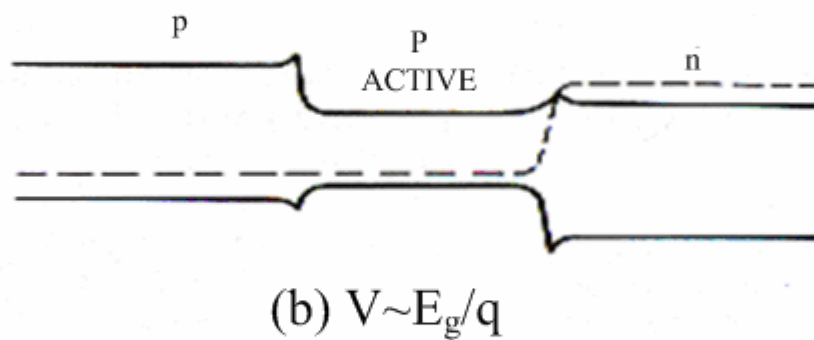
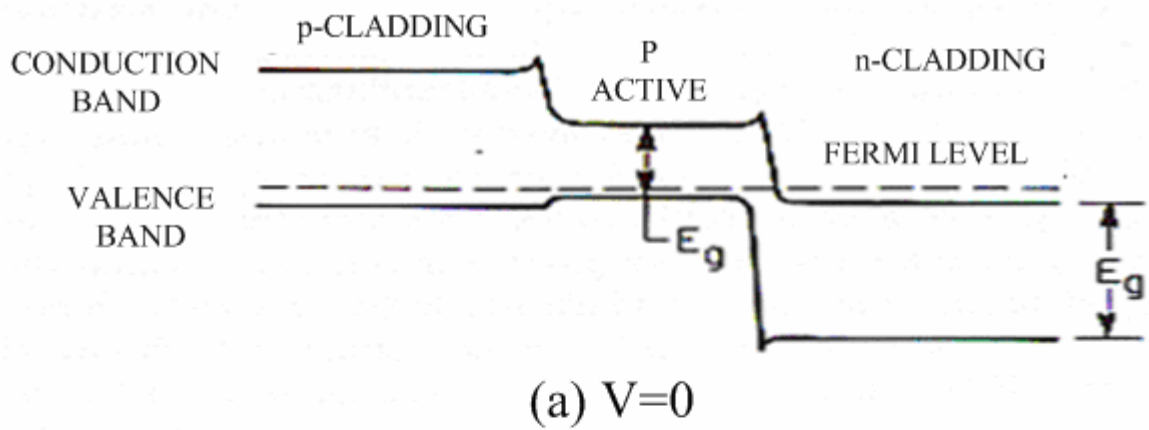


Fig. 1.6 Energy-band diagram of a double-heterostructure semiconductor laser at (a) zero bias and (b) forward bias. (c) The band-gap discontinuities at the two heterojunctions help to confine electrons and holes inside the active region, where they recombine to produce light. [G. P. Agrawal, and N. K. Dutta, *Long-wavelength Semiconductor Lasers*, New York: Van Nostrand Reinhold, 1986.]

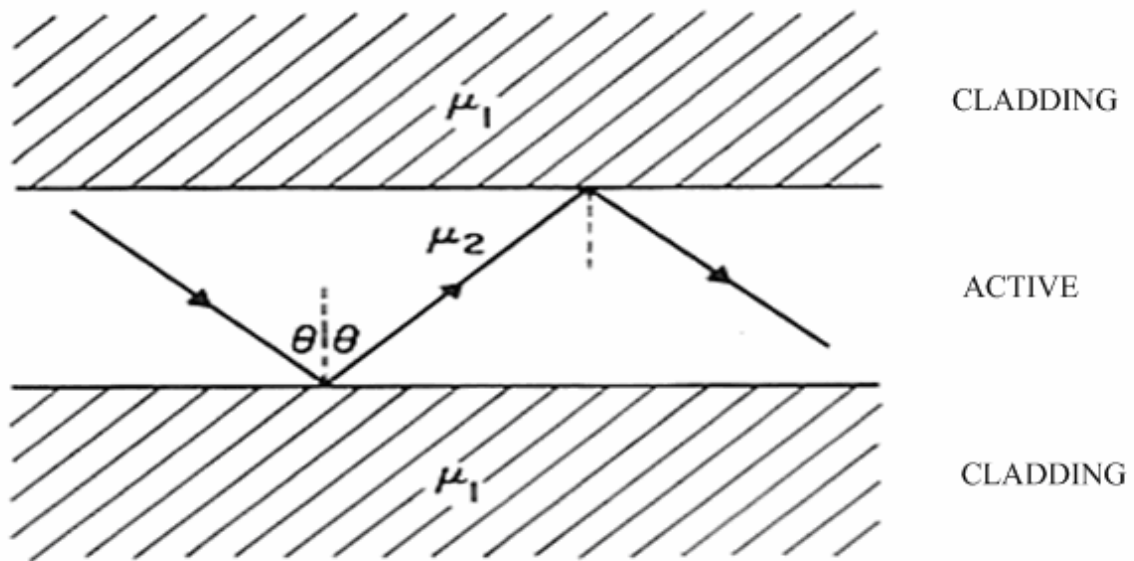


Fig. 1.7 Dielectric waveguiding in a heterostructure semiconductor laser. The relatively higher refractive index ( $\mu_2 > \mu_1$ ) of the active layer allows total internal reflection to occur at the two interfaces for angles such that  $\sin\theta > \mu_1/\mu_2$ .

[G. P. Agrawal, and N. K. Dutta, *Long-wavelength Semiconductor Lasers*, New York: Van Nostrand Reinhold, 1986.]

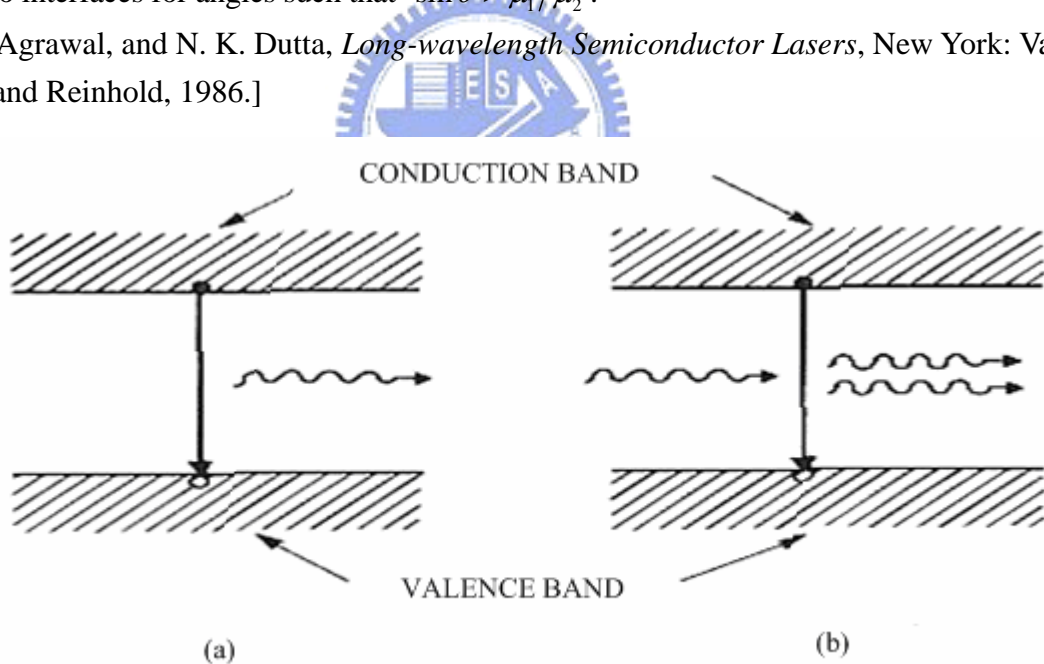


Fig. 1.8 Schematic illustration of (a) spontaneous-emission and (b) stimulated-emission processes wherein an electron-hole pair recombines to generate a photon. In the case of stimulated emission the two outgoing photons match in their frequency and direction of propagation.

[G. P. Agrawal, and N. K. Dutta, *Long-wavelength Semiconductor Lasers*, New York: Van Nostrand Reinhold, 1986.]

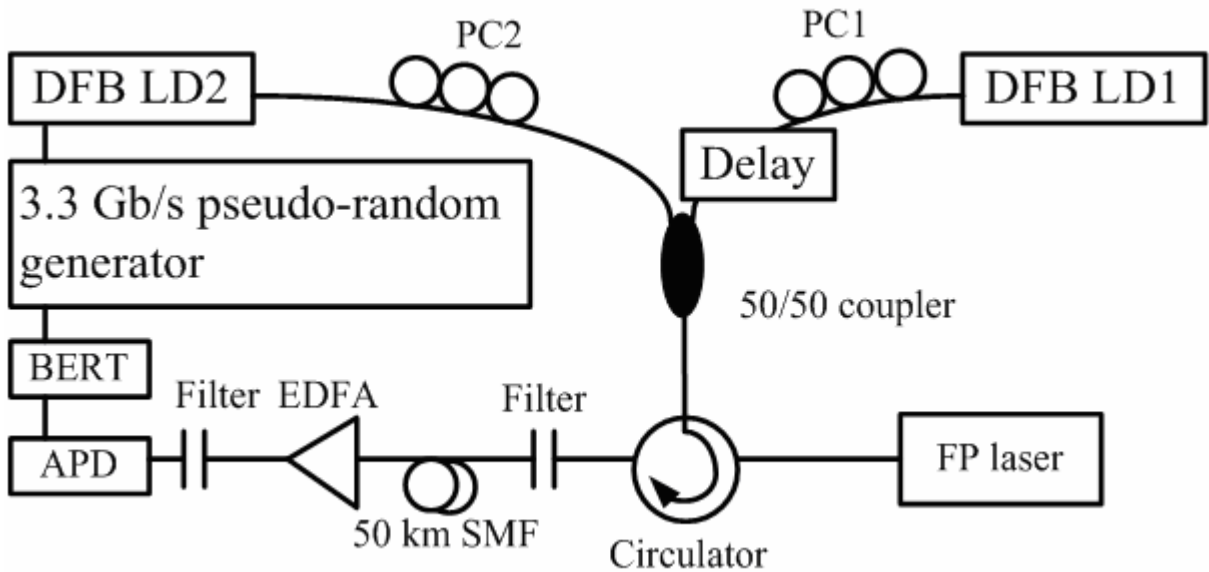


Fig. 1.9 Experimental setup. PC: polarization controller; SMF: single mode fiber; APD: avalanche photodiode; EDFA: erbium-doped fiber amplifier; BERT: bit-error tester.

[C. W. Chow, C. S. Wong, H. K. Tsang, "All-optical NRZ to RZ format and wavelength converter by dual-wavelength injection locking," *Opt. Commun.* **209**, 329 (2002).]

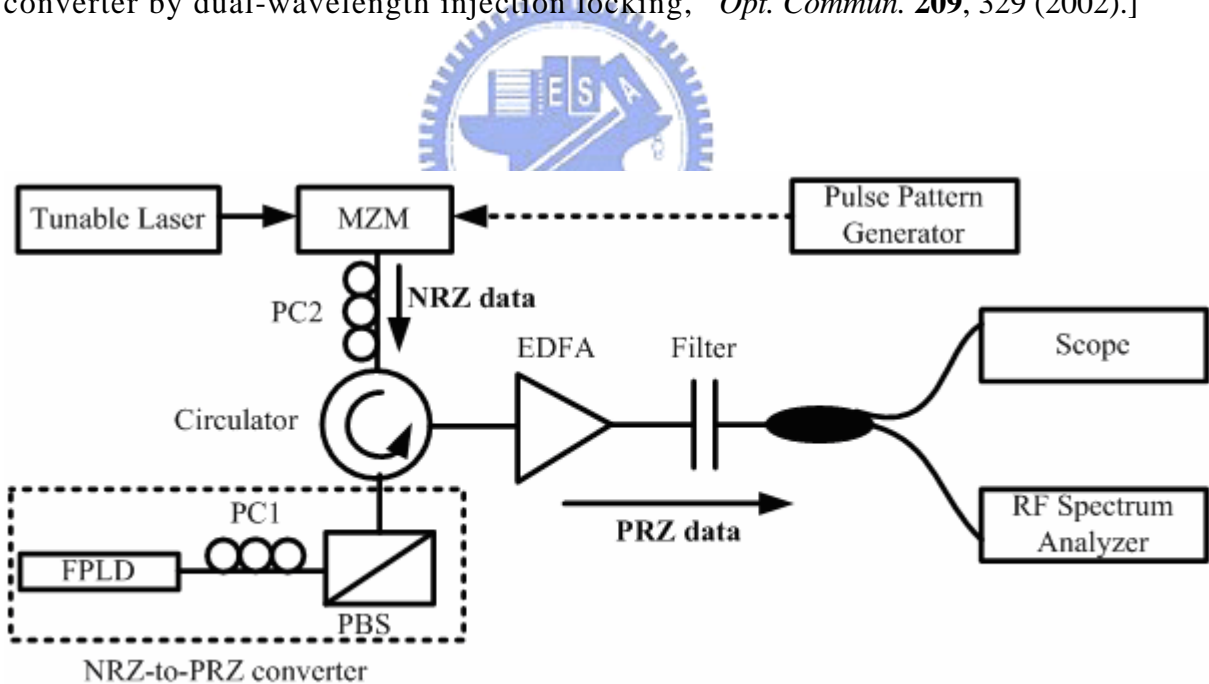


Fig. 1.10 Experimental setup for NRZ-to-PRZ converter; EDFA: erbium-doped fiber amplifier; PC: polarization controller; OBF: optical bandpass filter; PBS: polarization beam splitter.

[Y. D. Jeong, H. J. Lee, H. Yoo, and Y. H. Won, "All-optical NRZ-to-PRZ converter at 10 Gb/s based on self-phase modulation of Fabry-Perot laser diode," *IEEE Photon. Technol. Lett.* **16**, 1179 (2004).]



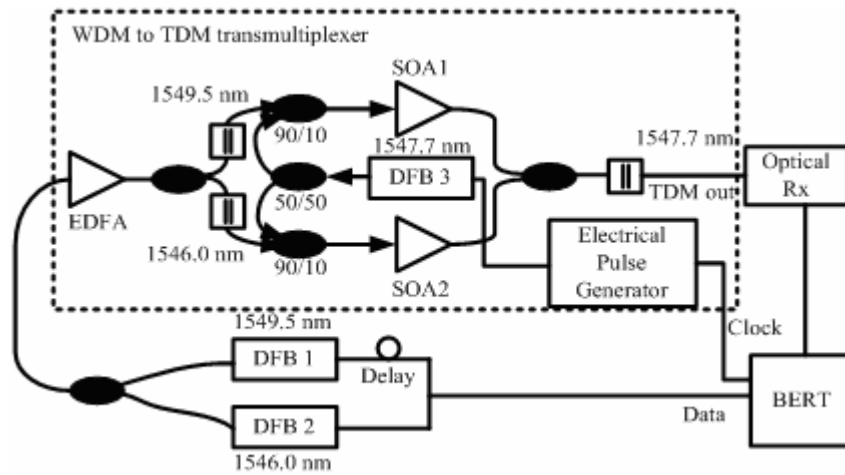


Fig. 1.11 Experimental setup. The gain-switched DFB3 is used to manipulate the gain in SOA1 and SOA2.

[J. P. R. Lacey, M. V. Chan, R. S. Tucker, A. J. Lowery and M. A. Summerfield, "All-optical WDM to TDM transmultiplexer," *Electron. Lett.* **30**, 1612 (1994).]

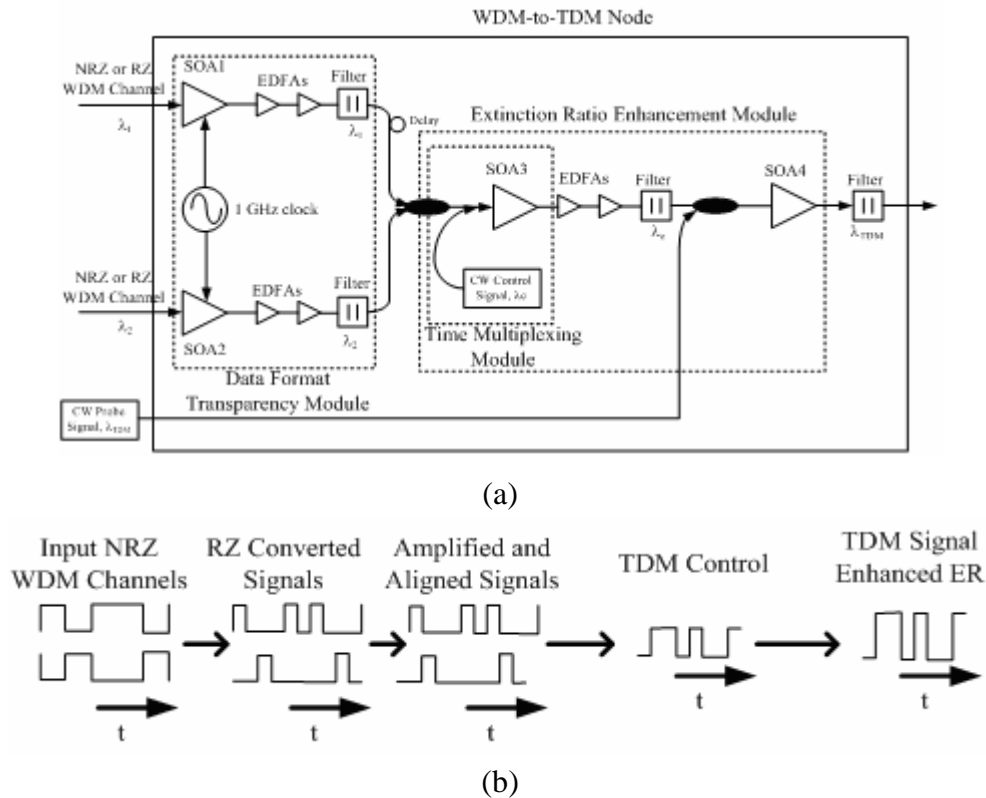


Fig. 1.12 (a) All-optical WDM-to-TDM node incorporating the modular functions of: (1) NRZ-to-RZ conversion; (2) extinction ratio enhancement; and (3) wavelength shifting. (b) Conceptual operation of the WDM-to-TDM node.

[D. Norte and A. E. Willner, "Demonstration of an all-optical data format transparent WDM-to-TDM network node with extinction ratio enhancement for reconfigurable WDM networks," *IEEE Photon. Technol. Lett.* **8**, 715 (1996).]

# Chapter 2

## Theory of Threshold Current Reduction under External Light Injection Locking

### 2.1 Introduction

In this chapter we attempt to develop the theory about the threshold current reduction in semiconductor lasers under external light injection based on phenomenological arguments. By operating a Fabry-Perot laser diode in the condition of the external light injection locking, we can observe the phenomenon of the threshold current reduction through the L-I (light-current) curve measurement. Such a threshold current reduction is mainly attributed to injection locking in semiconductor lasers, which is a promising method to synchronize one or more free-running lasers to a master laser [107, 108]. Injection locking can be applied to ensure single mode operation [109], to generate optical frequency and phase modulation [110, 111], and to reduce the spectral width [112]. In addition, it can also be exploited to study the static and dynamic properties of the semiconductor lasers [113, 114].

From a fundamental point of view, the change of the lasing threshold current due to injection locking [115] is very important. It provides a tool to monitor the spontaneous emission into the laser mode and interplay between the charge carrier generation and recombination as both of them depend on the frequency, phase and intensity of the injected signal and the operating point of the laser.

Sharfin and Dagenais [116] predicted that optical injection does not lower the lasing threshold, since the optical light injection can only decrease the gain from the zero field value. In their work they had calculated the threshold current using the rate equation

approach. But they neglected the spontaneous emission part. The threshold current was taken when the average gain in the cavity becomes equal to the average loss rate. However, in 1994, Li [117] predicted that the gain is enhanced and hence threshold is decreased by including the spontaneous emission term. The behavior is quite complicated, especially for single mode diode lasers, where the linewidth enhancement factor and the cavity resonance dependence on the injected signal are more prominent.

The reduction of the threshold current was demonstrated experimentally for the first time by Sivaprakasam and Singh [118]. They used two identical and single-moded AlGaAs laser diodes (SDL 5412-H1), whose emitting wavelength is around 850 nm. The one used for this study is termed the slave laser and the other providing the injected signal is termed the master laser. Both lasers are driven by ultra-low-noise current sources and temperature controlled by thermo-electric controllers to a precision of 0.01 K. As shown in Fig. 2.1, it is obvious that there is a reduction in the threshold current [118]. The threshold current taken is the point where there is sharp increase in the laser output. The injected power in this study is much less than the total increases hence there is a net increase in the gain. It is noted that the difference in power, which is proportional to the total gain change, was shown to have a maximum as the bias current approaches the threshold.

In Section 2.2, we introduce a phenomenological approach [119] to diode lasers. From a water reservoir model, we can derive a set of rate equations to describe the dynamics of carriers and photons. Furthermore, we adopt Li's theory and consider the influence of the external light injection locking on the threshold current reduction in Section 2.3. These derivations are shown that the external light injection locking can reduce the threshold current of a semiconductor lasers.

## 2.2 A Phenomenological Approach to Diode Lasers [119]

In this section, a phenomenological approach, which is introduced by Coldren and Corzine [119], is used to derive the expression of the threshold current in diode lasers. First, a rate equation model is carried out for the flow of charge into double-heterostructure (DH) active regions and its subsequent recombination. Some electron-hole pairs recombine and generate photons by spontaneous emission, as shown in Fig 2.2a. This incoherent light by spontaneous emission is important in light-emitting diodes (LEDs). In subsequent subsection, we will derive the relevant equations governing LED operation for integrity of the theory. Furthermore, we provide a systematic derivation of the dc light-current characteristics of diode lasers. We begin from the development of the rate equation for photon generation and loss in a laser cavity. It shows that only a small portion of the spontaneously generated light contributes to the lasing mode. Most of the lasing light comes from the stimulated recombination of carriers. Such a stimulated carrier recombination/photon generation process, as shown in Fig. 2.2c, is a *gain* process. Next, the threshold gain, which is used to compensate for cavity losses, is studied. The current required to reach this gain is called the threshold current, and it is shown to be the current necessary to supply carriers for the unproductive nonradiative and spontaneous recombination processes, which clamp at their threshold value as more current is applied. Above threshold, all additional injected carriers are recombined in the active region to contribute to photons in the lasing mode by a stimulated recombination process. A fraction escape through the mirrors; others are absorbed by optical losses in the cavity.

Finally, we introduce the modulation of lasers in Subsection 2.2.6. Under small-signal modulation, the rate equations for carriers and photons are found to be analogous to the differential equations that describe the current and voltage in an *RLC* circuit. Thus, the optical modulation response is found to have a resonance and to fall

off rapidly above this frequency. These derivations in Section 2.2 are prepared to obtain the injection-locking-induced reduction in the threshold current and the enhancement in the natural resonance frequency in FPLDs.

### 2.2.1 Carrier Generation and Recombination in Active Region

In a diode laser or LED, it is desirable to have all of the injected current contribute to electrons and holes which recombine in the active region. However, in practice only a fraction,  $\eta_i$  (*i.e.*, internal quantum efficiency), of the injected current,  $I$ , does contribute such carriers. Figure 2.3 illustrates the process of carrier injection into a double-heterostructure active region.

The active region, where carriers are recombined to provide useful gain and photon emission, is usually the lowest bandgap region within the depletion region of a *pin* diode for efficient injection. However, it is occasionally convenient to include some of the surrounding intermediate bandgap regions. In the active region, there may be photon emission and even gain at some undesired wavelength elsewhere in the device. It is important to realize that the active region includes all of the injected carriers, not just carriers that recombine radiatively at the desired transition energy. The active regions analyzed here are undoped or lightly doped, so that under high injection levels relevant to LEDs and lasers, the electron density equals the hole density, *i.e.*,  $n = p$  in the active region due to charge neutrality. Therefore, for the simplicity, we proceed with our analysis by specifically tracking only the electron density,  $n$ .

The carrier density in the active region is governed by a dynamic process. Here, we use a water reservoir, which is being simultaneously filled and drained, to simulate the process of establishing a certain steady-state carrier density in the active region of the diode lasers, as shown schematically in Fig. 2.4. As we proceed, the various filling

(generation) and drain (recombination) terms illustrated will be defined. The current leakage illustrated in Fig. 2.4 contributes to current reduction  $(1-\eta_i)I$  and is created by possible shunt paths around the active region. The carrier leakage,  $r_l$ , is due to carriers “splashing” out of the active region (by thermionic emission or by lateral diffusion if no lateral confinement exists) before recombining. Thus, this leakage contributes to a loss of carriers in the active region that could otherwise be used to generate light.

For the DH active region, a generation term is provided by the injected current into the active region,  $\eta_i I$ , and recombination terms are provided by various radiative and nonradiative recombination processes as well as carrier leakage. Therefore, we have the rate equation as

$$\frac{dn}{dt} = G_{gen} - R_{rec} \quad (2.1)$$

where  $G_{gen}$  is the rate of injected electrons and  $R_{rec}$  is the rate of recombining electrons per unit volume in the active region. Since there are  $\eta_i I/q$  electrons per second being injected into the active region, we can write the rate of injected electrons per unit volume as

$$G_{gen} = \frac{\eta_i I}{qV} \quad (2.2)$$

where  $V$  is the volume of the active region.

The recombination process is a bit more complicated, since several mechanisms must be considered, including:

1. a spontaneous recombination rate,  $r_{sp}$  (see Fig. 2.2a).
2. a nonradiative recombination rate,  $r_{nr}$  (see Fig. 2.2a).
3. a carrier leakage rate,  $r_l$  (see Fig. 2.4) due to the transverse and/or lateral potential barriers not sufficiently high.

4. a net stimulated recombination,  $r_{st}$ , including both stimulated absorption and emission (Figs. 2.2b and 2.2c).

Thus, the recombination process can be written as

$$R_{rec} = r_{sp} + r_{nr} + r_l + r_{st} \quad (2.3)$$

The first three terms  $r_{sp} + r_{nr} + r_l$  on the right-hand side of the equation refer to the natural or unstimulated carrier decay processes. The fourth one,  $r_{st}$ , requires the presence of photons. It is common to describe the natural decay processes by *carrier lifetime*,  $\tau$ . In the absence of photons or a generation term, the rate equation for carrier decay is just,  $dn/dt = -n/\tau$ , where  $n/\tau \equiv r_{sp} + r_{nr} + r_l$ . This natural decay can be expressed in a power series of the carrier density,  $n$ , since each of the terms depends upon the existence of carriers. Thus, Eq. (2.3) can be rewritten in several ways.

$$\begin{aligned} R_{rec} &= r_{sp} + r_{nr} + r_l + r_{st} \\ &= \frac{n}{\tau} + r_{st} \\ &= Bn^2 + (An + Cn^3) + r_{st} \end{aligned} \quad (2.3a)$$

It has been found that  $r_{sp} \sim Bn^2$  and  $r_{nr} + r_l \sim (An + Cn^3)$ . The coefficient  $B$  is called the *bimolecular recombination coefficient*, and it has a magnitude,  $B \sim 10^{-10} \text{ cm}^3/\text{s}$  for most AlGaAs and InGaAsP alloys. The carrier lifetime,  $\tau$ , is not independent of  $n$  in most circumstances. By using the second equivalent expression for  $r_{rec}$  in Eq. (2.3a), the carrier rate equation may be expressed as

$$\frac{dn}{dt} = \frac{\eta_i I}{qV} - \frac{n}{\tau} - r_{st} \quad (2.4)$$

In the absence of a large photon density, such as in a laser well below threshold or in most LEDs, it can be shown that  $r_{st}$  can be neglected. Equation (2.4) is expressed as

$$\frac{dn}{dt} = \frac{\eta_i I}{qV} - \frac{n}{\tau} \quad (\text{for LEDs or lasers well below threshold}) \quad (2.4a)$$

Figure 2.4 illustrates each of these terms in our reservoir analogy, explicitly showing “leaks,”  $r_{sp}$ ,  $r_{nr}$ , and  $r_l$  for  $n/\tau$ .

## 2.2.2 Spontaneous Photon Generation in LEDs

Before proceeding with the consideration of lasers, where  $r_{st}$  will become a dominant term above threshold, some understanding of the situation where the photon density is relatively low, such as in an LED where no feedback is present to provide for the build-up of a large photon density, is studied first. This case is actually similar to a laser below threshold, in which the gain is insufficient to compensate for cavity losses, and generated photons do not receive net amplification.

The spontaneous photon generation rate per unit volume is exactly equal to the spontaneous electron recombination rate,  $r_{sp}$ , since by definition every time an electron-hole pair recombines radiatively, a photon is generated. (Again,  $n$  equals the density of electron-hole pairs as well as electrons for relatively light doping). Under *steady-state* conditions ( $dn/dt = 0$ ), the generation rate equals the recombination rate, *i.e.*, from Eqs. (2.2) and (2.3), with  $r_{st} \approx 0$ ,

$$\frac{\eta_i I}{qV} = r_{sp} + r_{nr} + r_l \quad (2.5)$$

The spontaneously generated optical power,  $P_{sp}$ , is obtained by multiplying the number of photons generated per unit time per unit volume,  $r_{sp}$ , by the energy per photon,  $h\nu$ , and the volume of the active region,  $V$ . We could solve Eq. (2.5) for  $r_{sp}$ , but



since the exact dependence of  $r_{nr} + r_i$  on current  $I$  is unknown, this leads only to a parametric equation. Therefore, a *radiative efficiency*,  $\eta_r$ , is introduced as

$$\eta_r = \frac{r_{sp}}{r_{sp} + r_{nr} + r_i} \quad (2.6)$$

We must not forget that  $\eta_r$  usually depends upon carrier density somewhat. Then, from Eqs. (2.5) and (2.6), we have

$$P_{sp} = h\nu V r_{sp} = \eta_r \left( \eta_i \frac{h\nu}{q} I \right) \quad (2.7)$$

The product of  $\eta_i \eta_r$  is sometimes referred to as the LED internal efficiency. However, we shall not use this definition here, since it can lead to serious confusion when we move on to lasers. As we shall see, only  $\eta_i$  appears in the laser output power, and we have called it alone the internal efficiency. If we are interested in how much power the LED emits into some receiving aperture,  $P_{LED}$ , we must further multiply  $P_{sp}$  by the *net collection efficiency*,  $\eta_c$ , experienced in transmitting photons out of the semiconductor and into this aperture. This is typically relatively low (< 10%) for most LEDs, because the light is emitted in all directions, and much of it is totally reflected at the semiconductor-air interface. This situation is illustrated in Fig. 2.6.

As indicated by Fig. 2.6, much of the light is reflected back toward the active region rather than being coupled out of the semiconductor chip. A possible consequence is the regeneration of new carriers by the reabsorption of this light. In properly designed LEDs this “photon recycling” can greatly increase their efficiency, yielding an effective  $\eta_c > 10\%$ . The product of the three efficiencies (fraction of carriers injected into the active region, fraction of these recombining radiatively, and the fraction of those usefully coupled out)

gives the *external LED quantum efficiency*,  $\eta_{ex}$ . That is,

$$P_{LED} = \eta_c \eta_r \eta_i \frac{h\nu}{q} I = \eta_{ex} \frac{h\nu}{q} I \quad (2.8)$$

Thus, ignoring the slight dependence of  $\eta_{ex}$  on  $I$ , we see that the power coupled from an LED is directly proportional to the drive current. The external LED quantum efficiency,  $\eta_{ex}$ , is the number of photons coupled to the receiving aperture per electron flowing into the LED.

The frequency response of the LED can also be derived from the carrier rate equation (2.4a). We shall use the theorem that the Fourier transform of the impulse response in the time domain gives the frequency response. An impulse of current is simply a quantity of charge, which will establish an initial condition of  $n(t=0^+) = n_i$ . For  $t > 0$ , the rate equation can be written as

$$\frac{dn}{dt} = -\frac{n}{\tau} = -An - Bn^2 - Cn^3 \quad (2.9)$$

With the polynomial expansion of the recombination rate, we are reminded that the carrier lifetime,  $\tau$ , is generally a function of the carrier density. If it were independent of  $n$ , the solution would be a simple exponential decay, and the frequency response would be analogous to that of a simple RC circuit in which the 3 dB cutoff frequency,  $\omega_c = 1/\tau$ .

In order for  $\tau$  to be constant:

1. the cubic term must be negligible.
2. either the linear term,  $An$ , must dominate (not good, since this represents nonradiative recombination) or the active region must be heavily doped, such that the  $Bn^2$  term which really equals  $Bnp$ , can be written as  $(Bp_d)n$ .

That is, the p-type doping level,  $p_d$ , must be greater than the injection level,  $n$ , so

that  $p_d + p \approx p_d$ . Under these conditions, then, the time response is just a simple exponential decay,

$$n(t) = n_i e^{-t/\tau} \quad (2.10)$$

and the frequency response is a Lorentzian function,

$$n(\omega) = \frac{n(0)}{1 + j\omega\tau} \quad (2.11)$$

which drops to  $0.707n(0)$  at  $\omega\tau = 1$ . For  $r_{sp} \approx (Bp_d)n$ , the output power,  $P_{LED}$ , which is proportional to  $r_{sp}$ , will also have the same frequency response. It should be clear that the cutoff frequency will be reduced if the carrier lifetime is increased.

### 2.2.3 Photon Generation and Loss in Laser Cavities

In analogy with the carrier rate equation, we construct another rate equation for the *photon density*,  $S$ , which includes the photon generation and loss terms. The main photon generation term above threshold, which is the regime of interest in lasers, is  $\mathcal{R}_{st}$ . Every time an electron-hole pair is stimulated by a photon to recombine, another photon is generated. However, as indicated in Fig. 2.5, since the cavity volume occupied by photons,  $V_p$ , is usually larger than the active region volume occupied by electrons,  $V$ , only a portion of photons can be used to stimulate the electron-hole pair to recombine and generate another photon within the active region. In another word, the photon density generation rate,  $\mathcal{R}_{st}$ , must be modified by adding an electron-photon overlap factor, which is generally referred to as the *confinement factor*,  $\Gamma = V/V_p$ , before  $\mathcal{R}_{st}$ . Therefore, in the photon rate equation the photon density generation rate is  $\left[ V/V_p \right] \mathcal{R}_{st} = \Gamma \mathcal{R}_{st}$ . Sometimes it is convenient to introduce an effective

thickness, width, and length that contains the photons,  $d_{eff}$ ,  $w_{eff}$ , and  $L$ , respectively. That is,  $V_p = d_{eff} w_{eff} L$ . Then, if the active region has dimensions,  $d$ ,  $W$ , and  $L_a$ , the confinement factor can be expressed as,  $\Gamma = \Gamma_x \Gamma_y \Gamma_z$ , where  $\Gamma_x = d/d_{eff}$ ,  $\Gamma_y = w/w_{eff}$  and  $\Gamma_z = L_a/L$ .

Photon loss is usually divided into two parts: (1) within the laser cavity it is due to optical absorption and scattering out of the mode; (2) it also occurs at the output coupling mirror where a portion of the resonant mode is usually coupled to some output medium. Here we first deal with the net photon loss by a photon lifetime,  $\tau_p$ , which is like the carrier lifetime,  $\tau$ , in the carrier rate equation. A photon rate equation can be written as

$$\frac{ds}{dt} = \Gamma r_{st} + \Gamma \beta_{sp} r_{sp} - \frac{s}{\tau_p} \quad (2.12)$$

where  $\beta_{sp}$  is the *spontaneous emission factor*, which is just the reciprocal of the number of optical modes in the bandwidth of the spontaneous emission. As also indicated by Eq. (2.12), in the absence of generation terms,  $\Gamma r_{st} + \Gamma \beta_{sp} r_{sp}$ , the photons decay exponentially with a decay constant of  $\tau_p$ .

Equations (2.4) and (2.12) are two coupled equations that can be solved for the steady-state and dynamic responses of a diode laser. However, in their present form there are still several terms that need to be written explicitly in terms of  $n$  and  $s$  before such solutions are possible. First, we shall deal with the photon density generation rate,  $r_{st}$ . As mentioned above, a net stimulated recombination,  $r_{st}$ , including both stimulated absorption and emission (Figs. 2.2b and 2.2c), is important. The positive photon density generation rate represents the photon-stimulated net electron-hole recombination which generates more

photons. This is a *gain* process for photons. As illustrated in Fig. 2.2, the net effect of the upward and downward electronic transitions, corresponding to stimulated absorption and emission of photons, respectively, are included. In Fig. 2.7 we show the growth of photon density from an incoming value of  $s$  to an exiting value of  $s + \Delta s$  as it passes through a small length,  $\Delta z$ , of the active region. As shown in Fig. 2.7, we can define this growth in terms of a *gain per unit length*,  $g$ , by

$$s + \Delta s = s e^{g \Delta z} \quad (2.13)$$

If  $\Delta z$  is sufficiently small,  $\exp(g \Delta z) \approx (1 + g \Delta z)$ . Also, using the fact that  $\Delta z = v_g \Delta t$ , where  $v_g$  is the group velocity, we find that,  $\Delta s = s g \Delta z = s g v_g \Delta t$ . Therefore, the photon density generation rate can be expressed as

$$r_{st} = \frac{\Delta s}{\Delta t} = v_g g s \quad (2.14)$$

Thus, we can now rewrite the carrier and photon density rate equations,

$$\frac{dn}{dt} = \frac{\eta_i I}{qV} - \frac{n}{\tau} - v_g g s \quad (2.15)$$

$$\frac{ds}{dt} = \Gamma v_g g s + \Gamma \beta_{sp} r_{sp} - \frac{s}{\tau_p} \quad (2.16)$$

Of course, we still have not made all the substitutions necessary to directly solve the two equations simultaneously. In general, the gain as a function of carrier density can be approximated by a straight line (see Fig. 2.8), at least under small-signal conditions. The gain can be expressed as

$$g \approx a(n - n_{tr}) \quad (2.17)$$

where the slope  $a$  is the *differential gain* (or gain coefficient),  $\partial g / \partial n$ , and  $n_{tr}$  is the injected carrier density required to achieve transparency (*i.e.*,  $r_{12} = r_{21}$ ), which is called the

*transparency carrier density*. Of course, we also know that  $n/\tau$  can be replaced by the polynomial  $An + Bn^2 + Cn^3$ , where the terms estimate defect, spontaneous ( $r_{sp}$ ), and Auger recombination, respectively.

## 2.2.4 Threshold or Steady-State Gain in Lasers

Now, we will explicitly express the photon lifetime,  $\tau_p$ , in terms of the losses associated with optical propagation along the cavity and the cavity mirrors. Also, we show that the net loss of some mode gives the value of net gain required to reach the lasing threshold.

The optical energy of a modern diode laser propagates in a dielectric waveguide mode which is confined both transversely and laterally as defined by a normalized transverse electric field profile,  $U(x, y)$ . In the axial direction this mode propagates as  $\exp(-j\tilde{\beta}z)$ , where  $\tilde{\beta}$  is the complex propagation constant which includes any loss or gain. Thus, the time- and space-varying electric field can be written as

$$\mathcal{E} = \hat{\mathbf{e}}_y E_0 U(x, y) e^{j(\omega t - \tilde{\beta}z)} \quad (2.18)$$

where  $\hat{\mathbf{e}}_y$  is the unit vector indicating TE polarization and  $E_0$  is the magnitude of the field.

The complex propagation constant,  $\tilde{\beta}$ , includes the incremental *transverse modal gain*,  $\langle g \rangle_{xy}$ , and *internal modal loss*,  $\langle \alpha_i \rangle_{xy}$ . That is,

$$\tilde{\beta} = \beta + j\beta_i = \beta + \frac{j}{2} \left( \langle g \rangle_{xy} - \langle \alpha_i \rangle_{xy} \right) \quad (2.19)$$

where the real part of  $\tilde{\beta}$ ;  $\beta = 2\pi\bar{n}/\lambda$ , and  $\bar{n}$  is an effective index of refraction for the mode.

The transverse modal gain,  $\langle g \rangle_{xy}$ , and loss,  $\langle \alpha_i \rangle_{xy}$ , are found from weighted averages of the gain and loss, respectively, across the mode shape,  $U(x, y)$ . The factor of  $\frac{1}{2}$  in this equation

is due to that the gain,  $\langle g \rangle_{xy}$ , and loss,  $\langle \alpha_i \rangle_{xy}$  both are related to power. In general, we can let  $\langle g \rangle_{xy} = \Gamma_{xy} g$ , where  $\Gamma_{xy}$  is the transverse confinement factor, if  $g(x, y)$  is constant across the active region and zero elsewhere. Also, for notational convenience, we shall let  $\langle \alpha_i \rangle_{xy} = \alpha_i$ .

As illustrated in Fig. 2.9, most laser cavities can be divided into two general sections: an active section of length  $L_a$  and a passive section of length  $L_p$ . Also,  $g$  and  $\alpha_i$  will clearly be different in these two sections. In the passive section, by definition  $g = 0$ , and  $\alpha_i$  can be given a second subscript to designate its location. The propagation mode is reflected by end mirrors, which have amplitude reflection coefficients of  $r_1$  and  $r_2$ , respectively, to provide a resonant cavity. The amount transmitted is potentially useful output.

When the gain of a mode in the active section is increased to the point where all the propagation and mirror losses are compensated, the mode of the laser is to reach threshold, *i.e.*, the electric field exactly replicates itself after one round-trip in the cavity,  $\mathcal{E}(z = 2L) = \mathcal{E}(z = 0)$ . We have

$$r_1 r_2 e^{-2j\tilde{\beta}_{ath}L_a} e^{-2j\tilde{\beta}_{pth}L_p} = 1 \quad (2.20)$$

The subscript *th* denotes that this characteristic equation only defines the threshold value of  $\tilde{\beta}$ . Using Eq. (2.19), we can rewrite Eq. (2.20) into two equations for its magnitude and phase. For the magnitude,

$$r_1 r_2 e^{(\Gamma_{xy} g_{th} - \alpha_{ia})L_a} e^{-\alpha_{ip}L_p} = 1 \quad (2.21)$$

where we have chosen reference planes to make the mirror reflectivities real. Solving for  $\Gamma_{xy} g_{th} L_a$  we obtain

$$\begin{aligned}\Gamma_{xy} g_{th} L_a &= \alpha_{ia} L_a + \alpha_{ip} L_p + \ln\left(\frac{1}{r_1 r_2}\right) \\ &= \alpha_{ia} L_a + \alpha_{ip} L_p + \ln\left(\frac{1}{R}\right)\end{aligned}\quad (2.22)$$

where  $R$  is the mean mirror intensity reflection coefficient. For cleaved facet lasers based upon GaAs or InP,  $R \sim 0.32$ . Dividing Eq. (2.22) by the total cavity length,  $L$ , realizing that  $\Gamma_{xy} L_a / L \approx \Gamma_{xy} \Gamma_z = \Gamma$  (exact for  $L_a \gg \lambda$ ), and defining the average internal loss  $(\alpha_{ia} L_a + \alpha_{ip} L_p) / L$  as  $\langle \alpha_i \rangle$ , we have

$$\langle g \rangle_{th} = \Gamma g_{th} = \langle \alpha_i \rangle + \frac{1}{L} \ln\left(\frac{1}{R}\right) = \langle \alpha_i \rangle + \alpha_m \quad (2.23)$$

where  $\alpha_m \equiv (1/L) \ln(1/R)$  is the mirror loss term. Noting that the photon decay rate,  $1/\tau_p = 1/\tau_i + 1/\tau_m = v_g (\langle \alpha_i \rangle + \alpha_m)$ , Eq. (2.23) can be rewritten as

$$\Gamma g_{th} = \langle \alpha_i \rangle + \alpha_m = \frac{1}{v_g \tau_p} \quad (2.24)$$

On the other hand, for the phase part of Eq. (2.20),  $\exp(2j\beta_{tha} L_a) \exp(2j\beta_{thp} L_p) = 1$ , requires that  $\beta_{tha} L_a + \beta_{thp} L_p = m\pi$ , which gives a condition on the modal wavelength

$$\lambda_{th} = \frac{2}{m} \left[ \bar{n}_a L_a + \bar{n}_p L_p \right] \quad (2.25)$$

where  $m$  is the longitudinal mode number. It should also be realized that  $\bar{n}$  varies with wavelength ( $\partial \bar{n} / \partial \lambda$ , dispersion), and it is generally also dependent upon the carrier density ( $\partial \bar{n} / \partial n$ , plasma loading). That is, to determine  $\bar{n}$  at a wavelength  $\lambda = \lambda_0 + \Delta \lambda$  and a carrier density,  $n = n_0 + \Delta n$ , we have



$$\bar{n}(\lambda, n) = \bar{n}(\lambda_0, n_0) + \frac{\partial \bar{n}}{\partial \lambda} \Delta \lambda + \frac{\partial \bar{n}}{\partial n} \Delta n \quad (2.26)$$

Typically,  $\partial \bar{n} / \partial \lambda \sim -1 \mu m^{-1}$ , and  $\partial \bar{n} / \partial n \approx \Gamma_{xy} \partial n_A / \partial n \sim -\Gamma_{xy} 10^{-20} cm^3$ , where  $n_A$  is the index in the active region. Using Eqs. (2.25) and (2.26) we can find the wavelength separation between two modes,  $m$  and  $m+1$ , to be

$$\delta \lambda = \frac{\lambda^2}{2(\bar{n}_{ga} L_a + \bar{n}_{gp} L_p)} \quad (2.27)$$

where the group effective index for the  $j$ th section,  $\bar{n}_{gj} = \bar{n}_j - \lambda (\partial \bar{n} / \partial \lambda) = \bar{n}_j + \omega (\partial \bar{n} / \partial \omega)$ .

The group index in semiconductors is typically 20-30% larger than the index of refraction, depending on the specific wavelength relative to the band edge. From experiments, the values of  $\bar{n}_g$  for the active sections of GaAs and InGaAsP DH in-plane lasers are near 4.5 and 4, respectively.

Finally, it is important to note that the steady-state gain in a laser operating above threshold must also equal its threshold value as given by Eq. (2.23). That is, *in a laser cavity*,

$$g(I > I_{th}) = g_{th} \text{ (steady state)} \quad (2.28)$$

If the gain were higher than  $g_{th}$ , then the field amplitude would continue to increase without bound, and this clearly cannot exist in the steady state. Furthermore, since the gain is monotonically related to the carrier density, this implies that the carrier density must also *clamp* at its threshold value. That is,

$$n(I > I_{th}) = n_{th} \text{ (steady state)} \quad (2.29)$$

In fact, what happens when the current is increased to a value above threshold is that the carrier density and gain initially (for on order of a nanosecond) increase to values above their

threshold levels, and the photon density,  $S$ , grows. But then, the stimulated recombination term  $r_{st} = v_g g S$  also increases, reducing the carrier density and gain until a new steady-state dynamic balance is struck where Eqs. (2.28) and (2.29) are again satisfied. In other words, from Eq. (2.15) the stimulated recombination term  $r_{st}$  depletes all additional carrier injection above threshold. According to the reservoir analogy depicted in Fig. 2.10, the water level has reached the spillway and any further increase in input goes over the spillway without increasing the water depth. Of course, the spillway represents stimulated recombination,  $r_{st}$ . Figure 2.11 summarizes this carrier clamping effect in a laser cavity. The physics of the  $g$  vs.  $n$  curve never changes. It is noted that the feedback effect causes the carrier density to clamp, in order to keep the gain at its threshold value.

## 2.2.5 Threshold Current and Output Power vs. Current

Although the rate equations (2.15) and (2.16) are valid both above and below threshold, we shall piece together a below-threshold LED characteristic with an above-threshold laser characteristic to construct the output power vs. current in for a diode laser. The LED part is already largely complete with Eq. (2.8). Thus, we shall here concentrate on the above threshold laser part. The first step is to use the below threshold steady-state carrier rate equation, Eq. (2.5), almost at threshold. That is,

$$\frac{\eta_i I_{th}}{qV} = (r_{sp} + r_{nr} + r_l)_{th} = \frac{n_{th}}{\tau} \quad (2.30)$$

Then, recognizing that  $(r_{sp} + r_{nr} + r_l) = Bn^2 + An + Cn^3$  depends monotonically on  $n$ , from Eq. (2.29) we know that the carrier density will clamp above threshold, resulting in  $(r_{sp} + r_{nr} + r_l)$  will also clamp at its threshold value, as shown in Eq. (2.30). Thus, we can substitute Eq. (2.30) into the carrier rate equation, Eq. (2.15), to obtain a new

above-threshold carrier rate equation,

$$\frac{dn}{dt} = \eta_i \frac{(I - I_{th})}{qV} - v_g g s \quad (I > I_{th}) \quad (2.31)$$

where we have assumed  $\eta_i$  is independent of current above threshold. From Eq. (2.31), under a steady-state condition ( $d/dt = 0$ ), we can obtain photon density,  $s$ , above threshold. That is,

$$s = \frac{\eta_i (I - I_{th})}{qv_g g_{th} V} \quad (\text{steady state}) \quad (2.32)$$

When the photon density in the cavity is obtained, we can further to calculate the output power of the laser. First, we first construct the *stored optical energy in the cavity*,  $E_{os}$  by multiplying the photon density,  $s$ , by the energy per photon,  $h\nu$ , and the cavity volume,  $V_p$ . That is,  $E_{os} = sh\nu V_p$ . Then, the power lost at mirror sides is the output power obtained. Therefore, we can obtain the output power by multiplying the stored optical energy in the cavity by the *energy loss rate through the mirrors*,  $v_g \alpha_m = 1/\tau_m$ , to get the optical output power put from the mirrors,

$$P_0 = v_g \alpha_m sh\nu V_p \quad (2.33)$$

Substituting from Eqs. (2.32) and (2.24), and using  $\Gamma = V/V_p$ , in Eq. (2.33),

$$P_0 = \eta_i \left( \frac{\alpha_m}{\langle \alpha_i \rangle + \alpha_m} \right) \frac{h\nu}{q} (I - I_{th}) \quad (I > I_{th}) \quad (2.34)$$

Now, by defining

$$\eta_d = \frac{\eta_i \alpha_m}{\langle \alpha_i \rangle + \alpha_m} \quad (2.35)$$

we can simplify Eq. (2.34) to be

$$P_0 = \eta_d \frac{h\nu}{q} (I - I_{th}) \quad (I > I_{th}) \quad (2.36)$$

Equation (2.36) represents the total output power of both mirrors. If the mirrors have equal reflectivity, then exactly half will be emitted out of each. If one is totally reflecting, then all will be emitted out the other. On the other hand, if the mirrors have partial but unequal reflectivity, the fraction emitted from each is a nontrivial function. Equation (2.36) also shows that the output power above threshold is a linear function of the current above threshold. This is true regardless of our assumptions about the form of the gain-current relationship or the nature of the nonradiative recombination mechanisms. The assumptions necessary for this P-I linearity are that the gain-current relationship, the internal efficiency, the confinement factor, and the cavity losses remain constant.

To determine  $\eta_d$ , we can compare the calculated result of Eq. (2.36) to a measurement. Postulating that it might be related to a quantum efficiency, we calculate a differential quantum efficiency, defined as the number of photons out per electron in from a measured  $P$ - $I$  characteristic. As shown in Fig. 2.12, the differential quantum efficiency would be found by measuring the slope  $[\Delta P_0 / \Delta I]$  in watts/amp above threshold (including output from both ends) and then multiplying this number by  $[q/h\nu]$  in Coulombs/joule to get an empirical number of photons per electron equal to  $[\Delta P_0 / \Delta I][q/h\nu]$ .

Now, if we take the derivative with respect to current of Eq. (2.36), and solve for  $\eta_d$ , we get the same result. This shows that  $\eta_d$  is indeed *the differential quantum efficiency*.

To repeat then,

$$\eta_d = \left[ \frac{q}{h\nu} \right] \frac{dP_0}{dI} \quad (I > I_{th}) \quad (2.37)$$

The region in Fig. 2.12 below threshold ( $I < I_{th}$ ) can be approximated by neglecting the stimulated emission term in Eq. (2.16) and solving for  $s$ , again under steady-state conditions. In this case we find that

$$s = \Gamma \beta_{sp} r_{sp} \tau_p \quad (I < I_{th}) \quad (2.38)$$

Using Eqs. (2.38), (2.23), (2.6), and (2.5) in Eq. (2.33), we get the spontaneous emission into the laser mode as

$$P_0(I < I_{th}) = \eta_r \eta_i \left( \frac{\alpha_m}{\langle \alpha_i \rangle + \alpha_m} \right) \frac{h\nu}{q} \beta_{sp} I \quad (2.39)$$

Comparing this to the LED expression of Eq. (2.8) shows that  $\eta_c = \alpha_m \beta_{sp} / (\langle \alpha_i \rangle + \alpha_m)$  as might have been expected.

At threshold the spontaneous emission clamps as the carrier density clamps since  $r_{sp}$  depends upon  $n$ . Thus, as the current is increased above threshold, the spontaneous emission noise remains constant at the value of Eq. (2.39) with  $I = I_{th}$ , while the coherent stimulated emission power grows according to Eq. (2.36). This results in a gradual reduction in the linewidth of the output wavelength as the power is increased.

Equation (2.36) gives the output power in terms of the additional current applied above threshold. The proportionality factors are constants involving the cavity losses, the lasing wavelength, and the internal efficiency. To design lasers for minimum current at a given output power, we also need an analytic expression for the threshold current. We have the threshold modal gain,  $\Gamma g_{th}$ , in terms of the cavity losses [see Eq. (2.24)], and we have suggested that the gain can be related to the carrier density by either an approximate linear [see Eq. (2.17)], or more accurate logarithmic relationship. The threshold current is also related to the threshold carrier density via the recombination rates, which can be expressed as a polynomial in  $n$ , *e.g.*, Eq. (2.30).

Furthermore, it is shown that the gain vs. carrier density can be well approximated by a simple three-parameter logarithmic formula.

$$g = g'_0 \ln \frac{n + n_s}{n_{tr} + n_s} \quad (2.40)$$

In this approximation,  $g'_0$  is an empirical gain coefficient,  $n_{tr}$  is the transparency carrier density, and  $n_s$  is a shift to force the natural logarithm to be finite at  $n = 0$  such that the gain equals the unpumped absorption. However, if we restrict our attention to positive gains,  $g \geq 0$ , Eq. (2.40) can be further approximated as

$$g = g_0 \ln \frac{n}{n_{tr}} \quad (g \geq 0) \quad (2.41)$$

with a new gain coefficient  $g_0$ . In this case the differential gain,  $\partial g / \partial n = g_0 / n$ . Generally,  $n_{tr}$  and  $\partial g / \partial n$  will be quite different for bulk, quantum-well, and strained-layer quantum-well active regions. This is the basis for many of the arguments for and against certain of these structures. Figure 2.13 illustrates schematically the modal gain vs. carrier density with some of the relevant parameters labeled. The point where a line from the origin is tangent, which represents the maximum gain per unit carrier density injected, is simply given by the coordinates,  $\Gamma g_0, en_{tr}$ , with the assumed analytic approximation, Eq. (2.41).

Fitting Eq. (2.41) to numerical gain plots, a strained  $80 \text{ \AA}$  InGaAs/GaAs quantum well yields  $g_0 \sim 2100 \text{ cm}^{-1}$  and  $n_{tr} \sim 1.8 \times 10^{18} \text{ cm}^{-3}$ ; and an  $80 \text{ \AA}$  GaAs quantum well gives  $g_0 \sim 2400 \text{ cm}^{-1}$  and  $n_{tr} \sim 2.6 \times 10^{18} \text{ cm}^{-3}$ . For InP substrate cases, a strained  $30 \text{ \AA}$  InGaAs/InP gives  $g_0 \sim 4000 \text{ cm}^{-1}$  and  $n_{tr} \sim 3.3 \times 10^{18} \text{ cm}^{-3}$ ; and an unstrained  $60 \text{ \AA}$  InGaAs quantum well gives  $g_0 \sim 1800 \text{ cm}^{-1}$  and  $n_{tr} \sim 2.2 \times 10^{18} \text{ cm}^{-3}$ .

Now we can combine Eqs. (2.24) and (2.41) to get the threshold carrier density,

$$n_{th} = n_{tr} e^{g_{th}/g_0} = n_{tr} e^{(\langle\alpha_i\rangle + \alpha_m)/\Gamma g_0} \quad (2.42)$$

Using the polynomial fit for the recombination rates in Eq. (2.30), and recognizing that for the best laser material the recombination at threshold is dominated by spontaneous recombination, we have,  $I_{th} \cong B n_{th}^2 qV/\eta_i$ . Thus,

$$I_{th} = \frac{qVn_{th}}{\eta_i\tau} \cong \frac{qVBn_{tr}^2}{\eta_i} e^{2(\langle\alpha_i\rangle + \alpha_m)/\Gamma g_0} \quad (2.43)$$

where for most III-Vs of interest the bimolecular recombination coefficient,  $B \sim 10^{-10} \text{ cm}^3 / \text{ s}$ .

Equations (2.36) and (2.43) can now be used for a closed-form expression of output power vs. applied current. However, since we are usually trying to minimize the current needed for a given required power from one mirror,  $P_{01}$ , we solve for  $I$ .

$$I \cong \frac{qP_{01}(\langle\alpha_i\rangle + \alpha_m)}{F_1\eta_i h\nu\alpha_m} + \frac{qVBn_{tr}^2}{\eta_i} e^{2(\langle\alpha_i\rangle + \alpha_m)/\Gamma g_0} \quad (2.44)$$

where the first term is the additional current required above threshold to obtain power  $P_{01}$  from Eq. (2.36), and the second term is the threshold current, or Eq. (2.43). The factor  $F_1$  is the fraction of the total output power coming out of mirror 1.

Equations (2.43) and (2.44) give reasonable accuracy in simple analytic expressions which correctly show that it is always desirable to reduce the transparency value and increase the differential gain of the active material. Both points argue in favor of using quantum-well, especially strained-layer quantum-well, active regions. Relative to the cavity design, the equations also indicate that it is desirable to reduce the cavity loss  $(\langle\alpha_i\rangle + \alpha_m)$  and volume,  $V$ , subject to retaining a reasonably large confinement factor,  $\Gamma$ .

Thus, the merits of using vertical-cavity surface emitters or short-cavity in-plane lasers

with coated facets are also suggested.

Due to the exponential dependence on  $g_{th}/g_0$  in Eqs. (2.43) and (2.44), it may be beneficial to use more than one quantum well to increase  $\Gamma$  in a quantum-well laser. This dependence is a result of the saturation of the gain as the carrier density is increased to nearly fill the lowest set of states. Thus, by distributing the carriers over  $N_w$  wells, the gain per well is reduced by less than  $N_w$  times, but the modal gain is still multiplied by nearly  $N_w$  times this value. For such multiple quantum-well (MQW) lasers Eqs. (2.43) and (2.44) are still valid but one must be sure to multiply the single-well confinement factor,  $\Gamma_1$ , and volume,  $V_1$ , by the number of wells,  $N_w$ . That is, for an MQW laser, from Eq. (2.43) or the second term in Eq. (2.44), one can explicitly write

$$I_{thMQW} \cong \frac{qN_w V_1 B n_{tr}^2}{\eta_i} e^{2(\langle\alpha_i\rangle + \alpha_m)/N_w \Gamma_1 g_0} \quad (2.45)$$

Here, we have assumed a separate confinement waveguide, so that the optical mode does not change significantly as more wells are added. Also, the number of wells is limited to the number that can be placed near the maximum of the optical mode. The optimum number of wells is the number that minimizes Eq. (2.45), neglecting nonradiative recombination. With the increased confinement factor we also see that higher powers can be obtained efficiently without moving too far up the gain curve.

If nonradiative recombination is important at threshold, an additional nonradiative threshold current component must be added as outlined earlier. For the long-wavelength InGaAsP/InP materials, nonradiative recombination is known to be very important. In fact, were it not for such recombination, the threshold current densities of lasers using such materials would be lower than those using GaAs quantum wells, as indicated by the gain parameters listed after Eq. (2.41). If such higher-order nonradiative carrier recombination is important at threshold, one must add another component to the threshold



current due to the  $Cn_{th}^3$  term in the recombination rate. Then, Eqs. (2.43) and (2.44) should be increased by

$$I_{nr_{th}} \cong \frac{qVCn_{tr}^3}{\eta_i} e^{3(\langle\alpha_i\rangle+\alpha_m)/\Gamma g_0} \quad (2.46)$$

where for  $1.3 \mu\text{m}$  InGaAsP material, the Auger coefficient,  $C \sim 3 \times 10^{-29} \text{cm}^6/\text{s}$ , and for  $1.55 \mu\text{m}$  material it is about two or three times larger. The cubic dependence on  $n_{th}$  places more importance on reducing the threshold carrier density in this material system. In fact, this additive Auger term dominates Eq. (2.43) for carrier densities above  $n_{th} \sim 3 \times 10^{18}$  or  $n_{th} \sim 1.5 \times 10^{18} \text{cm}^{-3}$  at  $1.3$  and  $1.55 \mu\text{m}$ , respectively. This fact focuses more attention on reducing cavity losses,  $(\langle\alpha_i\rangle + \alpha_m)$ , and maintaining a large confinement factor,  $\Gamma$ . With the use of strained-layer InGaAs/InGaAsP or InGaAs/InGaAlAs quantum wells on InP, a considerable improvement is possible, since all the parameters affecting  $n_{th}$  move in the right direction. In fact, the Auger coefficient,  $C$ , may also be reduced due to the splitting of the valence bands.

## 2.2.6 Relaxation Resonance and Frequency Response

Here, we use Eqs. (2.15) and (2.16)

$$\frac{dn}{dt} = \frac{\eta_i I}{qV} - \frac{n}{\tau} - \nu_g g S \quad (2.15)$$

$$\frac{ds}{dt} = \Gamma \nu_g g S + \Gamma \beta_{sp} r_{sp} - \frac{s}{\tau_p} \quad (2.16)$$

to briefly outline the calculation of relaxation resonance frequency and its relationship to laser modulation bandwidth. In fact, because of gain compression with increasing photon density and possible transport effects, the calculations here are a bit

oversimplified, particularly with respect to quantum-well structures. However, these simple equations do seem to work well for standard DH structures, and the method of attack for calculating resonance frequency is also instructive for the more complex calculations.

Consider the application of an above-threshold dc current,  $I_0$ , superimposed with a small ac current,  $I_1$ , to a diode laser. Then, under steady-state conditions the laser's carrier density and photon density would respond similarly, with some possible harmonics of the drive frequency,  $\omega$ , that we shall ignore. Using complex frequency domain notation,

$$\begin{aligned} I &= I_0 + I_1 e^{j\omega t} \\ n &= n_0 + n_1 e^{j\omega t} \\ s &= s_0 + s_1 e^{j\omega t} \end{aligned} \quad (2.47)$$

Before applying these to Eqs. (2.15) and (2.16), we first rewrite the rate equations using Eq. (2.17) for the gain. This is valid since small-signal conditions are assumed and the gain can be well approximated as a straight line over some distance, *provided the local slope is used*. We also assume the dc current is sufficiently far above threshold that the spontaneous emission can be neglected. That is,

$$\frac{dn}{dt} = \frac{\eta_i I}{qV} - \frac{n}{\tau} - v_g a(n - n_{tr}) s \quad (2.48)$$

$$\frac{ds}{dt} = \Gamma v_g a(n - n_{tr}) s - \frac{s}{\tau_p} \quad (2.49)$$

Now, after plugging in Eqs. (2.47) for  $I$ ,  $n$ , and  $s$ , we recognize that the dc components satisfy the steady-state versions of Eqs. (2.48) and (2.49), *i.e.*, with  $d/dt \rightarrow 0$ ; and they can be grouped together and set to zero. Next, we recognize that the steady-state gain factors,  $a(n - n_{tr})$  are just equal to  $g_{th}$ , and can be replaced by  $[\Gamma v_g \tau_p]^{-1}$  according to Eq. (2.23).

Finally, we delete the second-harmonic terms that involve  $e^{j2\omega t}$ , and divide out an  $e^{j\omega t}$  common factor. Then,

$$j\omega n_1 = \frac{\eta_i I_1}{qV} - \frac{n_1}{\tau} - \frac{s_1}{\Gamma \tau_p} - v_g a n_1 s_0 \quad (2.50)$$

$$j\omega s_1 = \Gamma v_g a n_1 s_0 \quad (2.51)$$

With the above manipulations we have generated frequency domain equations which can easily be solved for the transfer function  $s_1(\omega)/I_1(\omega)$ .

Before solving for the transfer function, let's briefly examine the coupling between the small-signal photon density,  $s_1$ , and the small-signal carrier density,  $n_1$ . The carrier density  $n_1$  depends on  $s_1$  through the third term in Eq. (2.50), while the photon density  $s_1$  depends on  $n_1$  through Eq. (2.51). If we view the left-hand sides of these two equations as time derivatives, then we observe from Eq. (2.51) that as  $n_1$  increases and becomes positive,  $s_1$  increases in time due to increased gain in the laser. However, from the third term in Eq. (2.50), once  $s_1$  becomes positive, it serves to decrease  $n_1$ , through increased stimulated emission. As  $n_1$  decreases and becomes negative,  $s_1$  begins to fall, and once it becomes negative, it again produces an increase in  $n_1$ . At this point, the cycle repeats itself. This phenomenon produces a natural resonance in the laser cavity which shows up as a ringing in the output power of the laser in response to sudden changes in the input current. The natural frequency of oscillation associated with this mutual dependence between  $n_1$ , and  $s_1$ , can be found by multiplying Eqs. (2.50) and (2.51) together, ignoring all but the third term on the right-hand side of the first equation:

$$\omega_R^2 = \frac{v_g a S_0}{\tau_p} \quad (2.52)$$

This natural resonance frequency is commonly referred to as the *relaxation resonance frequency*,  $\omega_R$  (where *relaxation* refers to an attempt by the photons and carriers to relax to their steady-state values). It is directly proportional to the square root of the differential gain,  $a$ , and average photon density,  $S_0$ , in the cavity (output power), and inversely proportional to the square root of the photon lifetime in the cavity.

The relaxation resonance of the laser cavity is much like the natural oscillation of an *LC* circuit. However, the additional terms present in Eq. (2.50) lead to more of an *RLC* circuit behavior, dampening the resonant response. The overall modulation frequency response including these terms is governed by the small-signal transfer function,  $s_1(\omega)/I_1(\omega)$ . Solving for  $n_1$  in Eq. (2.51), we have  $n_1 = j\omega s_1/\Gamma v_g a s_0$ . Then eliminating  $n_1$  from Eq. (2.50), and using  $P_{ac} = v_g \alpha_m s_1 h\nu V_p$ , we obtain

$$\frac{P_{ac}(\omega)}{I_1(\omega)} = \frac{\eta_i h\nu}{q} \frac{v_g \alpha_m (v_g a S_0)}{v_g a S_0/\tau_p - \omega^2 + j\omega [v_g a S_0 + 1/\tau]} \quad (2.53)$$

Setting  $v_g a S_0 = \omega_R^2 \tau_p$  and using Eqs. (2.24) and (2.35) the transfer function can be written in another form:

$$\frac{P_{ac}(\omega)}{I_1(\omega)} = \frac{\eta_d h\nu/q}{1 - (\omega/\omega_R)^2 + j(\omega/\omega_R) [\omega_R \tau_p + 1/\omega_R \tau]} \quad (2.54)$$

For sufficiently low modulation frequencies, the denominator reduces to one and Eq. (2.54) reduces to the ac equivalent of Eq. (2.36). For higher modulation frequencies, the  $1 - (\omega/\omega_R)^2$  term in the denominator creates a strong resonance in the response. Figure 2.14 illustrates the frequency dependence for a wide range of output powers. Note that the resonance is damped at low and high output powers. This occurs because the

imaginary damping term in Eq. (2.54) depends on both  $\omega_R$  and  $1/\omega_R$ . In fact, we will find that inclusion of gain compression and transport effects creates significantly more damping than predicted here. On real laser devices the resonance is typically limited to 5—10 dB (as opposed to the peak ~25 dB suggested in Fig. 2.14).

Beyond the strong resonance, the transfer characteristics degrade significantly. Thus, effective modulation of the output power can only be achieved over a modulation bandwidth of  $\sim \omega_R$ . When the damping is small, the electrical 3 dB down frequency ,

*i.e.*, the frequency which reduces the received *electrical* power to one-half its dc value, is

given by  $\omega_{3\text{dB}} = \sqrt{1 + \sqrt{2}} \omega_R$ . Expanding Eq. (2.52) using Eqs. (2.24), (2.33), and (2.35),

we can express this result in terms of the output power:

$$f_{3\text{dB}} \approx \frac{1.55}{2\pi} \left[ \frac{\Gamma v_g a \eta_i}{h\nu V \eta_d} \right]^{1/2} \sqrt{P_0} \quad (\text{small damping}) \quad (2.55)$$

The modulation bandwidth of the laser can be steadily enhanced by increasing the output power. However, increased damping of the resonance at high powers, thermal limitations, and high-power mirror facet damage set practical limits on the maximum average operating power we can use.

Since thermal limits are usually associated with the drive current, it is also convenient to express  $\omega_R$  in terms of current. Using Eq. (2.32) for  $s_0$ , with  $g_{th}$ , given by Eq. (2.24), Eq. (2.52) becomes

$$\omega_R = \left[ \frac{\Gamma v_g a}{qV} \eta_i (I - I_{th}) \right]^{1/2} \quad (2.56)$$

In this form we observe that it is desirable to enhance the differential gain, minimize the volume of the mode ( $\Gamma/V = 1/V_p$ ), and maximize the current relative to threshold for maximum bandwidth. If we want to keep the overall drive current low, then we should

also try to minimize the threshold current, perhaps by increasing the facet reflectivity. If, however, we are more concerned about keeping the photon density low (for example, to reduce the risk of facet damage), then from (2.52) we should try to decrease the photon lifetime instead, perhaps by *decreasing* the facet reflectivity [refer to Eq. (2.24)].

Thus, the optimum cavity design for a high-speed laser depends on what constraints we place on the device operation. In fact, it is found that at very high powers, the maximum bandwidth actually becomes independent of  $\omega_R$ , and is more fundamentally related to the damping factor (the K-factor) which is affected by gain compression and transport effects.

## 2.3 Threshold Current Reduction Under External Light

### Injection

As mentioned in the introduction, in 1994, Li [117] predicted that the gain is enhanced and hence threshold is decreased by including the spontaneous emission term. Later on, in 1998, Sivaprakasam and Singh [118] demonstrated the threshold current reduction experimentally by using two identical, single mode AlGaAs laser diodes (SDL 5412-H1,  $\lambda=850$  nm ). Following the derivations given above, we will derive the expression about the threshold current reduction under injection locking condition.

From Eq. (2.43), in a free-running condition, the threshold current of diode lasers can be written as

$$I_{th} = \frac{qVn_{th}}{\eta_i\tau} \quad (2.43)$$

Herein, we introduce the concept of the gain compression [120]. The normalized gain of a free-running semiconductor laser can be written as

$$\begin{aligned}
G(n, S) &= \frac{\partial g}{\partial n} v_g \tau_p (n - n_{tr})(1 - k_s S) \\
&= G_n (n - n_{tr})(1 - k_s S)
\end{aligned} \tag{2.57}$$

where  $n$  is the carrier density in the active region,  $\partial g/\partial n$  is the gain coefficient,  $v_g$  is the group velocity of light,  $\tau_p$  is the photon lifetime, and  $n_{tr}$  is the transparent carrier density. The gain is also related to the photon number  $S$ , in the laser cavity and  $k_s$  is the nonlinear gain coefficient.

Due to the influence of spontaneous emission, the normalized gain is always less than unity, regardless of whether the laser is biased below or above threshold [120]. This gain difference can be then expressed as

$$D_g = G(n, S) - 1 \tag{2.58}$$

When external light is injected into the laser, we assume that the carrier density is  $n_{ui}$  and that the photon number is  $S_{ui}$ . Then, the normalized gain is

$$G(n_{ui}, S_{ui}) = G_n (n_{ui} - n_{tr})(1 - k_s S_{ui}) \tag{2.59}$$

Under an injection-locking condition, the laser is biased at or above threshold. Therefore, the gain can be approximately given as [113, 120]

$$\begin{aligned}
G(n_{ui}, S_{ui}) &\approx G_n (n_{th} - n_{tr}) + \delta G \\
&= 1 + G_n \Delta n - k_s \Delta S
\end{aligned} \tag{2.60}$$

where  $n_{th}$  is the threshold carrier density of the free-running laser,  $\Delta n = n_{ui} - n \approx n_{ui} - n_{th}$  is the carrier density change due to external light injection, and  $\Delta S = S_{ui} - S$ . In this case, we have  $|\delta G| \ll 1$ . Thus, it is possible to apply small-signal analysis. However, in our case, the laser may be biased below threshold. Normally, Eq. (2.60) cannot be applied to this condition. Fortunately, semiconductor lasers applied to actual systems are not biased far below threshold (for example, higher than 95 percent of their threshold). Therefore, we can

use small-signal analysis in the following way:

$$\begin{aligned} G(n_{ui}, S_{ui}) &\approx 1 + D_g + \delta G \\ &= 1 + D_g + G_n \Delta n - G(n, S) k_s \Delta S \end{aligned} \quad (2.61)$$

to include the deviation from threshold, if the injected power is not very large so that  $|\delta G| \ll 1 + D_g$ . In this section, we shall show that this condition can be satisfied for most actual cases.

If the cavity resonance frequency of a free-running laser corresponding to the threshold carrier density  $n_{th}$  is  $\omega_{th}$ , according to Eqs. (2.57) and (2.58), the cavity frequency  $\omega(n)$  corresponding to the carrier density  $n$  should obey [120]

$$\omega(n) = \omega_{th} + \alpha D_g / 2\tau_p \quad (2.62)$$

if the laser is not biased far below threshold, where  $\alpha$  is the linewidth enhancement factor. As discussed above, when Eq. (2.61) is satisfied, the cavity frequency  $\omega(n_{inj})$  considering external light injection is [108, 113, 120, 121]

$$\omega(n_{ui}) = \omega_{th} + \alpha (D_g + G_n \Delta n) / 2\tau_p \quad (2.63)$$

Equations (2.61) and (2.63) are two basic equations for our analysis.

Furthermore, by using Eqs. (2.57), (2.58) and (2.62), the electric field  $E$  of a free-running laser can be written as [120]

$$\begin{aligned} \frac{dE}{dt} &= \left\{ j[\omega(n) - \omega_{th}] + \frac{[G(n, S) - 1]}{2\tau_p} \right\} E + E_{sp} \\ &= (1 + j\alpha) D_G E / 2 + E_{sp} \end{aligned} \quad (2.64)$$

where  $D_G = D_g / \tau_p$ . The spontaneous emission is accounted for by the noise term  $E_{sp}$ , which is assumed to be a white Gaussian process with the spectral density  $R_{sp}$ , which can be obtained from Eq. (2.16)



$$\begin{aligned}
\frac{d(s \cdot V)}{dt} &= \Gamma v_g g s V + \Gamma \beta_{sp} r_{sp} V - \frac{s}{\tau_p} V \\
\Rightarrow \frac{dS}{dt} &= \Gamma v_g g S + \Gamma \beta_{sp} r_{sp} V - \frac{S}{\tau_p} \\
&= S \left( \Gamma v_g g - \frac{1}{\tau_p} \right) + \Gamma \beta_{sp} r_{sp} V \\
&= S \left( R_{st} - \frac{1}{\tau_p} \right) + R_{sp}
\end{aligned} \tag{2.65}$$

For the same reason, considering (2.61) and (2.63), the slowly varying amplitude of the complex electric field  $E$  in a semiconductor laser with external light injection obeys [108, 113, 120]

$$\begin{aligned}
\frac{dE_{ui}}{dt} &= \left\{ j \left[ \omega(n_{ui}) - \omega_{th} - \Delta\omega_0 \right] + \frac{[G(n_{ui}, S_{ui}) - 1]}{2\tau_p} \right\} \bullet E_{ui} + k_c \bullet E_i + E_{sp} \\
&= \left\{ j \left[ \frac{\alpha(D_G + G_N \Delta N)}{2} - \Delta\omega_0 \right] + \frac{T_G}{2} \right\} \bullet E_{ui} + k_c \bullet E_i + E_{sp}
\end{aligned} \tag{2.66}$$

with

$$\begin{aligned}
\Delta G &= \frac{\delta G}{\tau_p} = \frac{G_n \Delta n - G(n, S) k_s \Delta S}{\tau_p} \\
&= \frac{G_n}{\tau_p V} (\Delta n \cdot V) - \frac{G(n, S) k_s}{\tau_p} \Delta S \\
&= G_N \bullet \Delta N - G_S \bullet \Delta S
\end{aligned} \tag{2.67}$$

the gain change due to external light injection, and

$$T_G = D_G + \Delta G \tag{2.68}$$

the total gain difference of the laser from the threshold value  $1/\tau_p$ , where

$G_N = G_n/\tau_p V$ ,  $G_S = G(n, S)k_s/\tau_p$ ,  $\Delta N = \Delta n \cdot V$  is the carrier number change due to optical

injection,  $V$  is the volume of the active region,  $\Delta\omega_0$  is the angular frequency detuning between

the free-running laser and the external field  $E_i$ , and  $k_c$  is the coupling coefficient.

To include the possible excitation of the neighboring mode with increasing detuning, we present a rate equation for the photon number  $S_p$  in that mode (unlocked mode) as [108]

$$\frac{dS_p}{dt} = \frac{(G-1) \cdot S_p}{\tau_p} + R_{sp} = T_G \cdot S_p + R_{sp} \quad (2.69)$$

Actually, the gain in this mode is different from that in the locked mode. However, to simplify the problem, we assume that they are the same, as done in [108, 113, 114, 121, 122].

The equation for the carrier number  $N_{ui} = n_{ui}V$  in the active region is

$$\frac{dN_{ui}}{dt} = \frac{I}{q} - R(N_{ui}) - \frac{GS_{ui}}{\tau_p} \quad (2.70)$$

where  $S_{ui} = |E_{ui}|^2 + S_p = S_L + S_p$ .

To compare the theory with experiments, we use the following notation for the carrier recombination effect. That is,  $R(N) = A'N + B'N^2 + C'N^3$  with  $A'$ ,  $B'$ , and  $C'$  being the nonradiative, radiative, and Auger recombination coefficients, respectively [114]. The spontaneous emission rate in Eqs. (2.64), (2.66), and (2.69) can therefore be represented as  $R_{sp} = \Gamma\beta_{sp}r_{sp}V = \Gamma\beta_{sp}Bn^2V = \Gamma\beta_{sp}B'N^2V$ .

As discussed above, when the external field is injected, the carrier number is changed from its free-running value  $N = nV$  by  $\Delta N$ . Therefore, according to Eq. (2.70), the equation for  $\Delta N$  is

$$\frac{d(\Delta N)}{dt} = -\Delta S \left( \frac{1}{\tau_p} + D_G + G_N \Delta N - G_S S_{ui} \right) - \frac{\Delta N}{\tau_e} \quad (2.71)$$

where  $1/\tau_e = 1/\tau_{\Delta N} + G_N S$  with  $\tau_{\Delta N} = 1/(A' + 2B'N + 3C'N^2)$  being the *differential carrier lifetime*.

The static properties of the laser can be obtained according to Eqs. (2.66), (2.69), and (2.71), assuming  $\frac{d(\Delta N)}{dt} = \frac{dE_{ui}}{dt} = \frac{dS_p}{dt} = 0$  [108, 113, 121, 122]. The real and imaginary parts of Eq.

(2.66) can be written together as

$$\frac{(T_G + R_{sp}/S_L)^2}{4} + \left[ \frac{\alpha(D_G + G_N \Delta N)}{2} - \Delta\omega_0 \right]^2 = \frac{k_c^2 |E_i|^2}{|E_{ii}|^2} = k_c^2 \frac{S_i}{S_L} = S_{iL} \quad (2.72)$$

where  $S_{iL}$  determines the relative strength of the injection. Equation (2.72) is an expression for  $\Delta N$ . Formally, the solution of Eq. (2.72) is

$$\begin{aligned} & D_G + G_N \Delta N \\ &= \frac{2}{1 + \alpha^2} \left[ \alpha \Delta\omega_0 - \frac{(R_{sp}/S_L - G_S \Delta S)}{2} \pm \sqrt{(1 + \alpha^2) K - \left( \Delta\omega_0 + \alpha \frac{(R_{sp}/S_L - G_S \Delta S)}{2} \right)^2} \right] \end{aligned} \quad (2.73)$$

According to Eq. (2.73), it is clear that  $\Delta N$  has two possible solutions for each value of  $\Delta\omega_0$ . Also, this indicates that the gain change  $\Delta G$  will have two roots. These two roots give rise to optical bistability, as predicted in [123, 124].

As discussed above, small-signal analysis is valid only if the normalized gain change  $\delta G$  is much less than the normalized gain  $1 + D_g$  [see Eq. (2.61)]. Therefore, we present some discussion for the maximum gain change  $\delta G_m$  due to external light injection. Of course, if  $|\delta G_m| \ll 1 + D_g$  is satisfied, we can apply small-signal analysis.

The discriminant for Eq. (2.72) should not be less than zero because  $\Delta N$  must be real. That is, the angular frequency detuning  $\Delta\omega_0$  must satisfy

$$(1 + \alpha^2) S_{iL} - \left( \alpha \frac{(G_S \Delta S - R_{sp}/S_L)}{2} - \Delta\omega_0 \right)^2 \geq 0 \quad (2.74)$$

Obviously, the gain change  $\Delta G$  reaches its maximum when the frequency detuning  $\Delta f_0 = \Delta\omega_0/2\pi$  becomes [113]

$$\Delta f_l = \left[ \frac{\alpha(G_S \Delta S - R_{sp}/S_L)}{2} - k_c \sqrt{(1 + \alpha^2) \frac{S_i}{S_L}} \right] / 2\pi \quad (2.75)$$

This frequency  $\Delta f$  is called the lower limit of the frequency detuning [113]. Also, the maximum gain change due to external light injection, by substituting Eq. (2.75) into Eq.

(2.73), is

$$\begin{aligned}\Delta G_m &= G_N \Delta N_m - G_S \Delta S_m \\ &= -D_G - \frac{R_{sp}}{S_{Lm}} - \sqrt{\frac{4\alpha^2 k_c^2 S_i}{(1+\alpha^2) S_{Lm}}}\end{aligned}\quad (2.76)$$

where subscript  $m$  means the values corresponding to the maximum gain change.

When the gain difference  $D_G$  from the threshold value  $1/\tau_p$  is taken into consideration by moving the term  $-D_G$  to the left-hand side of Eq. (2.76) [see Eq. (2.77)], the total gain difference  $T_G = D_G + \Delta G$  from the threshold value can be increased by the external light injection locking. It is noted that the gain difference  $D_G$  is important only for the free-running laser biased below or far above threshold.

$$\begin{aligned}T_G &= D_G + \Delta G_m = D_G + G_N \Delta N_m - G_S \Delta S_m \\ &= -\frac{R_{sp}}{S_{Lm}} - \sqrt{\frac{4\alpha^2 k_c^2 S_i}{(1+\alpha^2) S_{Lm}}}\end{aligned}\quad (2.77)$$

Thus, the total gain difference  $T_G$  will be increased under the condition external injection locking. Furthermore, we rewrite Eq. (2.77) by adding the loss rate  $1/\tau_p$  to both sides of it:

$$\begin{aligned}\underbrace{g}_{\text{Threshold gain for the injection-locked laser}} &= \underbrace{1/\tau_p}_{\text{Cavity loss rate for the free-running laser}} + \underbrace{T_G}_{\text{Total gain difference under external injection locking}} \\ &= 1/\tau_p + D_G + \Delta G_m \\ &= 1/\tau_p + D_G + G_N \Delta N_m - G_S \Delta S_m \\ &= \frac{1}{\tau_p} - \frac{R_{sp}}{S_{Lm}} - \sqrt{\frac{4\alpha^2 k_c^2 S_i}{(1+\alpha^2) S_{Lm}}}\end{aligned}\quad (2.78)$$

The first term on right-hand side of Eq. (2.78) is the cavity loss rate for the free-running laser. The second term represents the influence of spontaneous emission. The last term represents the effect of external light injection on the threshold. We can see that its role is to reduce the threshold. According to the prediction by Sharfin and Dagenais [116], the optical injection can only decrease the gain from the zero field value but optical injection does not lower the

lasing threshold. In their model, they had calculated the threshold using the rate equation approach, neglecting the spontaneous emission part. However, by including the spontaneous emission part into the rate equation, we can find, from Eq. (2.78), that the threshold gain is reduced by external light injection from  $1/\tau_p$  (free-running condition) to  $\left[1/\tau_p - R_{sp}/S_{Lm} - \sqrt{4\alpha^2 k_c^2 S_i / (1 + \alpha^2) S_{Lm}}\right]$  (externally light injecting condition). Therefore, under external light injection the threshold gain is indeed reduced.

Finally, according to Eq. (2.57), the normalized gain at threshold current can be expressed as

$$\begin{aligned}
 G(n_{th}, S_{th}) &= \frac{\partial g}{\partial n} v_g \tau_p (n_{th} - n_{tr})(1 - k_s S) \\
 &\approx \frac{\partial g}{\partial n} v_g \tau_p (n_{th} - n_{tr}) \\
 &= G_n (n_{th} - n_{tr}) \\
 \Rightarrow n_{th} &= \frac{G(n_{th}, S_{th})}{G_n} + n_{tr}
 \end{aligned} \tag{2.79}$$

By combing Eqs. (2.78), (2.79) and (2.43), we can obtain the threshold current under external light injection  $I_{th,ui}$

$$\begin{aligned}
 I_{th,ui} &= \frac{qV}{\eta_i \tau} n_{th,ui} = \frac{qV}{\eta_i \tau} \left( \frac{v_g}{G_n} - \frac{\left( \frac{R_{sp}}{S_{Lm}} + \sqrt{\frac{4\alpha^2 k_c^2 S_i}{(1 + \alpha^2) S_{Lm}}} \right) \cdot v_g \tau_p}{G_n} + n_{tr} \right) \\
 &= \frac{qV}{\eta_i \tau} \left( \frac{v_g}{a v_g \tau_p} + n_{tr} \right) - \frac{qV}{\eta_i \tau} \frac{v_g \tau_p}{a v_g \tau_p} \left( \frac{R_{sp}}{S_{Lm}} + \sqrt{\frac{4\alpha^2 k_c^2 S_i}{(1 + \alpha^2) S_{Lm}}} \right) \\
 &= \frac{qV}{\eta_i \tau} \left( \frac{g_{th}}{a} + n_{tr} \right) - \frac{qV}{\tau \eta_i a} \left( \frac{R_{sp}}{S_{Lm}} + \sqrt{\frac{4\alpha^2}{(1 + \alpha^2)}} \sqrt{S_{iLm}} \right) \\
 &= I_{th, free-running} - \Delta I_{injection}
 \end{aligned} \tag{2.80}$$

It is noted that the threshold gain  $g$  in Eq. (2.78) is divided by  $(1/v_g \tau_p)$  for normalization.

Equation (2.80) accounts for the reduction of the threshold current under external light injection. We can also find that the magnitude of the reduced threshold current is related to the injection strength factor  $S_{iLm}$ .

In our operating condition, the FPLD is injection-locked at its threshold current. Therefore, it is easy to obtain very large value of  $S_{iLm}$ . By using the typical parameter values for a buried-heterostructure laser, we can obtain that if the power inside the FPLD is  $2.25 \mu\text{W}$ , the reduction of 3 mA under injection power of 7 dBm can be achieved. The detailed parameters are listed in Table 2.1. These parameters show that the FPLD biased at threshold current and the very strong injection locking both cause the threshold current reduction.



**Table 2.1**

Typical parameter values for a 1.55  $\mu\text{m}$  semiconductor laser in a injection-locking condition

Symbol	Parameters	Typical Values	Units
I	Injection current		Amp
q	Unit charge of electron	1.6e-19	Coulomb
d	Thickness of active region	0.2	$\mu\text{m}$
w	Width of active region	2	$\mu\text{m}$
L	Length of active region	250	$\mu\text{m}$
$V=dwL$	Volume of active region		$\text{cm}^3$
$\alpha_m$	Facet loss	45	$\text{cm}^{-1}$
$\Gamma=V/V_p$	Optical confinement factor	0.5	
$V_p=V/\Gamma$	The cavity volume occupied by photons		$\text{cm}^3$
$\beta_{sp}$	The spontaneous emission factor	1e-3	
R	Reflection coefficient of mirror	0.308	
$v_g$	Group velocity	8.57e9	cm/sec
$\tau_p$	Photon lifetime	1.6e-12	sec
$g_{th}$	Threshold gain	$1/(\Gamma v_g \tau_p)=145.9$	$\text{cm}^{-1}$
$\tau$	Carrier lifetime at threshold	2e-9	sec
$R_{sp}$	The spontaneous emission rate	$\Gamma \beta_{sp} B n_{th}^2 V = 1.254e13$	$\text{sec}^{-1}$
$I_{th,free-running}$	Threshold current	12.67	mA
$\alpha$	Linewidth enhancement factor	5	
$P_0$	Total output power	100	$\mu\text{W}$
$S_{Lm}$	Photon number in the locked mode	1.011e13	
$S_{iLm}$	Relative injection strength	33.5	dB
$\Delta I_{injection}$	Threshold current reduction due to injection locking	3	mA

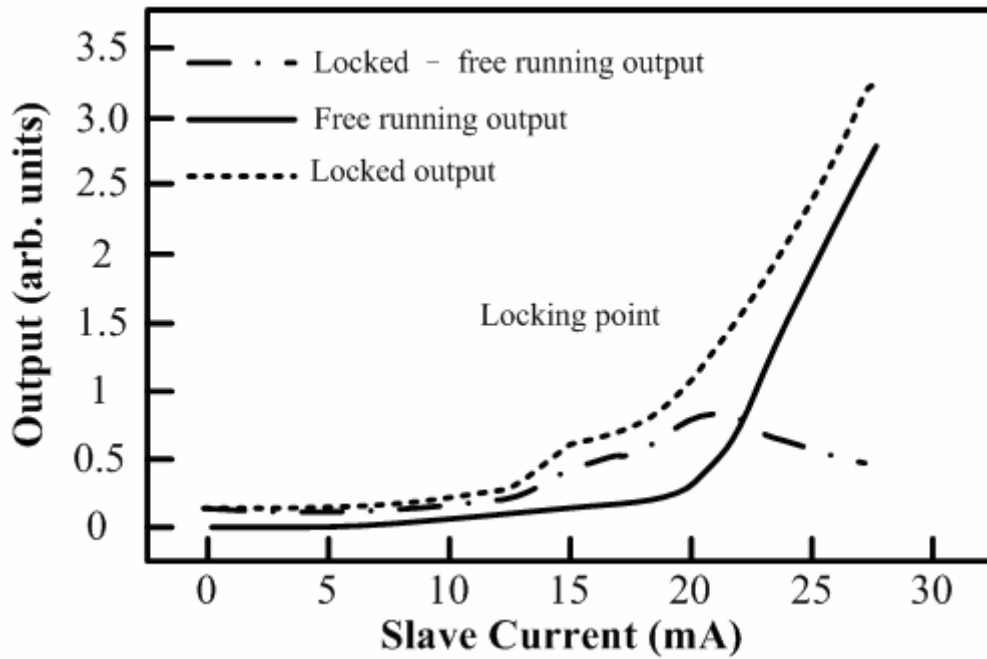


Fig. 2.1 Light-current graph for free running, injected locked laser and the difference of the two.

[S. Sivaprakasam and Ranjit Singh, "Gain change and threshold reduction of diode laser by injection locking," *Optics Communications*, **151**, 253 (1998).]

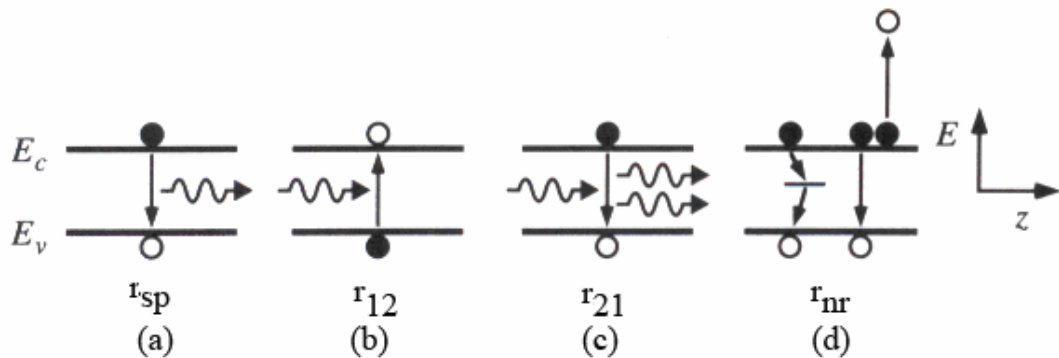


Fig. 2.2 Electronic transitions between the conduction and valence bands. The first three (a-c) represent radiative transitions in which the energy to free or bind an electron is supplied by or given to a photon. The fourth illustrates two nonradiative processes.

[L. A. Coldren, and S. W. Corzine, *Diode Lasers and Photonic Integrated Circuits*, New York: Wiley Interscience, 1995.]



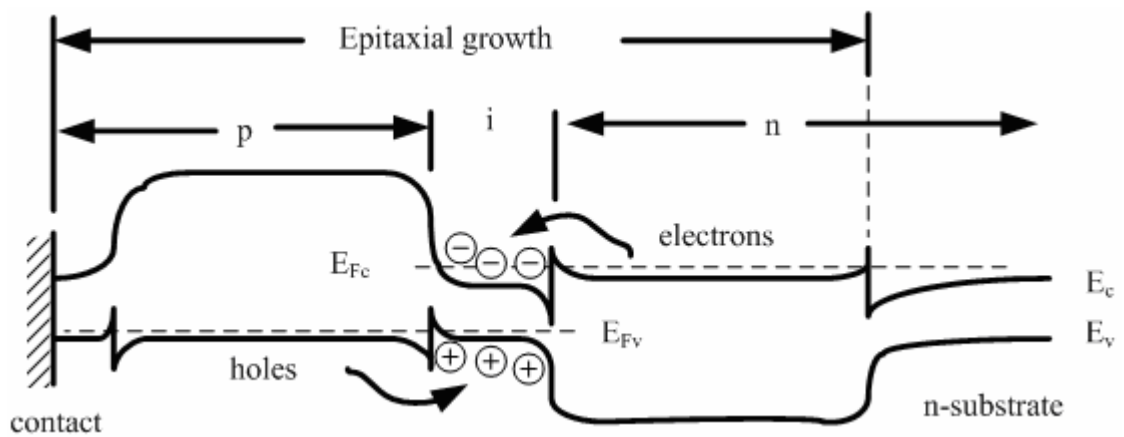


Fig. 2.3 Band diagram of forward biased double-heterostructure diode.

[L. A. Coldren, and S. W. Corzine, *Diode Lasers and Photonic Integrated Circuits*, New York: Wiley Interscience, 1995.]

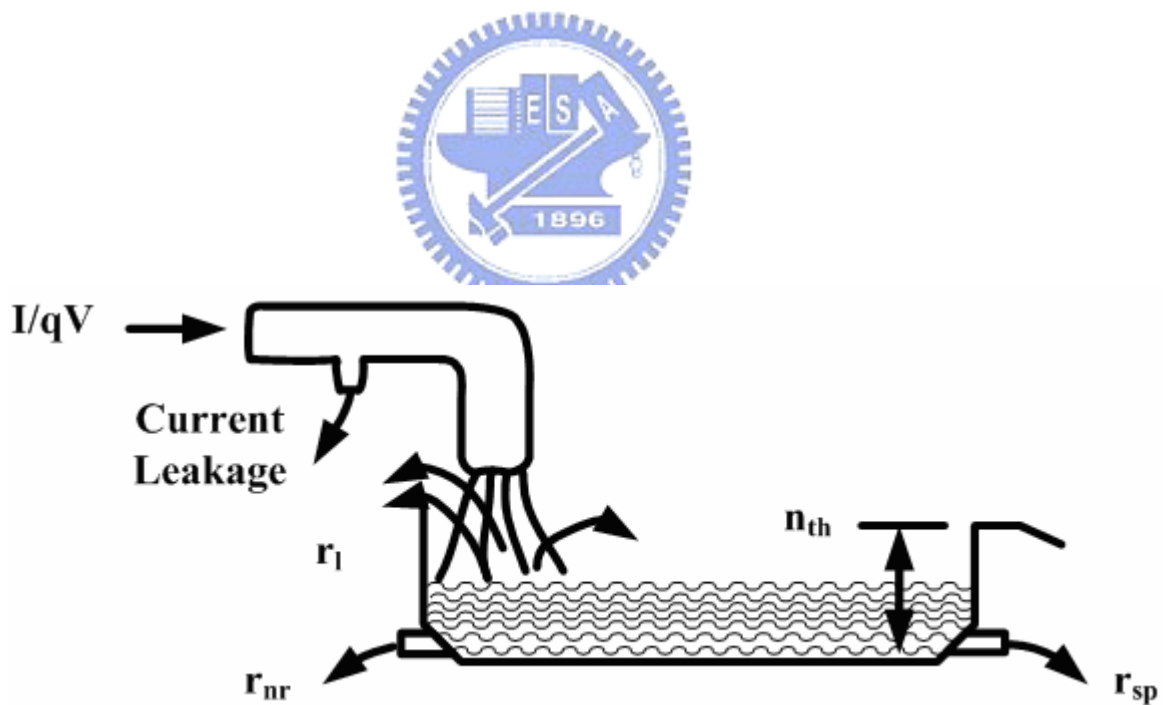


Fig. 2.4 Reservoir with continuous supply and leakage as an analog to a DH active region with current injection for carrier generation and radiative and nonradiative recombination (LED or laser below threshold).

[L. A. Coldren, and S. W. Corzine, *Diode Lasers and Photonic Integrated Circuits*, New York: Wiley Interscience, 1995.]

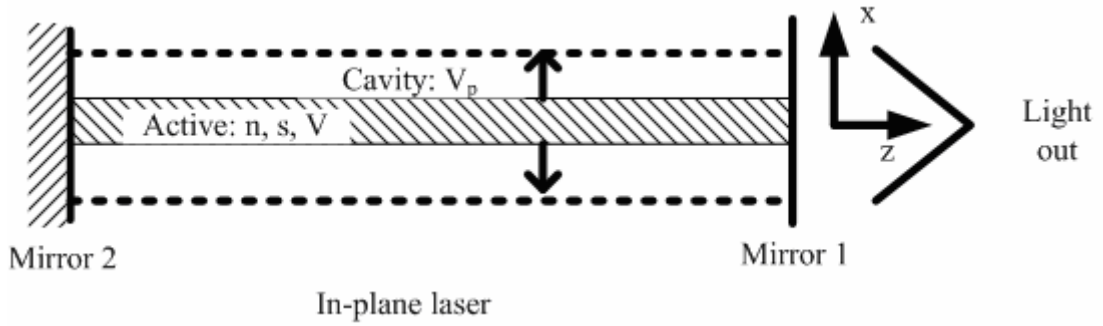


Fig. 2.5 Schematics of in-plane and vertical-cavity lasers illustrating the active (cross-hatched) and cavity (within dashed lines) volume as well as the coordinate systems.  
 [L. A. Coldren, and S. W. Corzine, *Diode Lasers and Photonic Integrated Circuits*, New York: Wiley Interscience, 1995.]

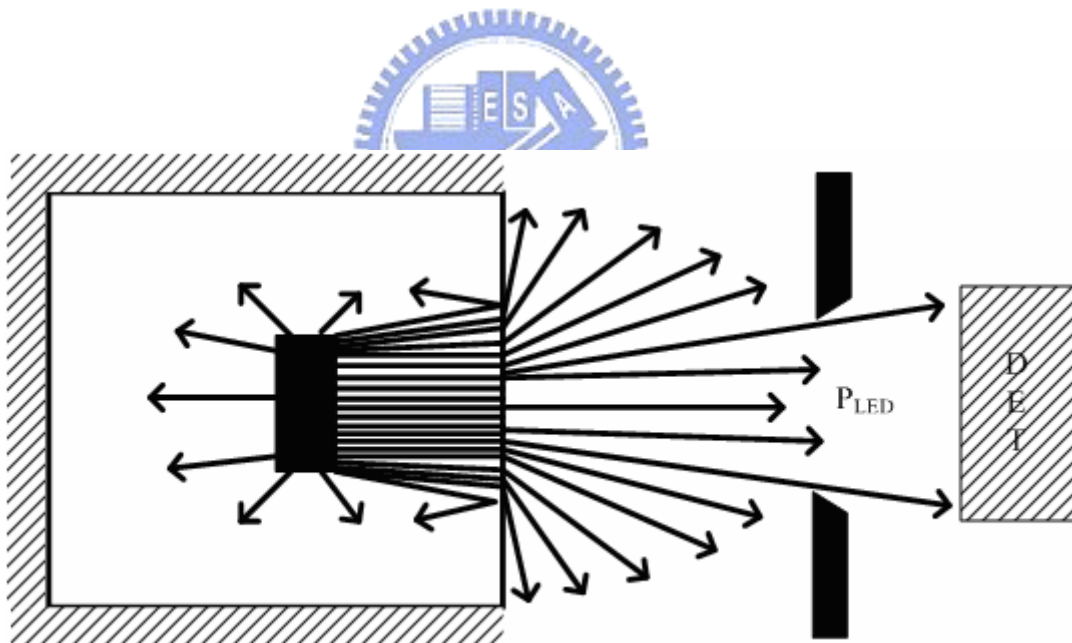


Fig. 2.6 Schematic of LED showing how only a small portion of the generated light reaches a desired detector.  
 [L. A. Coldren, and S. W. Corzine, *Diode Lasers and Photonic Integrated Circuits*, New York: Wiley Interscience, 1995.]

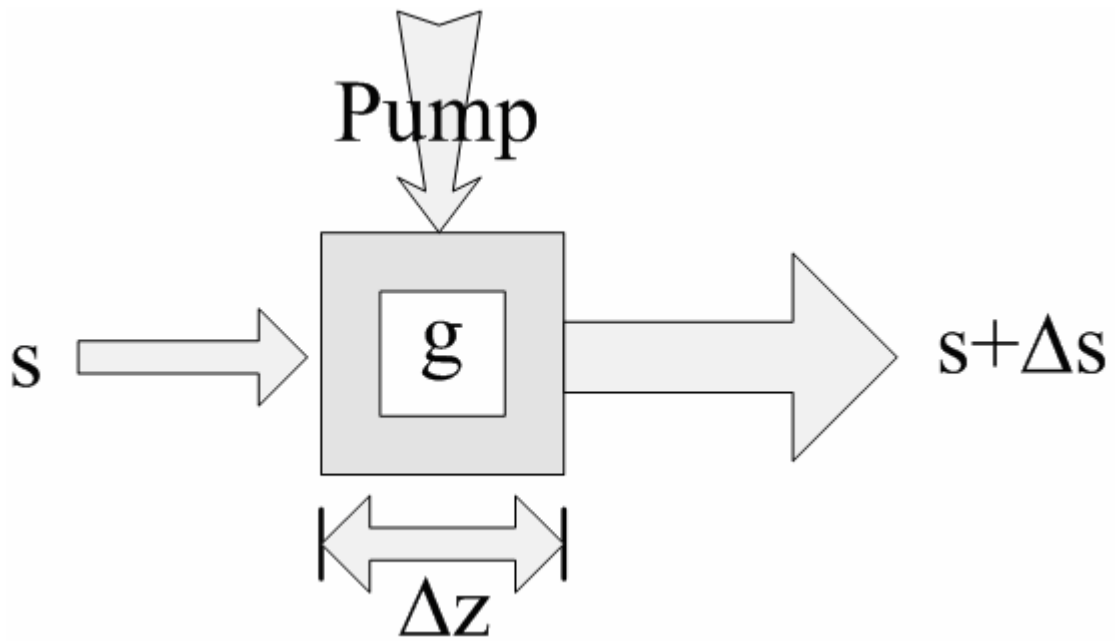


Fig. 2.7 Definition of gain in terms of the increase in photon number across a small segment of gain material.

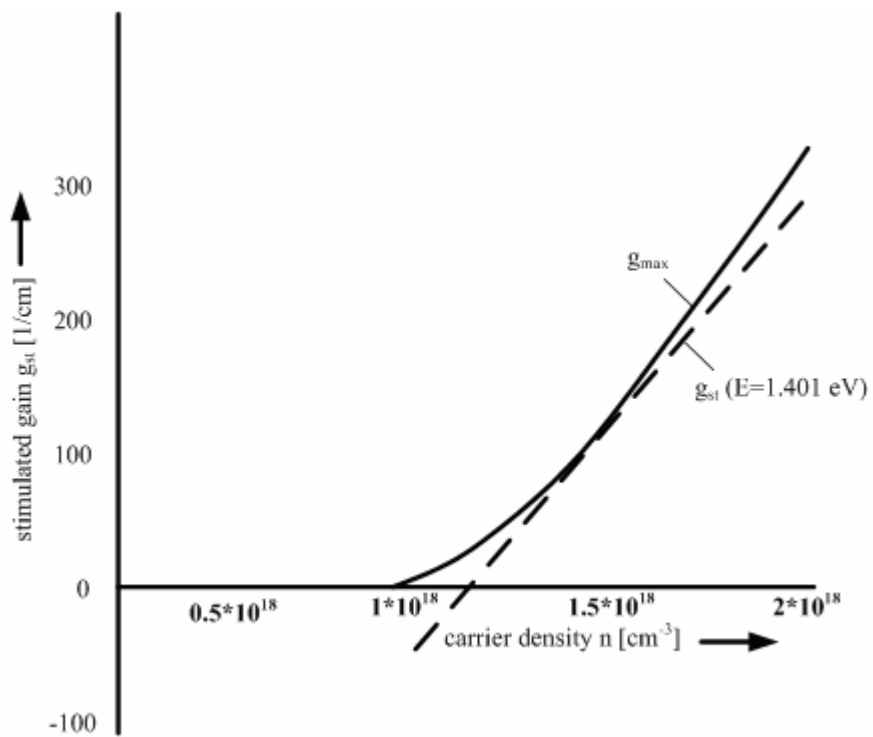


Fig. 2.8 Maximum gain  $g_{max}$  and gain at a specific photon energy.

[K. Petermann, Laser Diode Modulation and Noise, 1991]

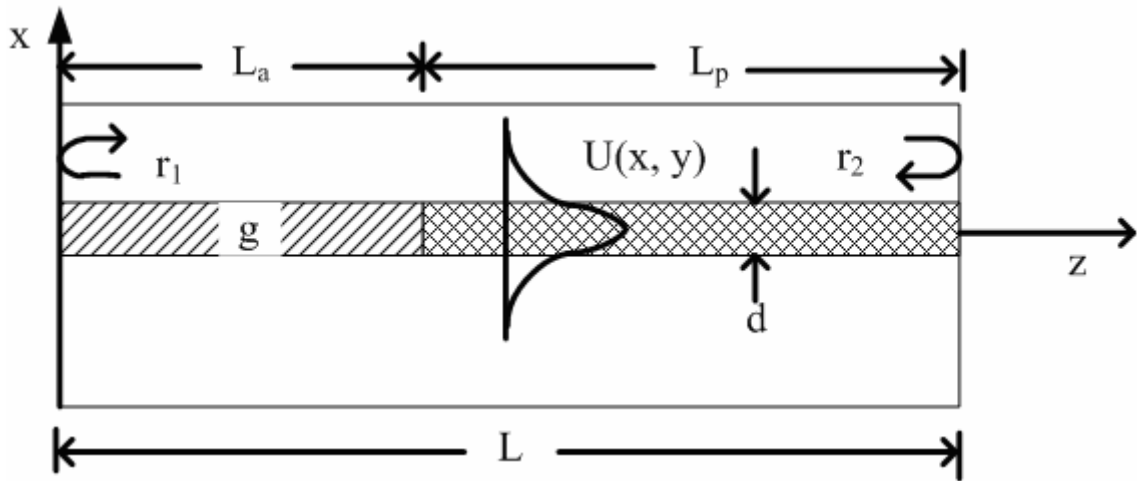


Fig. 2.9 Generic laser cavity cross section showing active and passive sections and the guided-mode profile.

[L. A. Coldren, and S. W. Corzine, *Diode Lasers and Photonic Integrated Circuits*, New York: Wiley Interscience, 1995.]

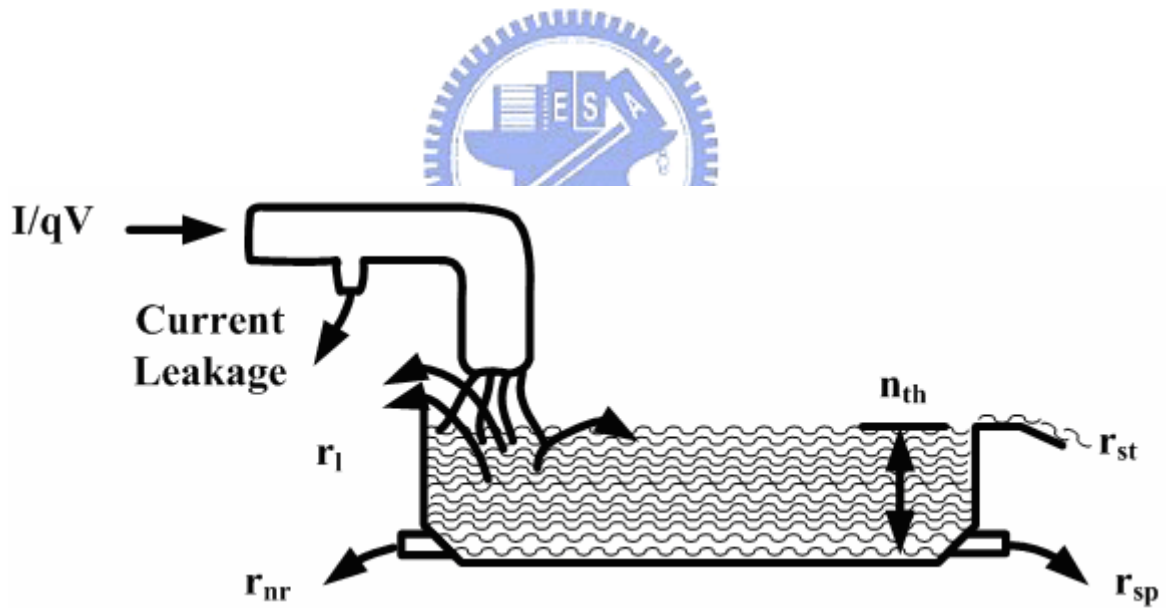


Fig. 2.10 Reservoir analogy above threshold where water level has risen to the spillway so that an increased input results in an increased output ( $R_{st}$ ) but no increase in carrier density (water level). The flows  $R_{nr}$  and  $R_{sp}$  do not change above threshold.

[L. A. Coldren, and S. W. Corzine, *Diode Lasers and Photonic Integrated Circuits*, New York: Wiley Interscience, 1995.]

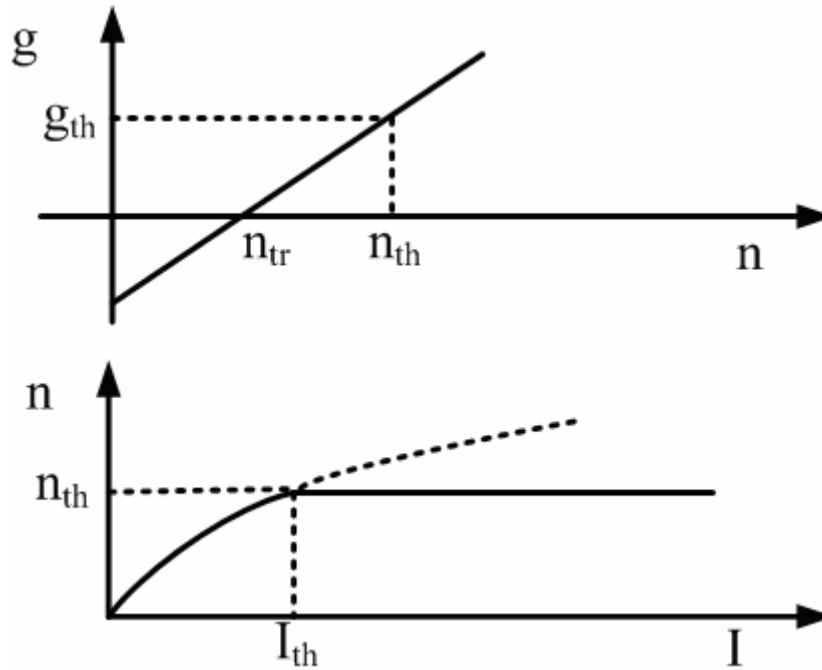


Fig. 2.11 Gain vs. carrier density and carrier density vs. input current. The carrier density clamps at threshold causing the gain to clamp also.

[L. A. Coldren, and S. W. Corzine, *Diode Lasers and Photonic Integrated Circuits*, New York: Wiley Interscience, 1995.]

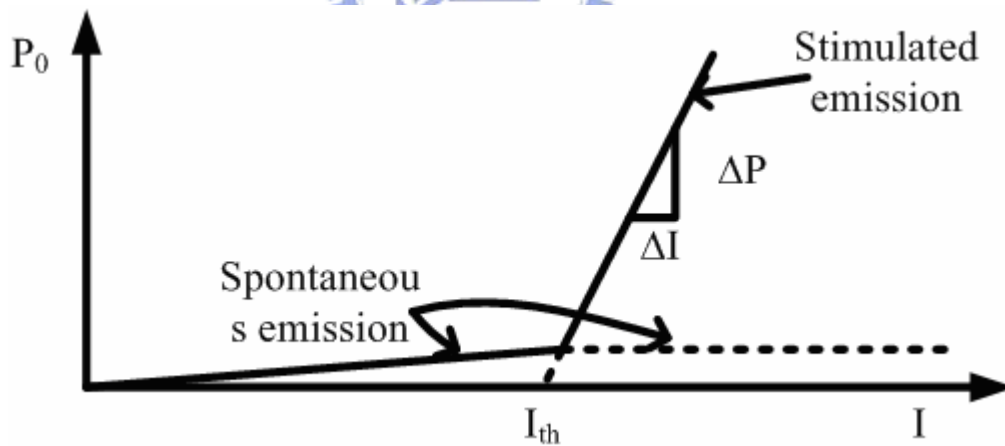


Fig. 2.12 Illustration of output power vs. current for a diode laser. Below threshold only spontaneous emission is important; above threshold the stimulated emission power increases while the spontaneous emission is clamped at its threshold value.

[L. A. Coldren, and S. W. Corzine, *Diode Lasers and Photonic Integrated Circuits*, New York: Wiley Interscience, 1995.]

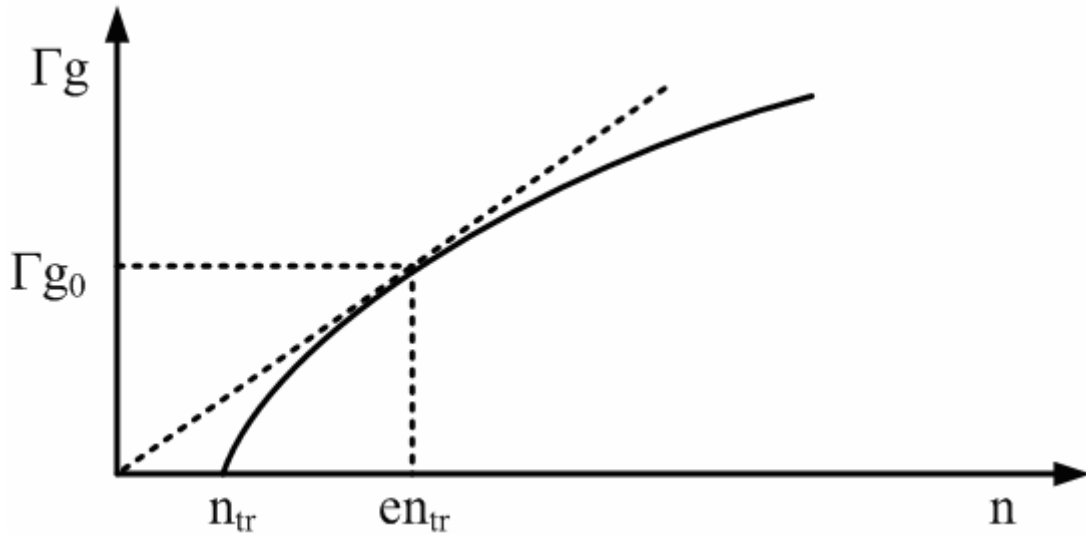


Fig. 2.13 Schematic illustration of modal gain versus injected carrier density with values labeled from the two-parameter logarithmic fit of Eq. (2.41).

[L. A. Coldren, and S. W. Corzine, *Diode Lasers and Photonic Integrated Circuits*, New York: Wiley Interscience, 1995.]

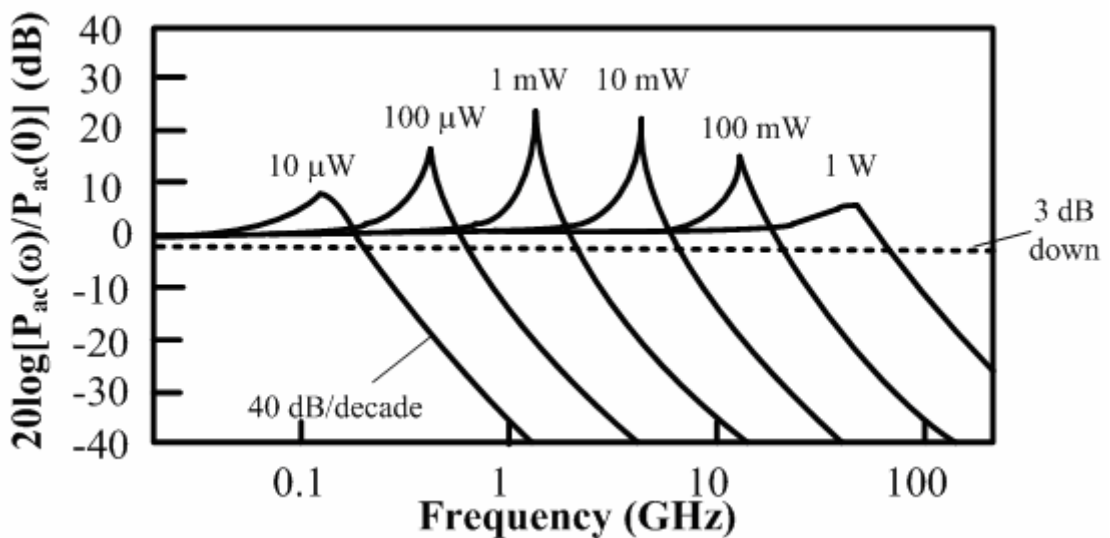


Fig. 2.14 Frequency response of an idealized diode laser for several different output powers.

[L. A. Coldren, and S. W. Corzine, *Diode Lasers and Photonic Integrated Circuits*, New York: Wiley Interscience, 1995.]

# Chapter 3

## All-optical NRZ-to-RZ Data Format Converter with An Injection-locked Fabry-Perot Laser Diode in Unlasing Condition

### Abstract

By using an optical nonreturn-to-zero (NRZ) formatted data stream to injection-lock a synchronously modulated Fabry-Perot laser diode at below threshold condition, an output data stream with return-to-zero (RZ) formatted can be generated at bit rates of up to 9.953 Gbit/s. Such an NRZ-to-RZ data format conversion is due to the injection-locking-induced gain-switching of the FPLD with the incoming NRZ data. The RZ data stream with a maximum on/off extinction ratio of 12.2 dB is obtained under the optical injecting power of -2 dBm and the RF driving power of 24.4 dBm. The best side-mode suppression ratio of 40 dB and the lowest timing jitter of 0.4 ps for the RZ pulse are observed. Power penalties of 1.2 and 1.5 dB are measured at a bit-error rate of  $10^{-9}$  after NRZ-to-RZ conversion for bit rate of 2.488 and 9.953 Gbit/s, respectively.

### 3.1 Introduction

In this chapter we will propose an FPLD-based NRZ-to-RZ data format converter. The FPLD used in this experiment is synchronously modulated by an RF current in unlasing condition. That is, the maximum RF current is at or just below threshold current and the FPLD can not be gain-switched. Furthermore, the threshold current of FPLDs will be

reduced under external light injection, as mentioned in Chapter 2. Thus, the synchronously-modulated FPLD just below threshold current will become gain-switching when its threshold current is reduced by an external injection locking.

In Section 3.2, we introduce the operating principle of an FPLD-based all-optical NRZ-to-RZ data format converter. In Section 3.3, experimental setups and results of threshold current reduction under external injection locking, injection-locking-induced gain switching, FPLD-based all-optical NRZ-to-RZ data format converter are presented.

## **3.2 Operating Principle of Injection-locking-induced gain-switching in a Synchronously-modulated FPLD just below Threshold Current**

As mentioned in Chapter 1, gain switching has the advantage that no external cavity and no sophisticated fabrication technology are required. The idea of gain switching originated from the observations of relaxation oscillations when turning on a diode laser from below threshold using sinusoidal waves or electrical pulses with a fast leading edge. When a diode laser is gain-switched, the generated optical pulsewidth is considerably shorter than the electrical pulse. Gain-switching consists of exciting the first spike of relaxation oscillation and terminating the electrical pulsewidth before the onset of the next spike. In other words, the electrical pulsewidth should be rather short and should lie in the picosecond or nanosecond time range. The most popular electrical driving sources for gain switching are comb generators [85, 86], picosecond photoconductive switches [87, 88], and avalanche transistor generators [89]. Alternatively, the modulation of a laser biased below threshold with a large sinusoidal signal at subgigahertz or gigahertz frequency also results in gain-switched optical pulses [90, 91].



The generation of ultrashort light pulses by a gain-switched diode laser is illustrated in Figs. 3.1 and 3.2(a). The DC bias and a sinusoidal current are assumed to be applied on the laser, as shown in Fig. 3.1(a).  $I_0$  can be below or above the threshold. Below the threshold lasing does not occur until the electric pulse increases the injection carrier density above the threshold carrier density, as shown in Fig. 3.1(b). Then lasing occurs and represses the increase in carrier density. Thus, an optical pulse is generated.

From the derivations in Chapter 2, the threshold current of the diode laser can be reduced under external injection locking. When the FPLD is modulated by a large sinusoidal signal at just below threshold [see case (A) in Fig. 3.2(b)], it is in unlasing condition. However, the FPLD will be gain-switched when an external CW light injection-locks the FPLD [see case (B) in Fig. 3.2(b)]. That is, under the external injection locking, the FPLD will be translated from an unlasing to a gain-switching operation.

### 3.3 Experimental Setup and Results

The FPLD used in the experiment is a pig-tailed one with a threshold current of 13 mA and a longitudinal mode spacing of 1.2 nm. It is biased by a laser diode controller (ILX 3724) and modulated by the RF sinusoidal-wave synthesizer (Agilent E8257C) via a Bias Tee circuit (Hewlett Packard 33150A). The output power is measured by a power meter (ILX OMM-6810B). The temperature of the FPLD is controlled at 27.5°C with fluctuation of <0.1 °C to prevent the wavelength drift of the FPLD's longitudinal modes.

#### 3.3.1 Threshold Current Reduction under External Injection Locking

To measure the reduction of the threshold current under external injection locking, an experimental setup is constructed, as shown in Fig. 3.3. The FPLD is externally

injection-locked by a tunable laser (TL; Hewlett Packard 8168F) through an optical circulator. The power-current relationships with and without external light injection are measured by a computer-controlled program. It is noted that the wavelength of the external injected light is aligned with the long wavelength part of the central longitudinal mode at just above threshold current to achieve stable injection locking of the FPLD. Figure 3.4 shows the measured light-current (L-I) curves with and without external injection locking. The injection power in the experiment is -2 dBm. We can find that the threshold current is reduced from 13 to 10 mA under external injection locking.

### **3.3.2 Injection-locking-induced Gain Switching**

To investigate the gain-switching of the FPLD via external optical injection locking, the experimental setup is constructed, as shown in Fig. 3.5. An RF amplifier (MiniCircuits ZHL-2-12) is used to amplify the sinusoidal wave to periodically bias the FPLD. A polarization controller (PC) is placed before the optical circular for optimizing the polarization of the injected light. An erbium-doped fiber amplifier after the optical circulator is used to amplify the gain-switching pulse for enhancement of the extinction ratio.

The FPLD is modulated only by an amplified RF signal of 24.4 dBm below the threshold current. Without external light injection into the FPLD, no optical pulses can be observed on the digital sampling oscilloscope (DSO, Agilent 86100A with 86106A). The RF operating frequency is set at 1 GHz for the experiment of a CW external injection locking. With an injection power of -2 dBm and a wavelength coincident with that of the FPLD's longitudinal mode, the effective threshold current of the FPLD will be reduced by the external TL injection. Thus, the injection of the TL will cause the FPLD to enter gain-switching operation.

The pulsewidth and the peak power of the FPLD's output after EDFA are 44 ps and up to 135 mW (corresponding to average power of 5.94 mW), as shown in Fig. 3.6. It is noted

that an attenuator is used to prevent the damage of the sampling head of the DSO. Furthermore, the wavelength of the TL is detuned away from one longitudinal mode (Fig. 3.7a) to the other (Fig. 3.7c) for evaluations of the maximum wavelength detuning range capable of reducing the threshold current. We can find that the FPLD will not be injection-locked when the wavelength of the external injection light is detuned away from the locking range (e.g., Fig. 3.7b). As shown in Fig. 3.8, the temporal traces versus the detuning range shows that the gain-switching pulses will be degraded and diminished when the wavelength detuning range is larger than 0.2 nm.

As the wavelength of the injected light completely coincides with that of one of the FPLD's longitudinal modes, the maximum side mode suppression ratio (SMSR) of 34 dB can be obtained, which is better than the FPLD operated at wavelength mismatching condition, as shown in Fig. 3.7. Therefore, the wavelength matching between the external injection laser and the longitudinal mode of FPLD is mandatory for generating gain-switched pulses with largest peak power and highest SMSR.

Under the precise control of the external injection wavelength, the extinction ratio (ER) of the injection-locking-induced pulse-train (defined as the amplitude ratio of the pulse with and without injection locking) is measured. By switching the external injection wavelength between  $\lambda$  and  $\lambda + 0.6$  nm, the maximum ER of the FPLD pulse-train is about 10.5 dB (see Fig. 3.9). Similarly, the ER of FPLD pulse-train can be also defined as the amplitude ratio of pulses with to without external injection. The ER of the injection-locked FPLD pulse-train is up to 12.2 dB under the on/off control of external injection, as shown in Fig. 3.9. The amplified spontaneous emission (ASE) of the FPLD is slightly higher without the injection of the TL, as shown in Fig. 3.10. This indicates that the suppression of the ASE and side modes of the FPLD under external injection from the TL is more pronounced than those of the FPLD at normal operation. This is mainly attributed to the reduction of effective threshold current of the FPLD under the external injection case. In addition, a relatively weak signal

with considerable noise has also been found as the injection wavelength is detuned away from the FPLD's longitudinal mode by 0.4 nm.

The lasing spectra of the CW free-running FPLD, the CW tunable laser, and the gain-switched FPLD are measured by using an optical spectrum analyzer, as shown in Fig. 3.11. The measured 3-dB spectral linewidth for one longitudinal mode of the CW free-running FPLD are 0.1 nm. When the FPLD is gain-switching without external injection locking, the 3-dB linewidth significantly broaden to 0.36 nm. This result correlates well with the theory that the transient variation in carrier density simultaneously affects the refractive index and mode linewidth of the gain-switched FPLD [125]. However, under injection locking the linewidth is reduced to 0.146 nm.

Moreover, the variation in RF driving power and external injection power can strongly affect the ER of the gain-switched FPLD operated in injection-locking condition (see Fig. 3.12). When RF driving power is below the threshold value (24.4 dBm), the ER is extremely small [see trace (b) in Fig. 3.12]. It is found that the tolerance on RF driving power for optimized ER of FPLD pulse-train is relatively severe. Only 1 dB increasing of RF power will cause a serious degradation on the ER of FPLD pulse-train due to the self-gain-switching of the FPLD. The optimized RF driving power is ranged from 24.4 to 24.7 dBm. In particular, when RF driving power is set at just below threshold, there is a trade-off between the ER of FPLD pulse-train and the external injection power. External injection power larger than -2 dBm contributes more power to the CW component of FPLD and thus degrades the ER.

The peak power and SMSR of the single-mode gain-switched FPLD at different injection powers are shown in Fig. 3.13. The best SMSR of 40 dB under injection power of 6 dBm is obtained at a cost of slightly decreasing peak power (~140 mW). At wavelength-matched condition, the lowest noise performance is obtained from the injection-locked FPLD. The single-side-band (SSB) phase noise spectrum and the associated timing jitter of the

injection-locking-induced pulses are also evaluated. With external injection power of 6 dBm, the injection-locking-induced pulses exhibit SSB phase noise as low as -100 dBc/Hz at 5 kHz offset from carrier frequency, as shown in Fig. 3.14. The corresponding rms timing jitter of 0.4 ps calculated over an integral frequency band between 10 Hz and 5 kHz is also shown in Fig. 3.14.

Furthermore, the rms timing jitter of the injection-locking-induced pulse as a function of the external injection power is also depicted in Fig. 3.15. The timing jitter of the injection-locking-induced pulse decreases from 0.7 ps to 0.4 ps as the external injection power increases from -14 dBm to 6 dBm. In principle, the rms timing jitter is proportional to the ratio of the standard deviation to the mean value of the cavity photon density around time  $t_0$ , where  $t_0$  is the time corresponding to the threshold carrier density reaches the threshold. On condition that the injection power is smaller, the timing jitter is dominated by spontaneous emission of the FPLD. As the injection power is increased, the externally injected light provides a stimulated emission which is well above the level of spontaneous emission in the FPLD cavity. The stimulated emission reduces relative fluctuations in the photon density around  $t_0$ , which leads to a significant reduction in rms timing jitter [126]. In addition, the pulsewidth of gain-switched FPLD slightly shortens from 47 ps to 44 ps with the increase of the external injection power.

### **3.3.3 FPLD-based All-optical NRZ-to-RZ Data Format Converter**

From the previous experiment, we know that the external injection will injection-lock the synchronously-modulated FPLD just below threshold current, causing the FPLD to generate a gain-switching pulse train due to the reduction of the threshold current. Furthermore, such a CW light is encoded by an electrical NRZ-formatted pseudorandom bit sequence (PRBS)

through a Mach-Zehnder intensity modulator to form an optical NRZ PRBS. As the FPLD is injection-locked by such an optical NRZ PRBS, an NRZ-to-RZ conversion is carried out.

The experimental setup for NRZ-to-RZ conversion is depicted in Fig. 3.16. To simulate an incoming optical data stream with NRZ format, an amplified PRBS generated from a pattern generator (Hewlett Packard, 70843B) is used to drive the Mach-Zehnder intensity modulator (MZM, JDS Uniphase, OC-192 Modulator), which then encodes the TL in wavelength-matching condition. A transfer function of the MZM with  $V_{\pi}$  of 5 V is shown in Fig. 3.17. The MZM is biased at 7.5 V (nearly at the linear operating region), and is encoded by a PRBS with amplitude of 5 V. This results in a PRBS-encoded optical NRZ signal with largest on/off ER. Ten percent of the EDFA output power is coupled out to monitor the optical spectrum and the pulse waveform via an optical spectrum analyzer (OSA, Ando, AQ6317B) and a digital sampling oscilloscope, respectively. Finally, the BER of the RZ-formatted PRBS is optoelectronically converted by a clock/data receiver (CDR, Agilent, 83493A) and then measured by using an error detector (Hewlett Packard, 70843A). An optical band-pass filter (OBPF) placed after the EDFA is used to eliminate the CW component of the output RZ-formatted PRBS. As shown in Fig. 3.18, a clean RZ data stream can be obtained when it passes through the OBPF. Without the OBPF, the RZ data stream carries a large ASE from the EDFA, giving rise to an increased CW component and a worse quality on communication data. The adding of the OBPF completely eliminates the 1-mW CW component and results in a clean RZ data stream with the optimum eye diagram.

Figure 3.19 shows the electrical NRZ data before the MZM, the optical NRZ data after the MZM, and the FPLD-transformed RZ data at 2.488Gbit/s data rate, respectively. An 8-bit edited optical NRZ pattern is then transformed into a RZ pattern, as shown in Figs. 3.19b and 3.19c. The duty cycle of such a RZ-formatted data has the potential for the time-division multiplexing (TDM) with a passive TDM technique to enhance the bit rate and

increase the network throughput. Figure 3.20 shows the corresponding eye diagrams of the electrical NRZ, the optical NRZ, and the converted RZ data, respectively. Note that the transformed RZ-formatted data has a larger amplitude noise than the optical NRZ data due to a considerable spontaneous noise of the FPLD at the non-injected condition (*i.e.* “0” state). This drawback can be improved further by using two-mode injection locking (TMIL) technique [127], which transfers the unwanted spontaneous noise to another wavelength.

Moreover, the BER measurements of the RZ data are shown in Fig. 3.21. The RZ-formatted data is detected by a lightwave clock/data receiver (Agilent, 83446A), incorporating a high-gain avalanche photodiode (APD), a gain-controlled amplifier, and a clock/data recovery circuit. The received power is measured in the back-to-back (BtB) NRZ data and the BtB transformed into RZ data at 2.488 Gbit/s. By using a  $2^{23}-1$  bit pseudorandom NRZ data, power penalty of 1.2 dB is measured at a BER of  $10^{-9}$  in the NRZ-to-RZ data converter. The power penalty may be attributed to the considerable spontaneous noise at bit 0 and the amplitude fluctuation at bit 1 in an NRZ-to-RZ data converter. And error-free ( $\text{BER} < 10^{-12}$ ) of RZ-formatted output signal can be achieved when the received optical power is larger than -22 dBm. Similarly, the BER of RZ-formatted signal is also affected by the intensity of the external injection power. Figure 3.22 shows that the BER increases with reduction of the injection power. When the external injection power is larger than 3 dBm, the BER of the RZ-formatted output data can be as small as  $10^{-9}$ . The BER of  $10^{-12}$  can be observed with external injection power of 6 dBm.

A higher data rate can be achieved by raising the DC bias current and reducing the RF modulating power of the FPLD (remaining it at unlasng condition), since the modulating bandwidth is proportional to the DC biased current of FPLD. The highest data rate with BER of  $10^{-9}$  achieved at different DC biased currents is shown in Fig. 3.23. No DC bias current is required for the FPLD to achieve a data rate up to 6 Gbit/s. However, the NRZ-to-RZ data rate of 9.953 Gbit/s can only be achieved by increasing the DC bias current

of the FPLD to  $\geq 9$  mA. The maximum data rate is limited by the carrier lifetime and the DC bias of FPLD.

Figure 3.24 shows the electrical NRZ data stream before the MZM, the optical NRZ data stream after MZM, and the converted RZ data stream generated from the injection-locked and gain-switched FPLD at a data rate of 9.953 Gbit/s, respectively. An 8-bit edited NRZ pattern 01110101 (Fig. 3.24a) is sent into the MZM, and the logically inverted optical NRZ pattern 10001010 is obtained at the MZM output port (Fig. 3.24b). The encoded optical data injected into the FPLD for NRZ-to-RZ transformation, resulting in a RZ-formatted data 10001010, as shown in Fig. 3.24(c). The eye diagrams of the electrical NRZ data stream before the MZM, the optical NRZ data stream after MZM, and the transformed RZ data stream generated from the injection-locked FPLD are shown in Fig. 3.25(a), (b), and (c), respectively.

By externally injecting into the FPLD with a  $2^{23}-1$  bit PRBS NRZ data stream at 9.953 Gbit/s, the BER plotted as a function of the receiving optical power for the NRZ-format optical data and the transformed RZ-formatted output data are shown in Fig. 3.26. The result shows that the FPLD-based NRZ-to-RZ data transformer has a power penalty of 1.5 dB at  $10^{-9}$  BER level. An error-free ( $\text{BER} < 10^{-12}$ ) RZ-formatted data stream can be achieved at a receiving optical power as low as -16 dBm.

When external injection power is larger than 2 dBm, the BER of the RZ-formatted data stream can be as small as  $10^{-9}$  (see Fig. 3.27). Even a BER of  $10^{-12}$  can be observed under an external injection power of 4 dBm.

Table 3.1 compares the performances among versatile NRZ-to-RZ techniques. Our proposed system exhibits the better on/off ER of 12.2 dB, the higher SMSR of 40 dB, and the lower BER of  $10^{-12}$  can be achieved. Moreover, the narrowest pulsewidth of 27 ps at data rate of 9.953 Gbit/s can greatly increase the timing tolerance in TDM application. Although



the power penalty of 1.5 dB at data rate of 9.953 Gbit/s in our configuration is less comparable with that proposed using dual-wavelength injection technique (with power penalty of -9.5 dB), such a simple NRZ-to-RZ converter still benefits from the advantages of easier operation and low cost.



**Table 3.1**

Comparison among versatile NRZ-to-RZ techniques

<i>Mechanism</i>	<b>Dual-wavelength Injection (Hong Kong)</b>	<b>Self-phase Modulation (Korea)</b>	<b>Single-mode Injection (Taiwan)</b>
<i>Characteristics</i>			
<b>Power penalty</b>	-9.5 dB	NA	1.2 dB (OC-48) 1.5 dB (OC-192)
<b>Maximum ER</b>	12 dB	10.5 dB	12.2 dB
<b>Maximum SMSR</b>	> 30 dB	NA	40 dB
<b>Data rate</b>	3.3 Gbit/s	10 Gbit/s	10 Gbit/s
<b>Operation of FPLD</b>	CW lasing	CW lasing	Unlasing (with below-threshold RF modulation)
<b>Complexity</b>	High	Low	Midium
<b>Pulsewidth</b>	47 ps	30 ps	44 ps (OC-48) 27 ps (OC-192)
<b>Year</b>	2002	2004	2004

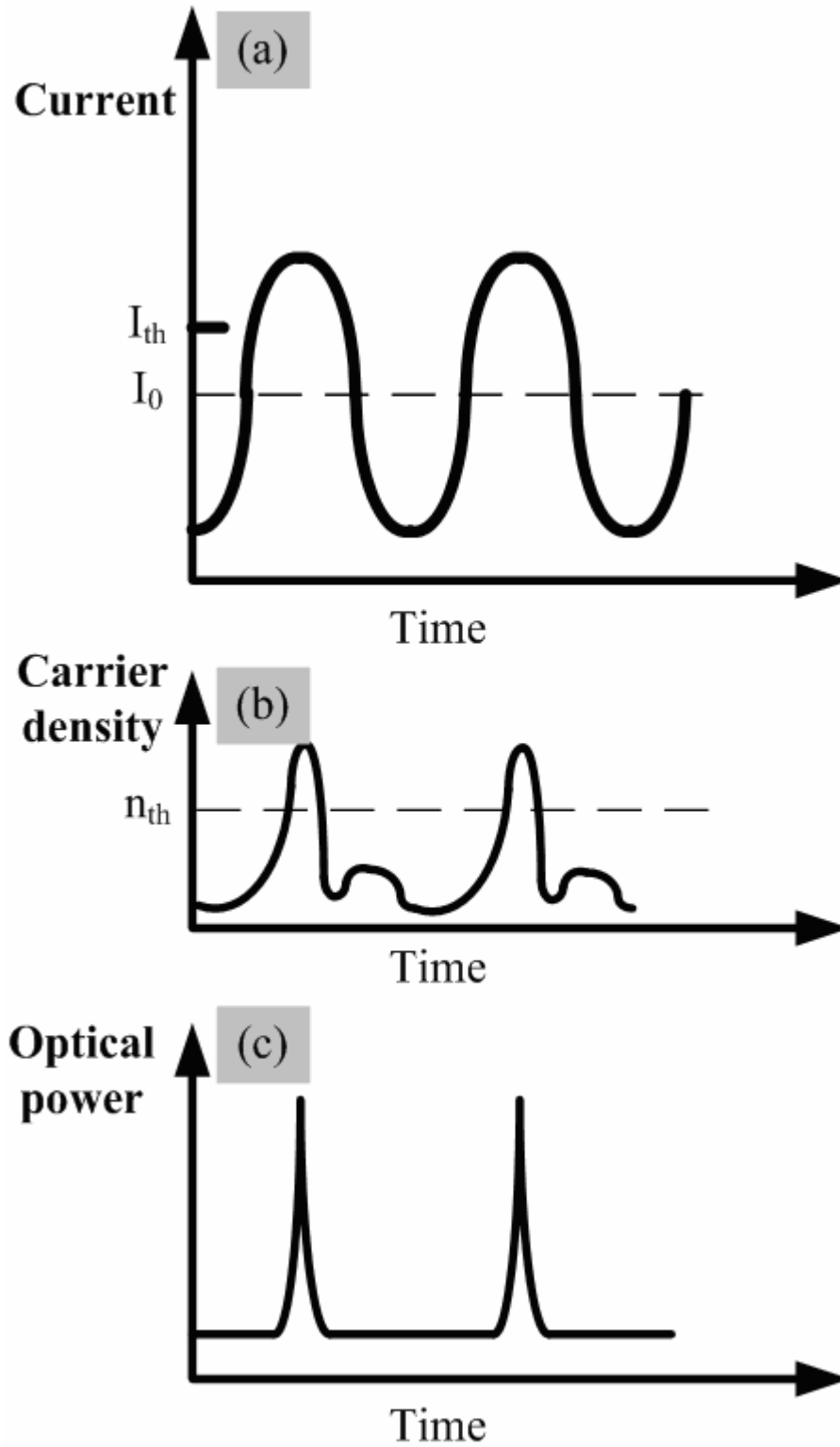


Fig. 3.1 The principle of gain switching. (a) The time dependence of the applied current; (b) The time dependence of the carrier density; (c) The time dependence of output pulses.

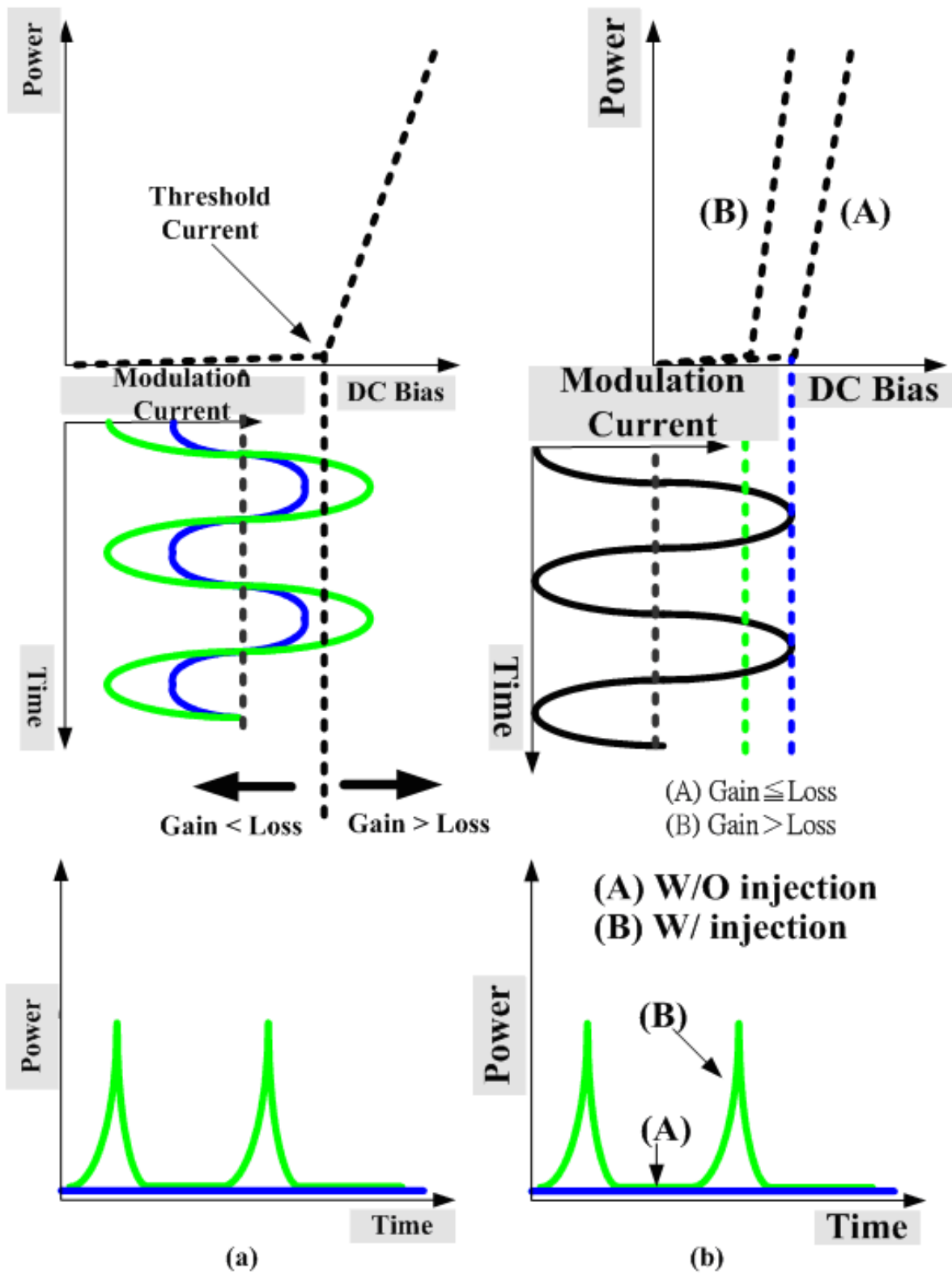


Fig. 3.2 (a) The ‘general’ gain-switching; (b) The injection-locking-induced gain-switching: (A) without external injection; (B) with external injection.

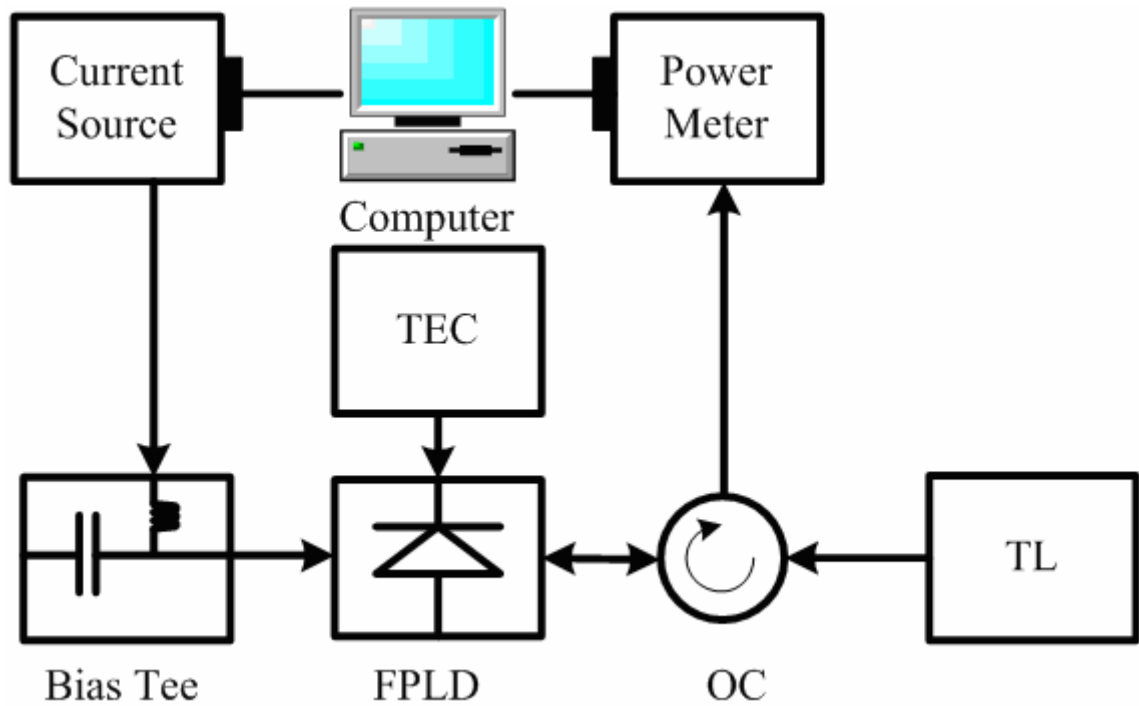


Fig. 3.3 Experimental setup for the observation of the power-current curve with and without external light injection locking. FPLD: Fabry-Perot laser diode; OC: optical circulator; TEC: thermoelectric cooler controller; TL: tunable laser.

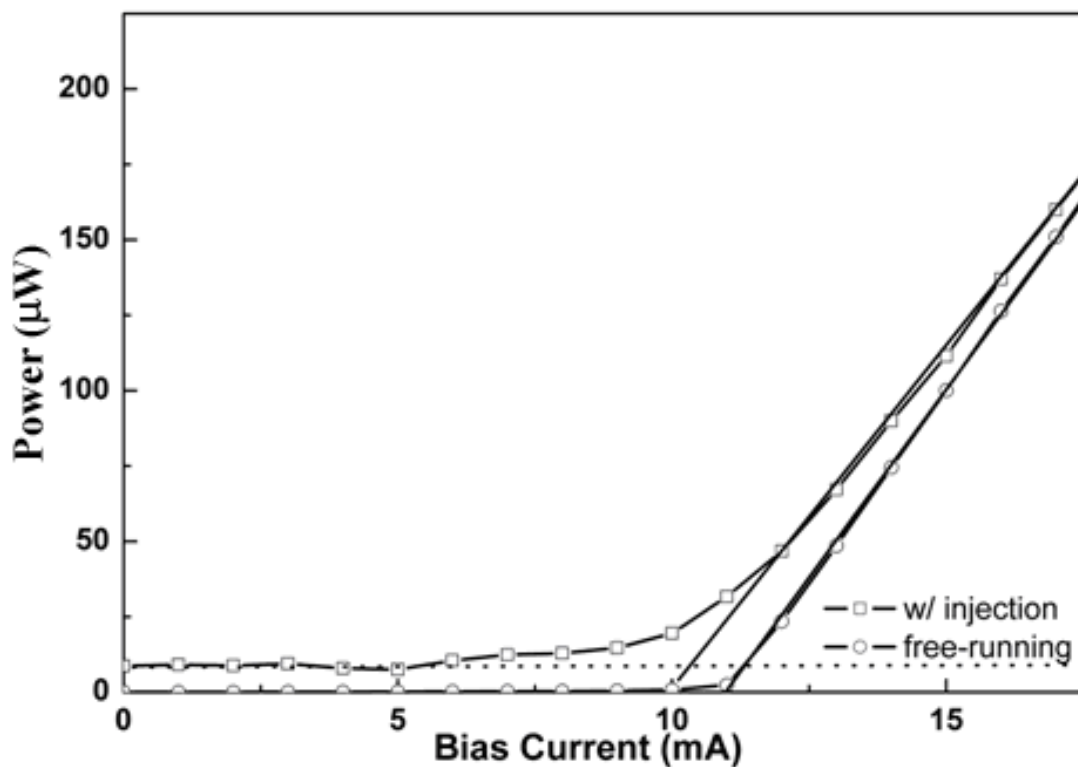


Fig. 3.4 Light-current (L-I) curves with and without external light injection locking.

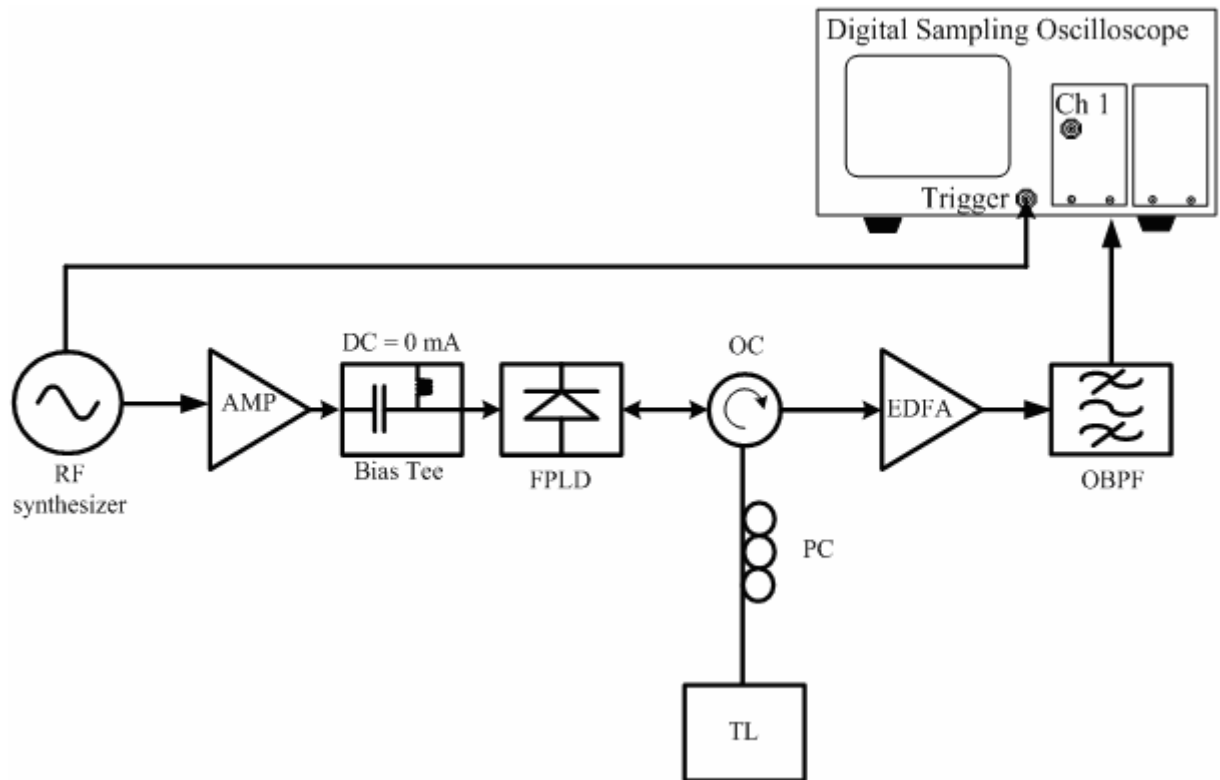


Fig. 3.5 Experimental setup for injection-locking-induced gain-switching. AMP: RF amplifier; EDFA: erbium-doped fiber amplifier; FPLD: Fabry-Perot laser diode; TL: tunable laser; OBPF: optical bandpass filter; OC: optical circulator.

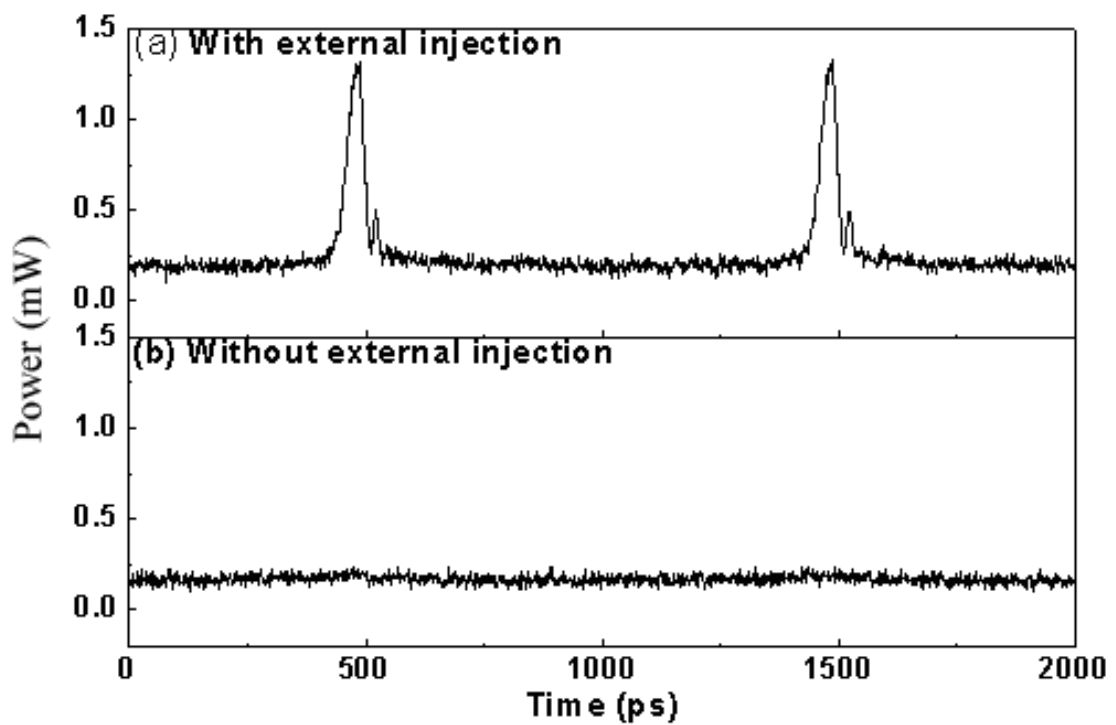


Fig. 3.6 The injection-locking-induced gain switching. (a) with external injection; (b) without external injection.

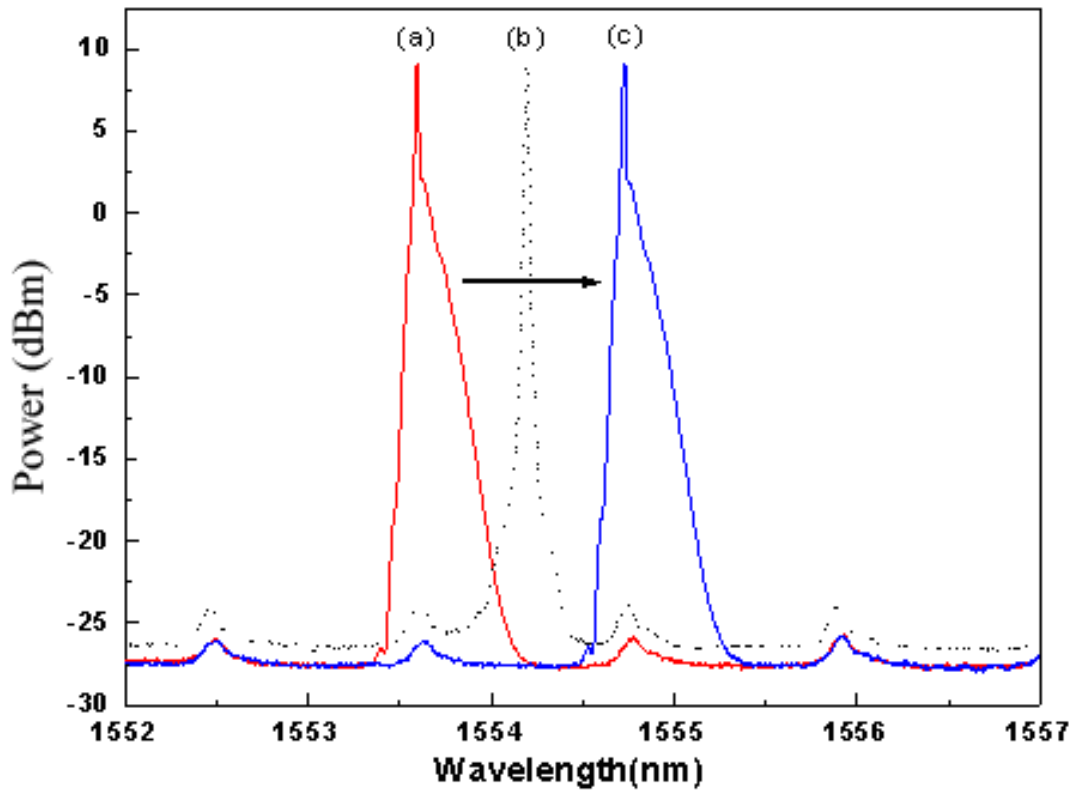


Fig. 3.7 Wavelength detuning of the tunable laser from one longitudinal mode to another.

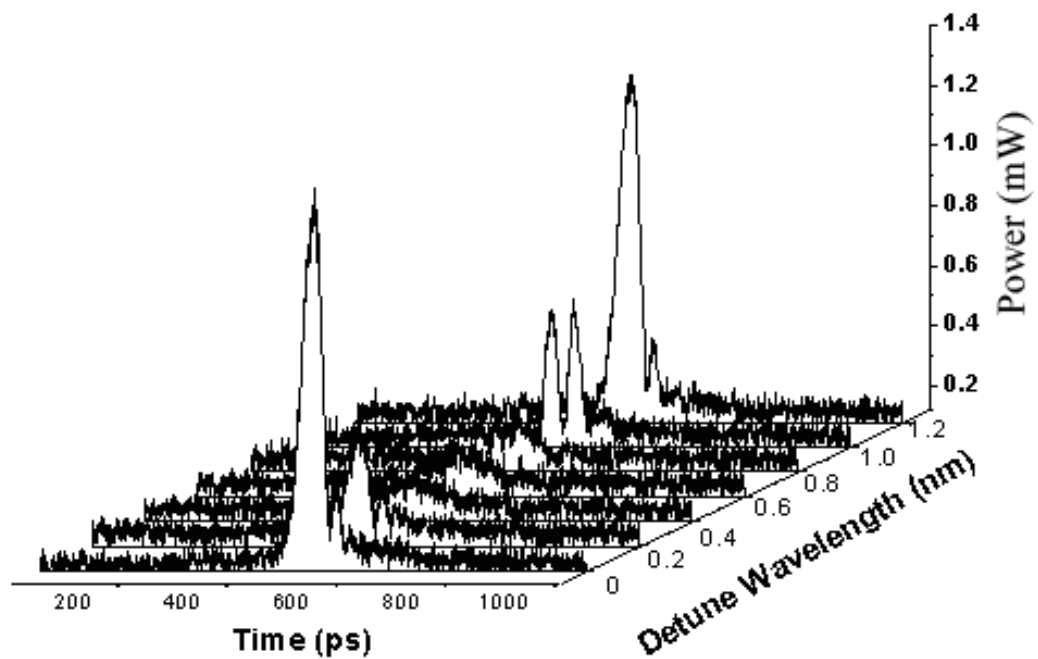


Fig. 3.8 Temporal traces versus the detuning range.

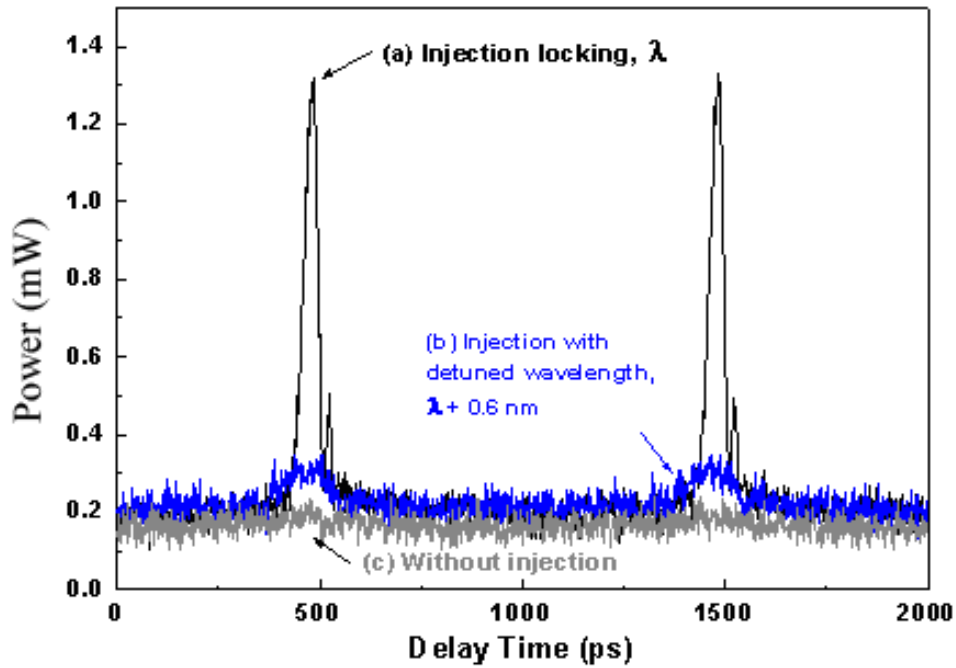


Fig. 3.9 The injection-locking-induced pulse: (a) with injection locking at wavelength  $\lambda$ ; (b) with injection locking at wavelength  $\lambda + 0.6$  nm; (c) without injection. The repetition rate of the pulse train is 1 GHz.

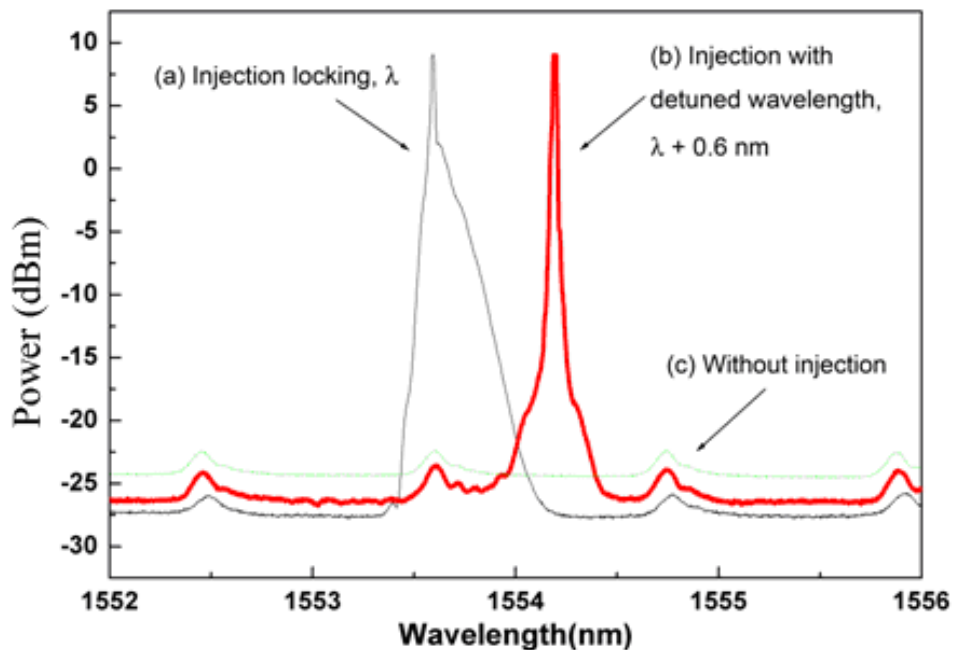


Fig. 3.10 Optical spectra of the FPLD modulated by a large sinusoidal signal at just below threshold: (a) injection locking; (b) injection with detuned wavelength,  $\lambda + 0.6$  nm; (c) without injection. It is noted that the red peak in trace (b) is the signal of the external injection light. The FPLD is not locked in this condition.



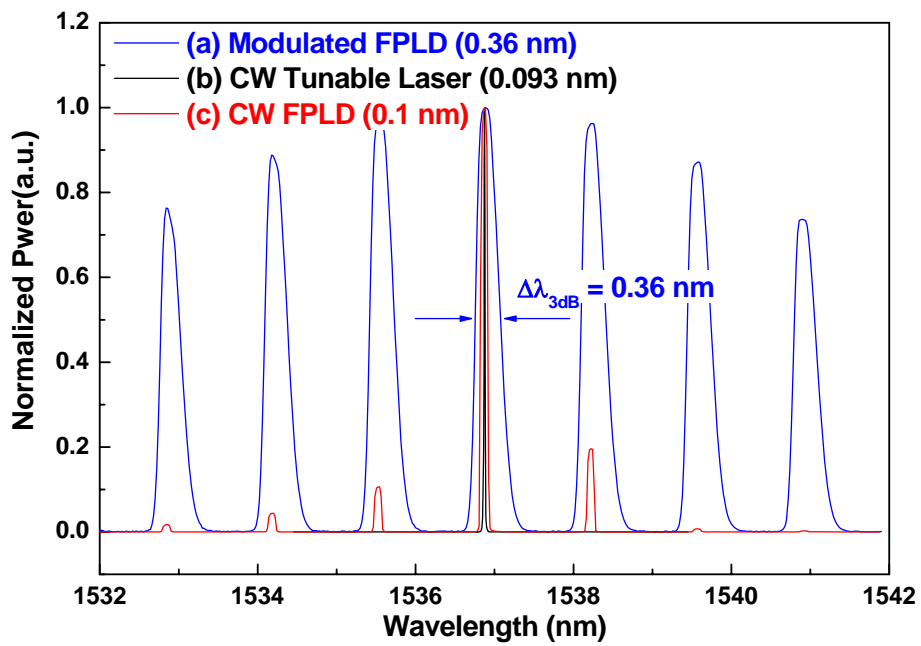


Fig. 3.11 Optical spectra: (a) modulated FPLD; (b) CW tunable laser; (c) CW FPLD injection-locked FPLD.

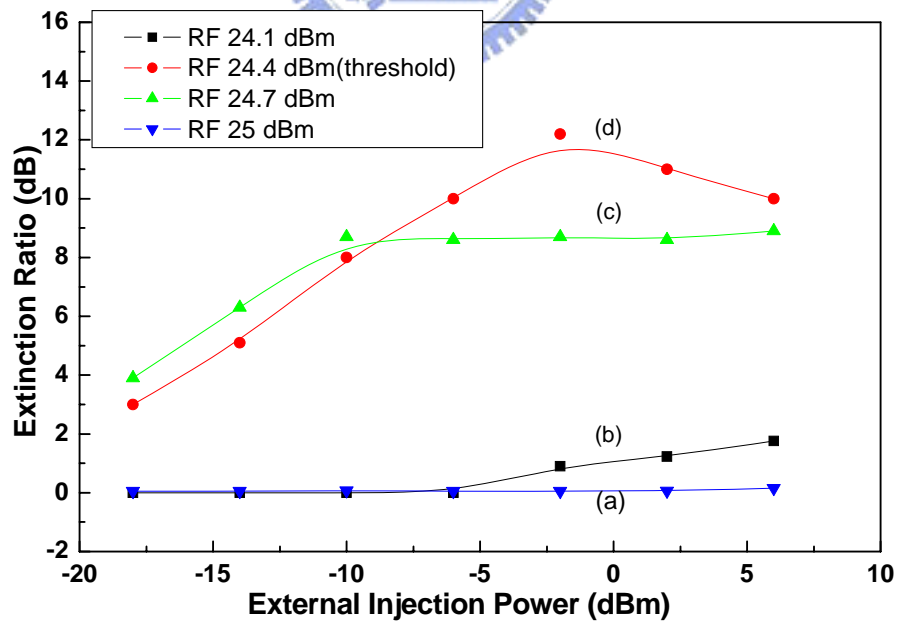


Fig. 3.12 The extinction ratio of the injection-locked FPLD at different RF driving and external injection power.

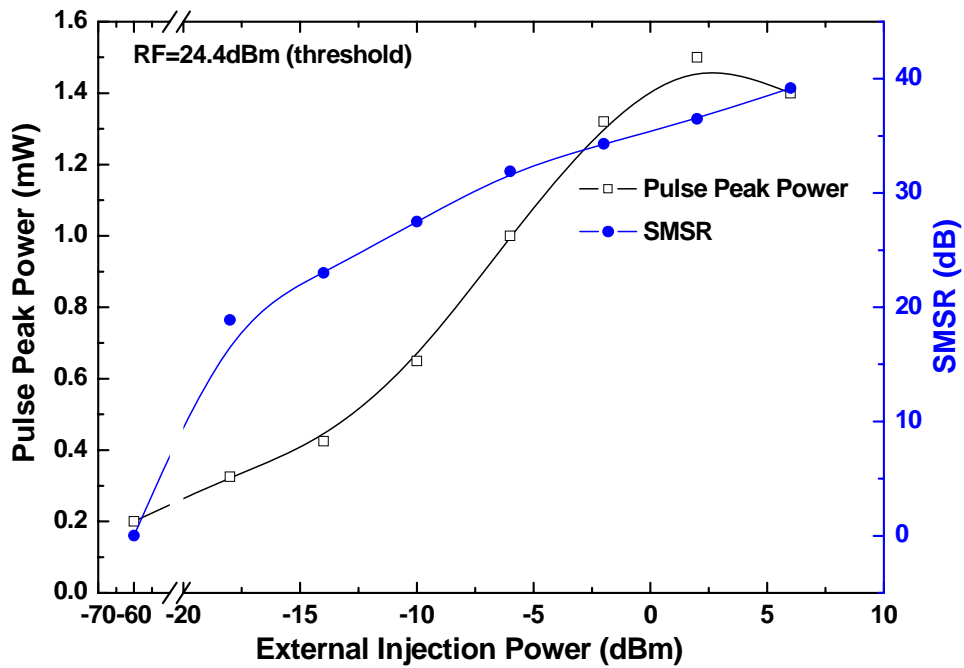


Fig. 3.13 The peak power and the SMSR of the single-mode gain-switched FPLD in injection-locking condition.

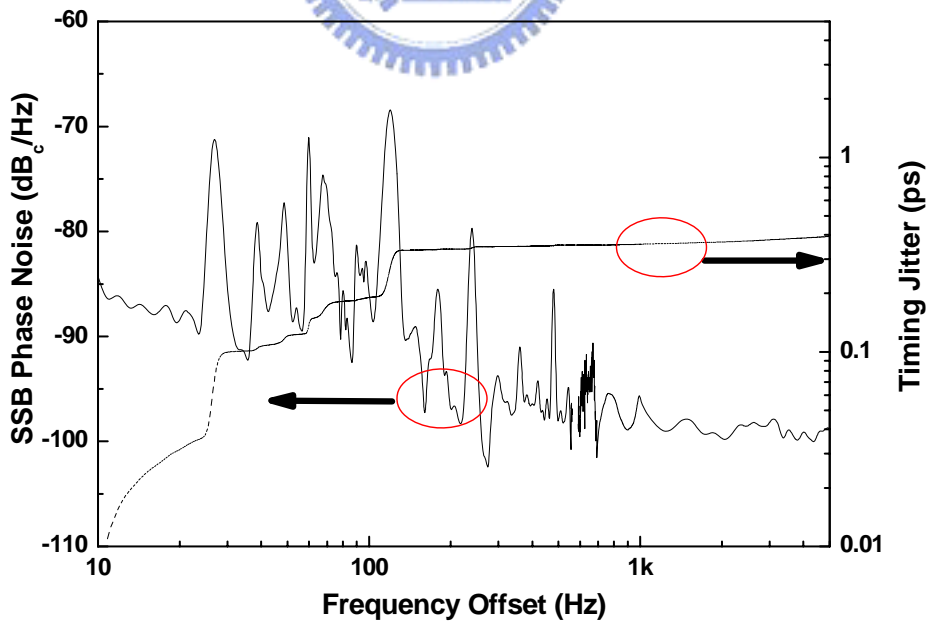


Fig. 3.14 The SSB phase noise density and the associated timing jitter of the injection-locking-induced pulses.

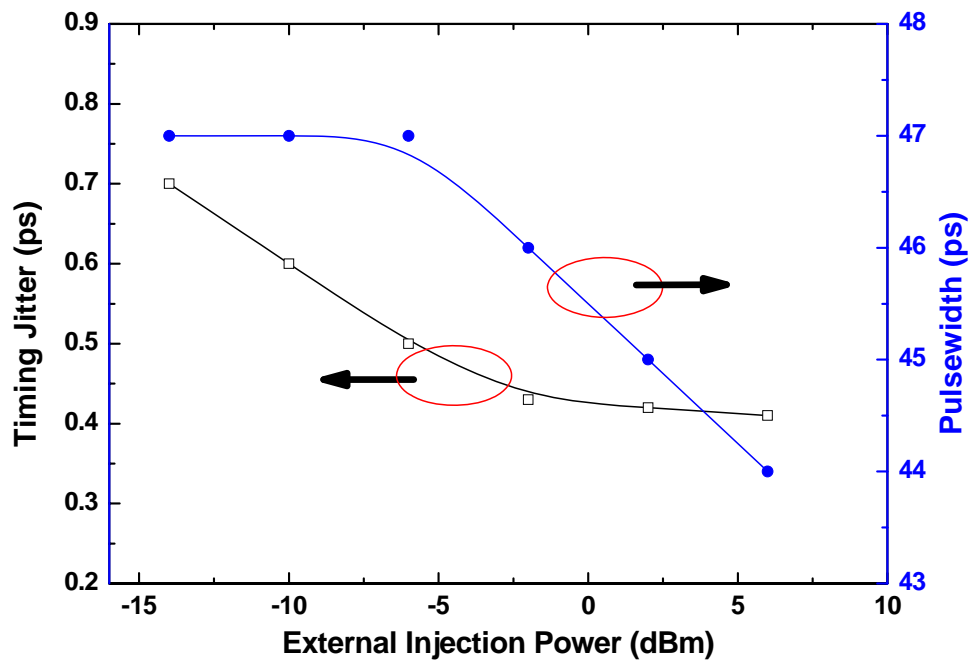


Fig. 3.15 Timing jitter and pulsewidth versus external injection power.

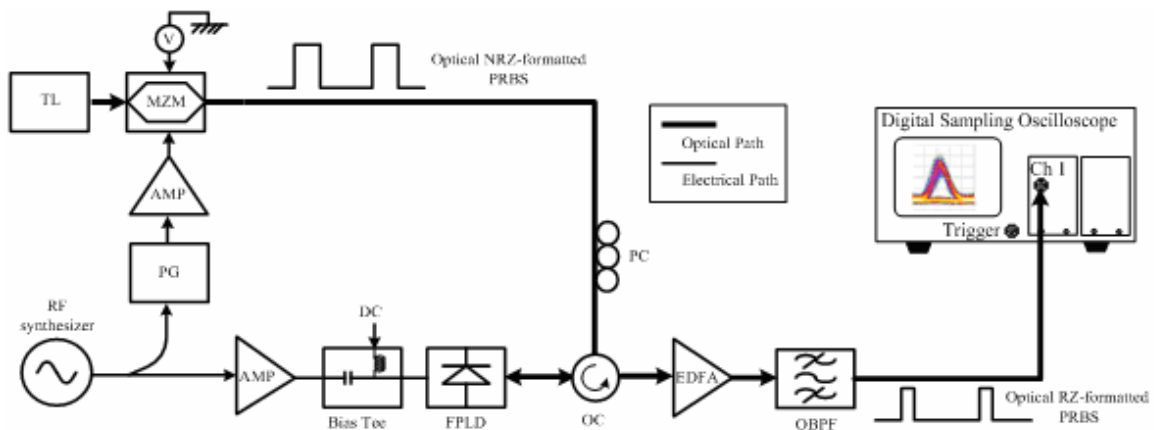


Fig. 3.16 Experimental setup for NRZ-to-RZ data format conversion. AMP: RF amplifier; EDFA: erbium-doped fiber amplifier; FPLD: Fabry-Perot laser diode; MZM: Mach-Zehnder intensity modulator; TL: tunable laser; OBPF: optical bandpass filter; OC: optical circulator; PG: pattern generator.

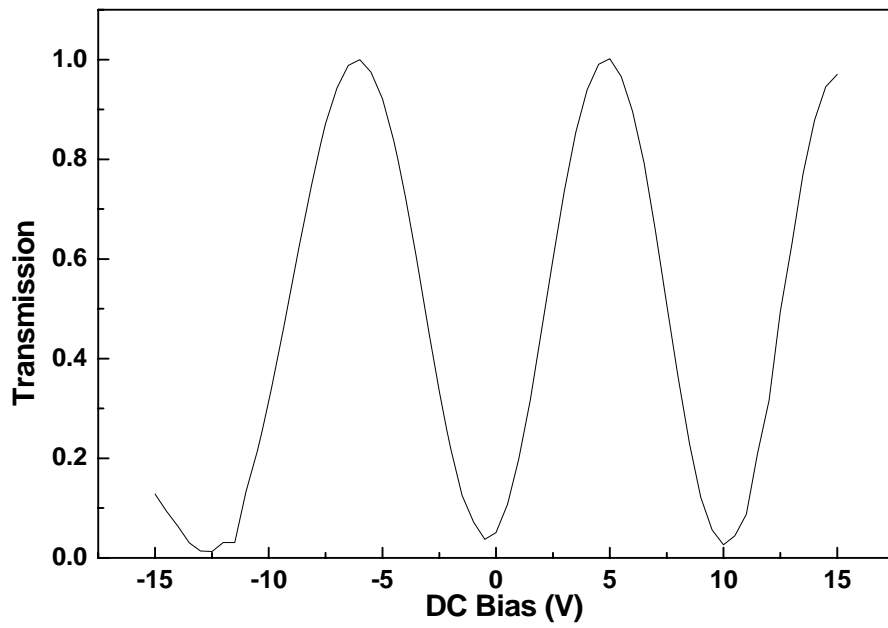


Fig. 3.17 The characteristic transmission coefficient of MZM at different DC bias.

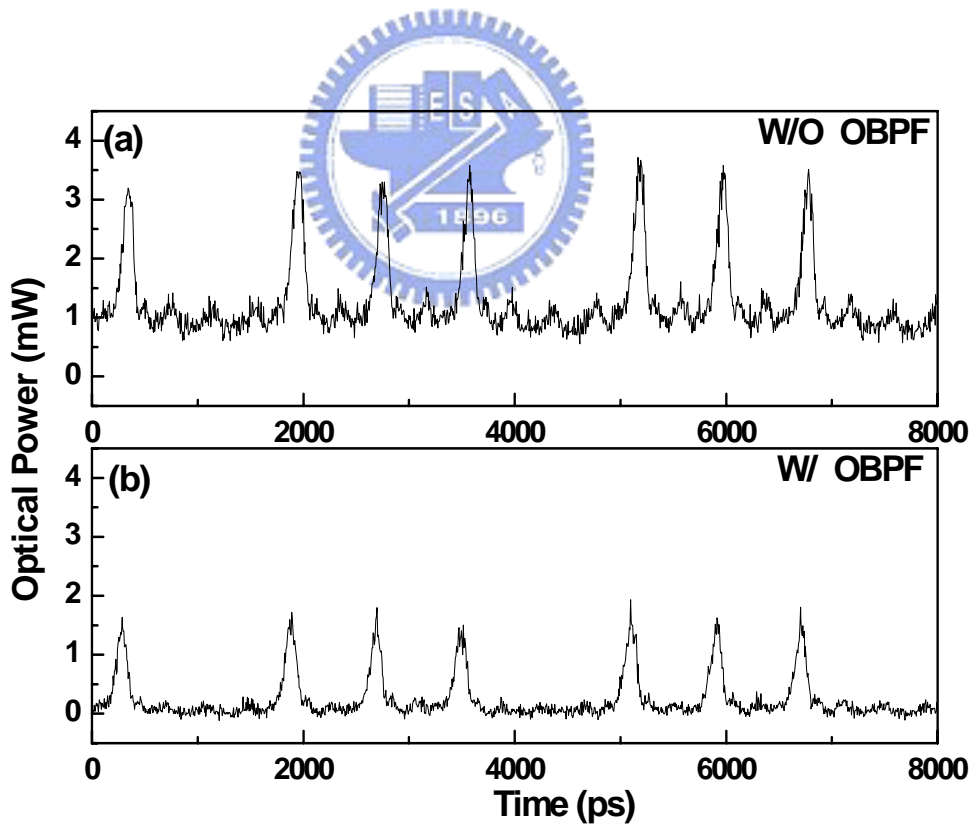


Fig. 3.18 RZ data streams (a) without OBPF (b) with OBPF.

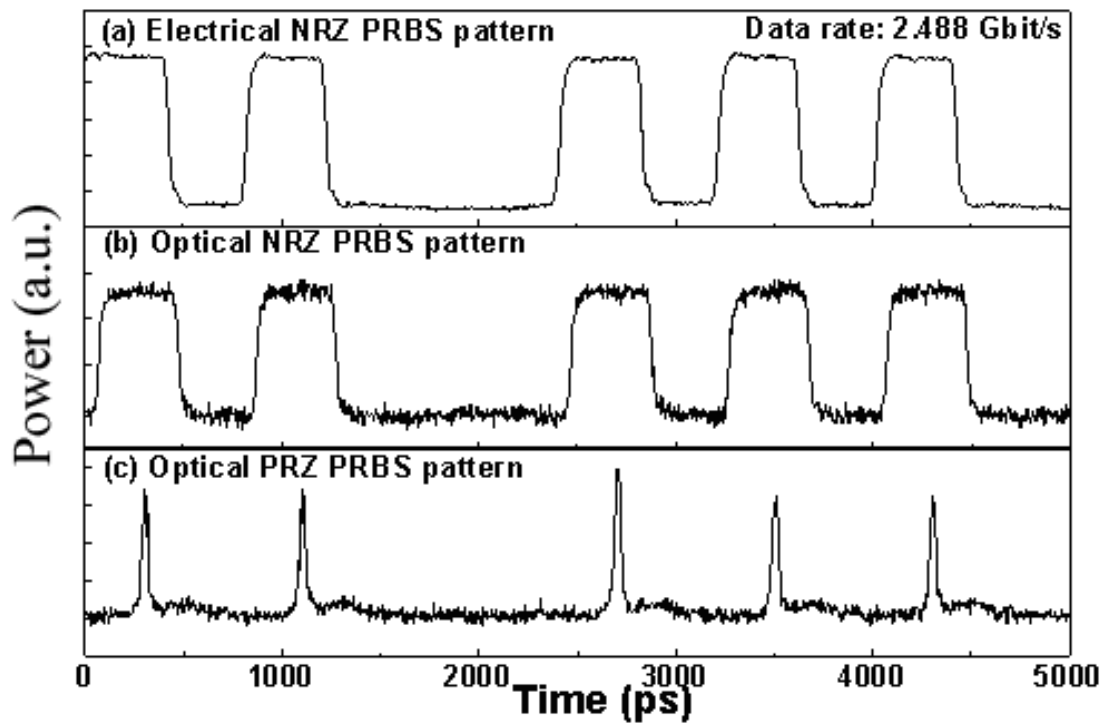


Fig. 3.19 The patterns: (a) the electrical NRZ data before the MZM; (b) the PG-encoded optical NRZ data; (c) the transformed RZ signal generated from the single-mode FPLD. The data rate is 2.488 Gbit/s.



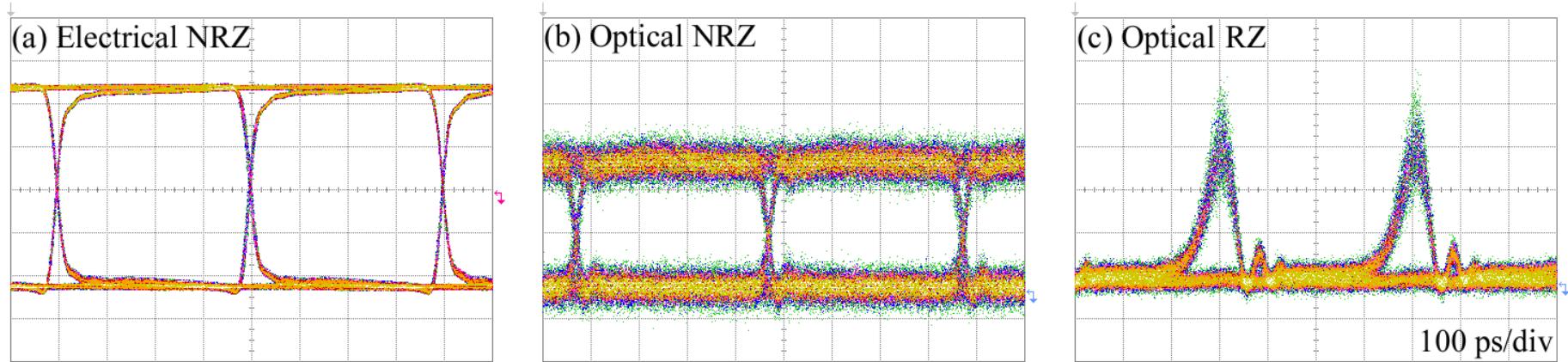


Fig. 3.20 The corresponding eye diagrams: (a) the electrical NRZ data before the MZM; (b) the PG-encoded optical NRZ data; (c) the transformed RZ data. The data rate is 2.488 Gbit/s.

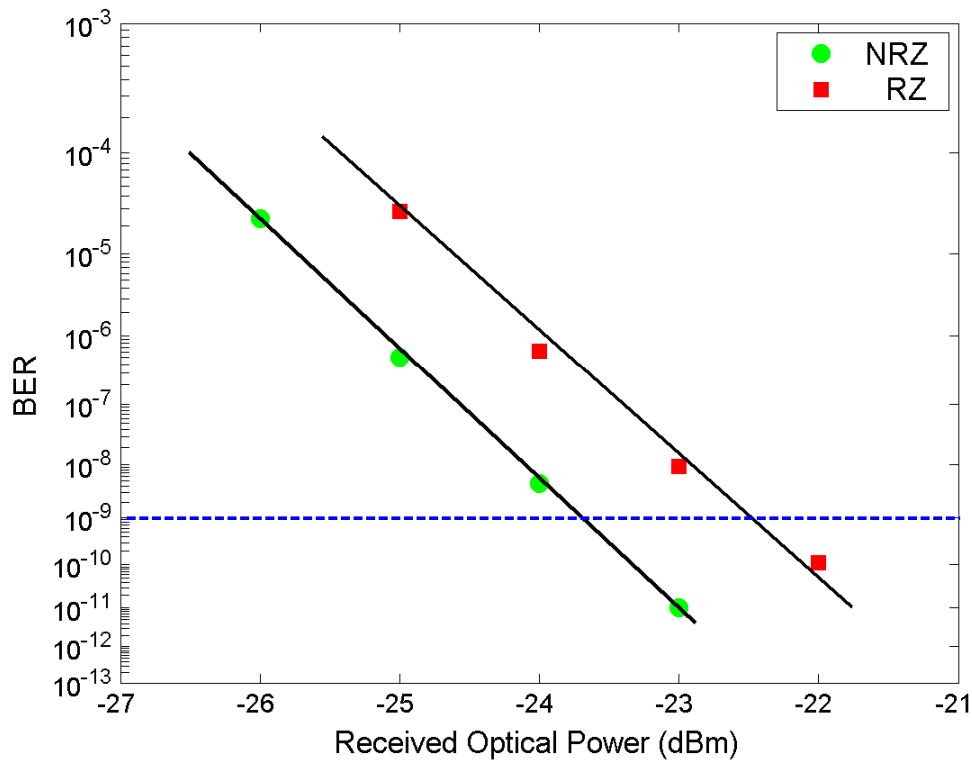


Fig. 3.21 The BER performance at 2.488 Gbit/s.

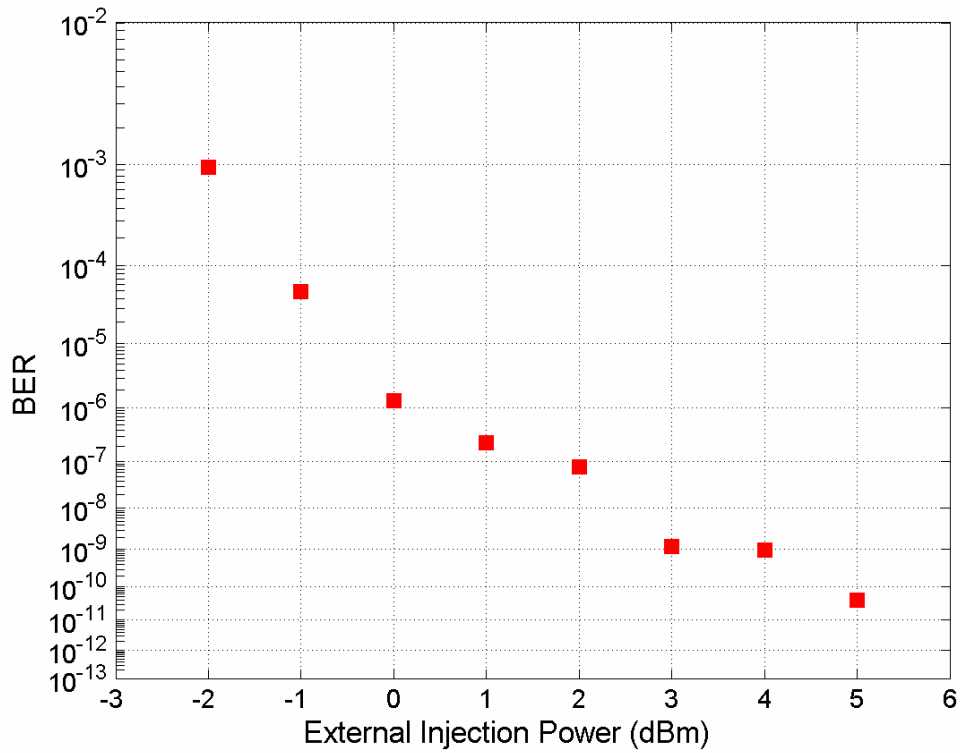


Fig. 3.22 The BER versus the external injection power.

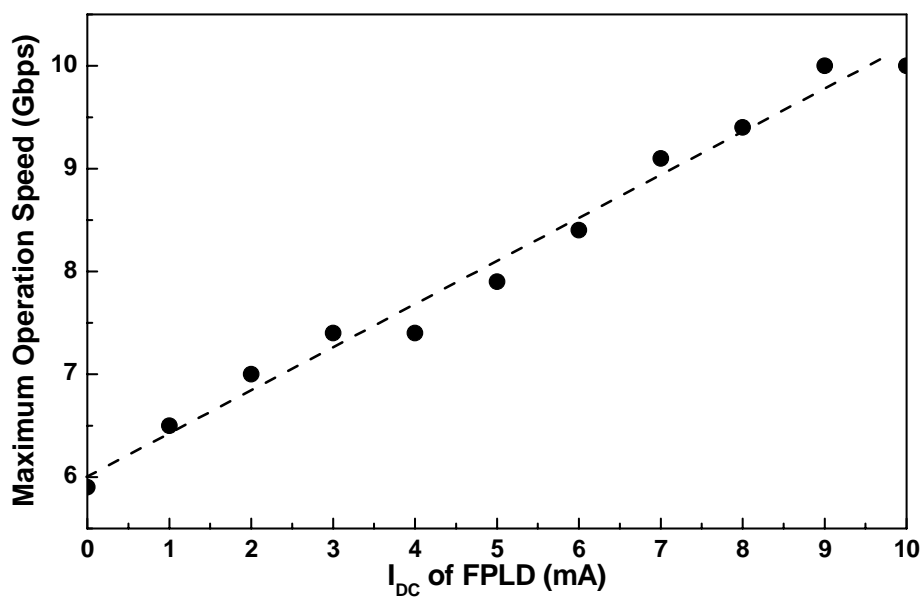


Fig. 3.23 The dependence of operation data rate on FPLD's DC bias current.

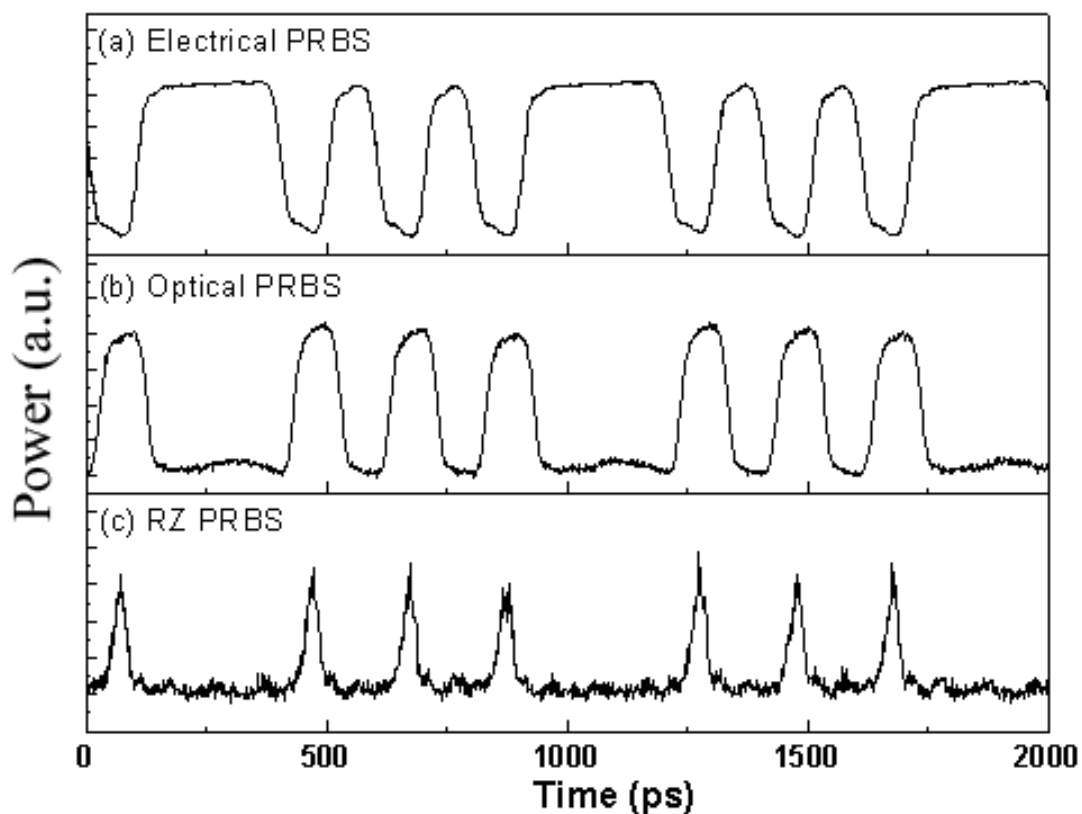


Fig. 3.24 The patterns: (a) the electrical NRZ data before the MZM; (b) the PG-encoded external injection light; (c) the converted RZ signal generated from the injection-locked FPLD. The data rate is 9.953 Gbit/s.



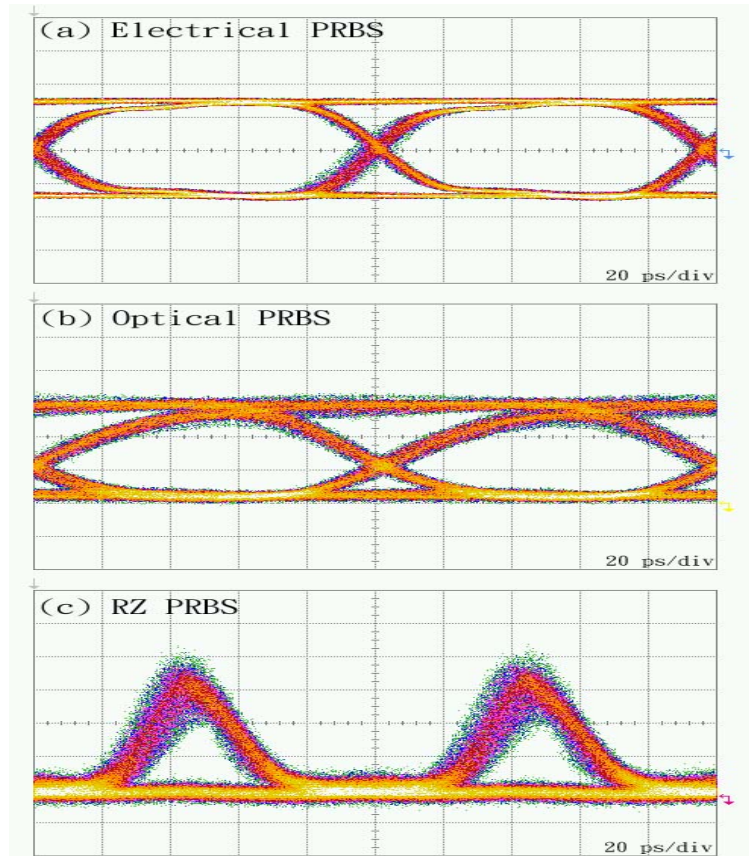


Fig. 3.25 The corresponding eye diagrams: (a) the electrical NRZ data before the MZM; (b) the PG-encoded external injection light; (c) the converted RZ signal generated from the single-mode FPLD. The data rate is 9.953 Gbit/s.

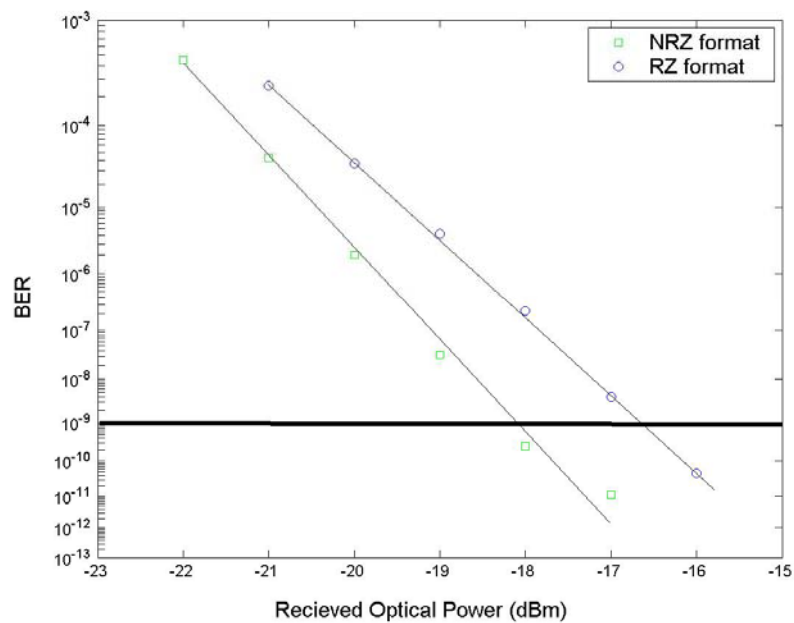


Fig. 3.26 The BER against the received optical power for NRZ-encoded external injection light and converted RZ signal at data rate of 9.953 Gbit/s.

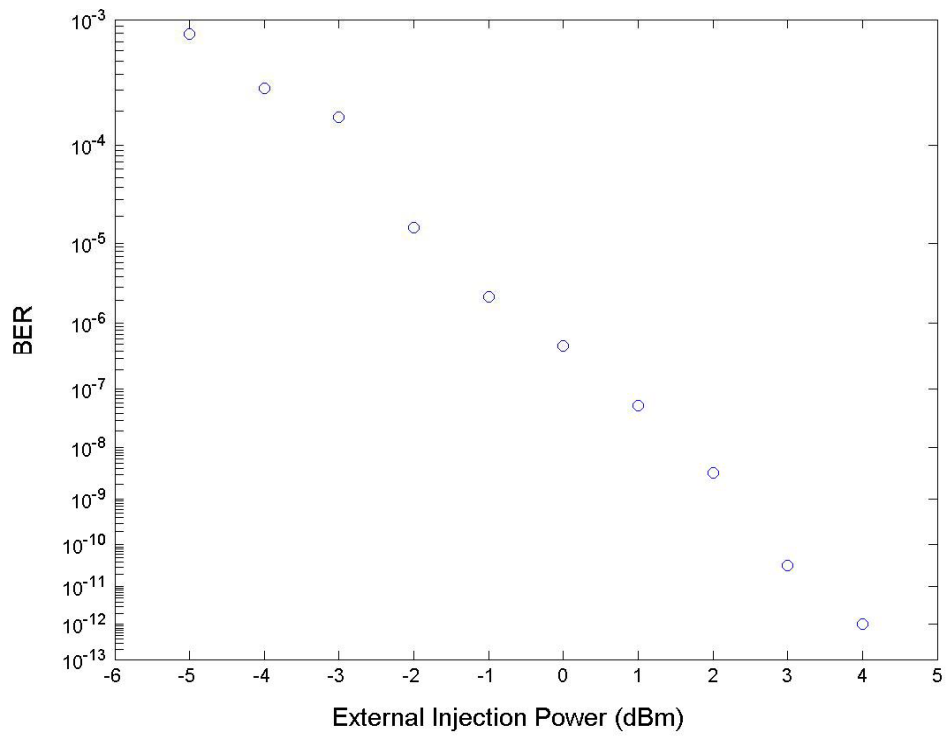


Fig. 3.27 The BERs for different external injection powers at data rate of 9.953 Gbit/s.



# Chapter 4

## Injection-locking Laser Diode based OC-192 optical NRZ-to-RZ OR Logic Gate

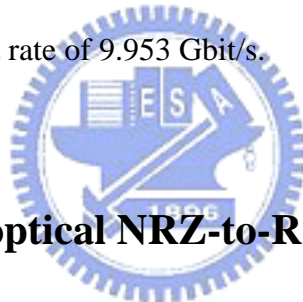
### Abstract

An OC-192 optical return-to-zero (RZ) formatted OR logic gate is experimentally demonstrated and theoretically interpreted for the first time, which is implemented using an optically injection-locked Fabry-Perot laser diode (FPLD) based data format converter modulated at below threshold condition. By injecting two non-return-to-zero data-streams into the FPLD-based OR gate, a peak-power-equalized RZ-formatted OR logic data-stream extinction ratio of  $>8$  dB is obtained from the FPLD with optimized rf modulating and optical injecting powers of 24.7 dBm and  $>-4$  dBm, respectively. Highest data rate up to 12.5 Gbit/s with a BER of  $10^{-12}$  at a received optical power of  $>-16$  dBm can be achieved by increasing the dc bias current of the FPLD-based RZ-formatted OR logic gate to 8 mA. The OR gated RZ data-stream exhibits a duty cycle (pulsewidth) of is  $\sim 27\%$  (27 ps) and a 0.5-dB power penalty at a BER of  $10^{-9}$  at data rate of 9.953 Gbit/s.

### 4.1 Introduction

Optical signal processing is the key technology in ultrahigh-speed networks to replace the cumbersome optical-electrical-optical conversion. Versatile researches were conducted to implement optical logic functionalities for important computing and encryption/decryption applications. Patel *et al.* have previously demonstrated the OR and NOR logic gates at 10

Gbit/s using an ultrafast nonlinear fiber interferometer [128]. The XOR functionality implemented using a terahertz fiber-optic asymmetric demultiplexer [129]. These schemes can be simplified using an integrated SOA based Mach-Zehnder interferometric wavelength converter (IWC), which offers a polarization- and wavelength-independent operation on optical XOR logics at 5 Gbit/s [130, 131]. Later on, the optical logic OR gates up to 10 Gbit/s were also achieved with aforementioned IWC [132]. Nonetheless, the demonstration of all-optic logic functions with laser diodes was seldom addressed. In this letter, a novel optical OR logic gate with nonreturn-to-zero-to-return-to-zero (NRZ-to-RZ) data-format converting function at bit rate up to 12.5 Gbit/s is primarily demonstrated by injecting the optical data into a Fabry-Perot laser diode (FPLD) modulated at just below threshold condition. The optical FPLD-based RZ-formatted OR logic gate is parametrically analyzed at a bit rate of 9.953 Gbit/s.



## **4.2 FPLD-Based All-optical NRZ-to-RZ OR Logic Gate**

The configuration of the rf-modulated FPLD-based OR logic gate is shown in Fig. 4.1. Two transmitted data-streams at 9.953 Gbit/s are generated from a distributed feedback laser diode (DFBLD) with monolithically integrated electro-absorption modulator, which is encoded by a  $2^{23}-1$  pseudorandom binary sequence NRZ pattern and amplified by erbium-doped fiber amplifier (EDFA). The rf clock tapped from the input channel and recovered by a commercial clock and data recovery unit (CDR, Agilent 83434) is then amplified to modulate the FPLD. The FPLD exhibits a threshold current of 11 mA and a longitudinal mode spacing of 1.2 nm, which is operated at below threshold condition by appropriately adjusting the amplified rf power. That is, the FPLD is un-lasing without input data. The wavelengths of the FPLD and the DFBLD (at 1550.92 nm originally) were controlled within lock-in range to achieve injection-locking operation. Afterwards, the

optical NRZ data-streams were sent into the input port of the FPLD-based OR logic gate via a fiber-optic coupler, and the RZ-formatted output of the OR gate was amplified by an EDFA. An optical bandpass filter (OBPF) was used to eliminate the excess amplified spontaneous emission (ASE) noise from the EDFA, providing the data with a smaller dc offset level and a better SNR.

In experiment, an increased dc bias for enhancing the modulating bandwidth up to >10 GHz and a reduced rf power for keeping the FPLD un-lasing are necessary. By increasing the dc biasing current of the FPLD to 8 mA, the FPLD-based OR logic gate at the data rate of >10 Gbit/s can be achieved, which is eventually limited by the carrier lifetime and the maximum biasing level of the FPLD. Figure 4.2 shows the input data-streams in different channels (Figs. 4.2a and 4.2b), the output data-stream combined using 50% coupler (Fig. 4.2c), and the pulsed data-stream output from the FPLD-based RZ-formatted OR logic gate (Fig. 4.2d) at a SONET data rate of 9.953 Gbit/s (OC-192). The pulsewidth of the each high-level bit in the RZ-formatted data-stream is 27 ps (with a duty cycle of ~27%). The RZ-formatted logic OR gate is demonstrated with unequal output bit levels in the data format converter mode, as shown in Fig. 4.2(d). The power injected into the rf-modulated FPLD is the sum of powers from two coupled data-streams, indicating that the output power level coupled by two input bits of “1” + “1” could be different from that by bits of “1” + “0” or “0” + “1”, as shown in Fig. 4.2(c).

The below threshold operation of the FPLD also causes a linear relationship between the extinction ratio and injecting power, as shown in Fig. 4.3. The drawback in injection-power-dependent output inequality of such an OR logic gate makes it sensitive to the external-injection power level while both of the threshold current and the P-I slope are decreased due to the enlarged external-injection power, as depicted in Figs. 4.4 and 4.5. Nonetheless, the offset P-I curves at different injection powers can coincide with one another due to the gradually reduced slopes of P-I curves at lasing condition (see the dashed

circle of Fig. 4.4). Therefore, by slightly increasing the rf modulating power of the FPLD to reach the coincident point of these P-I curves, the power dependency of the OR gated output level can be released. This helps to obtain an external-injection-power-independent operation for the FPLD-based RZ-formatted OR logic gate at a cost of smaller extinction ratio (due to the self-gain-switching under injecting bit of “0”). At the rf power of 24.7 dBm, the output peak powers of the high-level RZ-formatted data bits have been equalized (Fig. 4.6). A tiny gain-switched pulse appears at injecting bit of “0” under larger rf modulating power, which somewhat degrades the extinction ratio of the output data. Although the extinction ratio of the output data is sacrificed by 3 dB under the increased rf modulating power, the OR gate becomes insensitive to the injection power over a wide tuning range.

Although the increase of the DC biasing current can improve the modulating bandwidth of the FPLD, a larger dc current fails to enhance more the data-converting and OR-gating rate, which greatly degrades the BER and ER performances of the converted pulsed data due to the lasing of the FPLD even without external injection. In addition, the improper synchronization between the rf clock and the injected data-stream also leads to an error in NRZ-to-RZ conversion when the lagging time exceeds over 30 ps (*i.e.* the synchronous timing window is 30 ps) at 9.953 Gbit/s. In comparison with the wavelength converted OR gate reported previously [132], our proposed scheme provides a wavelength injection-locked, NRZ-to-RZ format converted, and OR operation simultaneously.

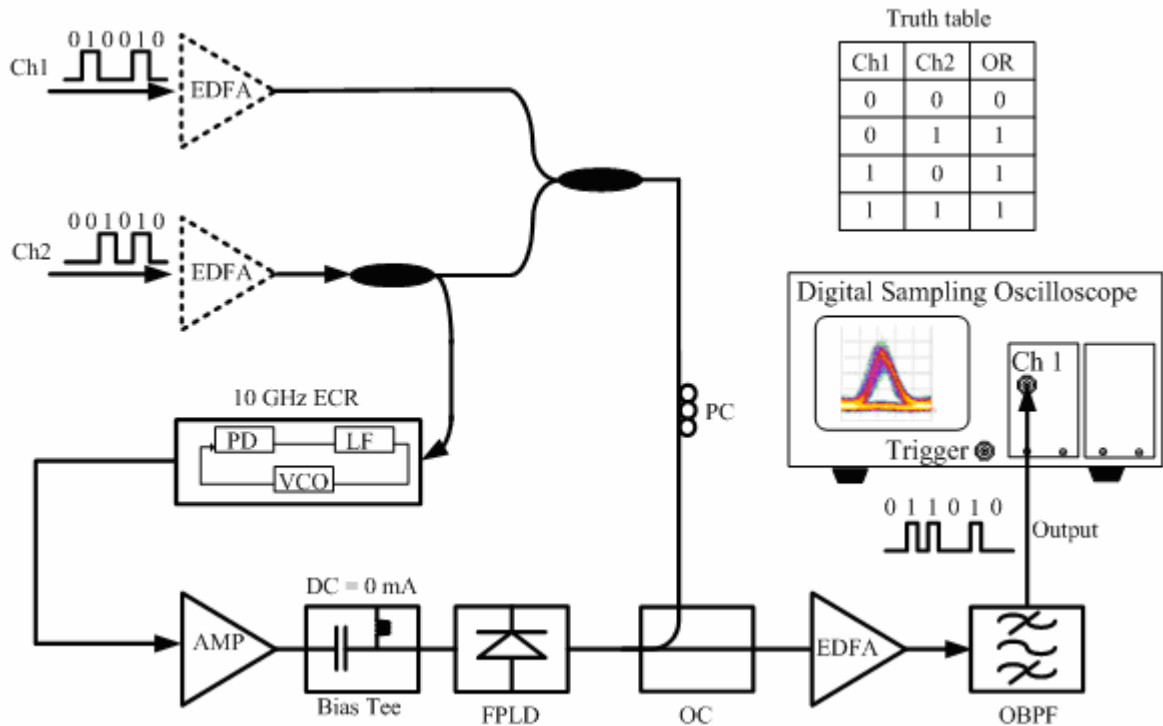


Fig. 4.1 Experimental setup and the truth table of the FPLD-based logic OR gate. AMP: rf amplifier; CDR: clock/data recovery unit; Ch1: input channel 1; Ch2: input channel 2; EDFA: erbium-doped fiber amplifier; FPLD: Fabry-Perot laser diode; OBPF: optical bandpass filter; OC: optical coupler.

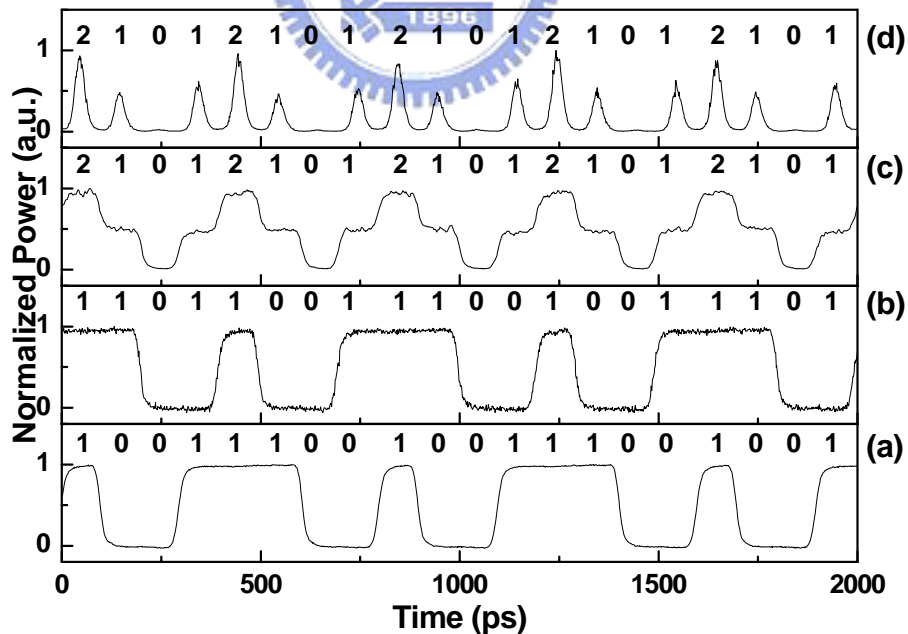


Fig. 4.2 The monitored data patterns. (a) and (b): two input NRZ data-streams; (c): passively combined data-stream; (d) the output data-stream (with the FPLD modulated at below threshold condition).

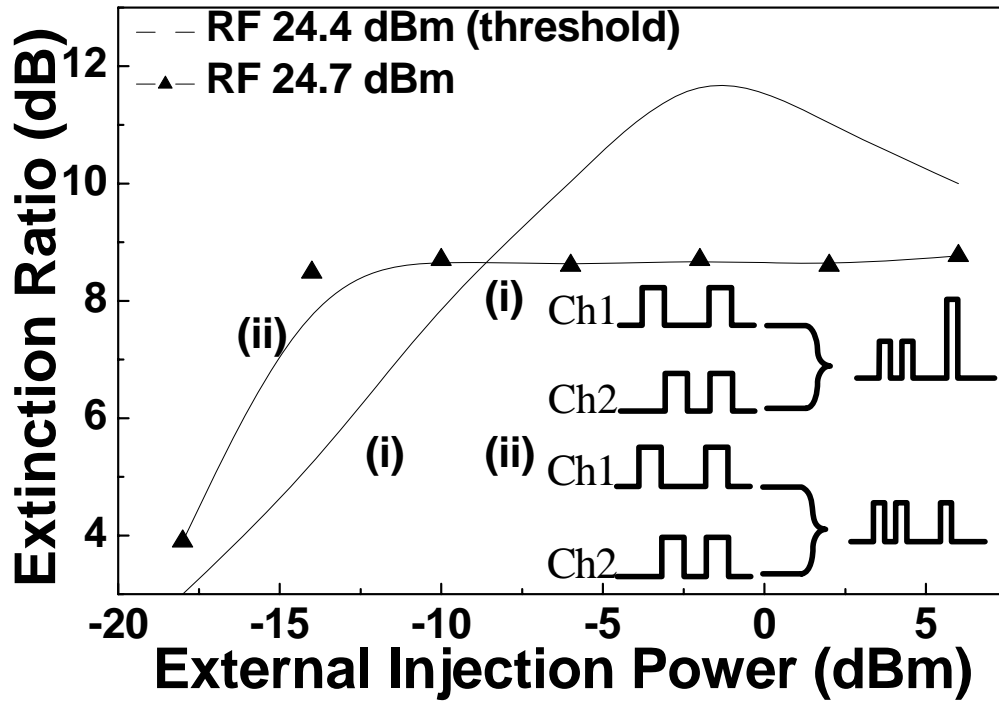


Fig. 4.3 The power dependent extinction ratio of the RZ-formatted data at rf-modulating power of (i) 24.4 dBm and (ii) 24.7 dBm. Inset: the conceptual diagrams of (i) the power-dependent and (ii) the power-independent OR gating operations.

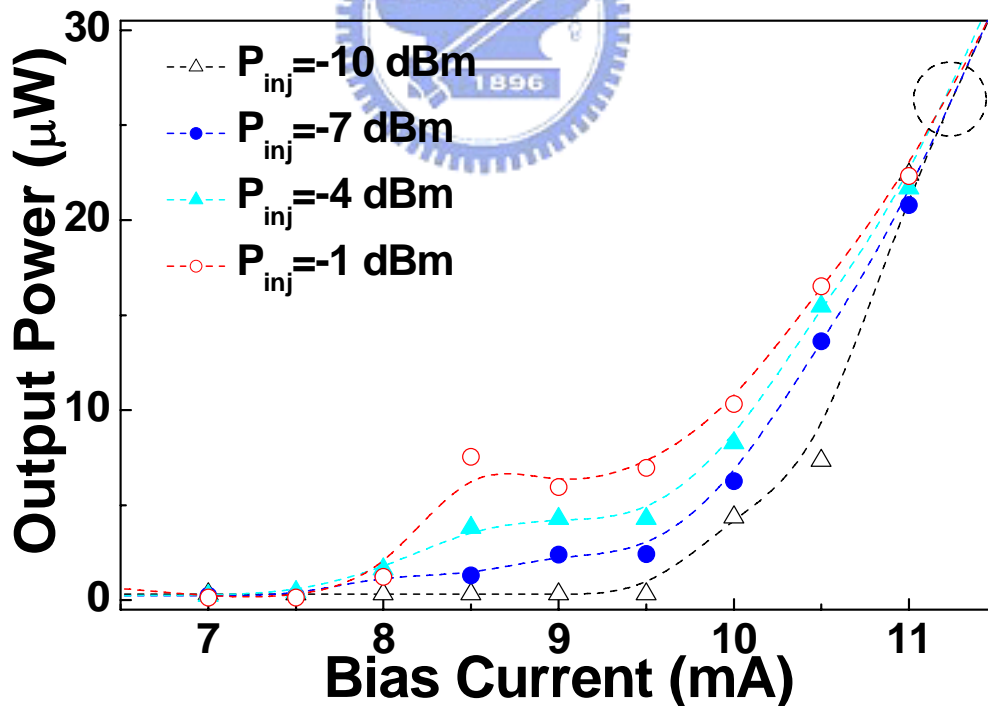


Fig. 4.4 P-I curves and of the rf-modulated and injection-locked FPLD for different injection power.



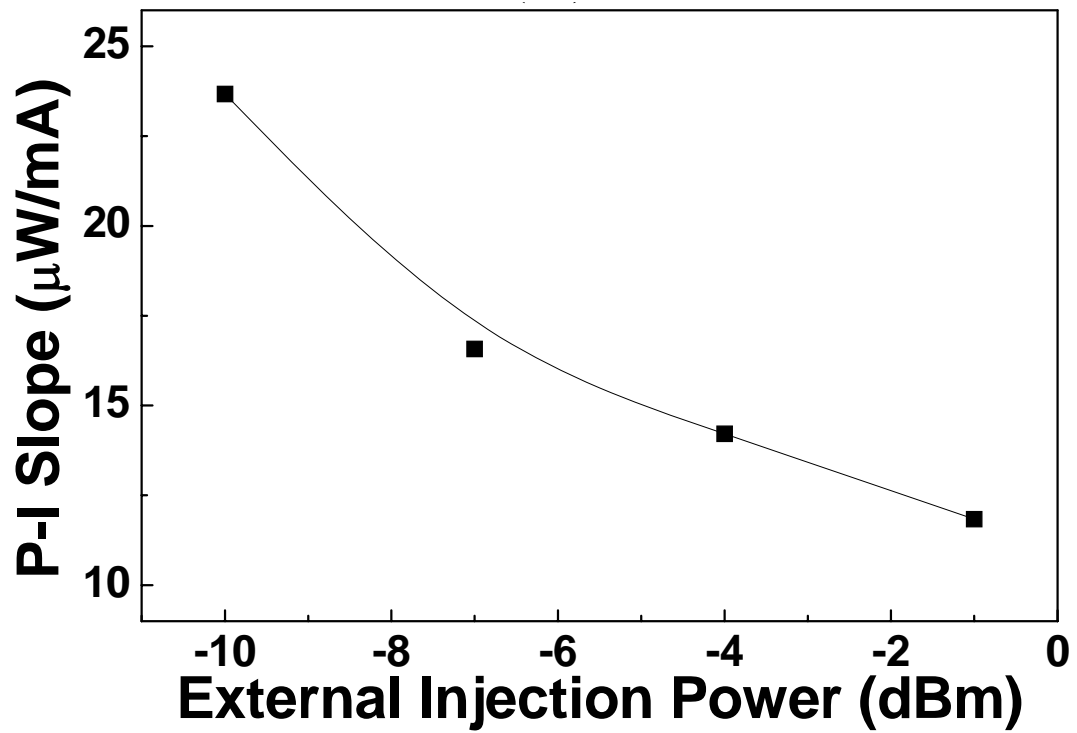


Fig. 4.5 P-I slope of the rf-modulated and injection-locked FPLD for different injection power.

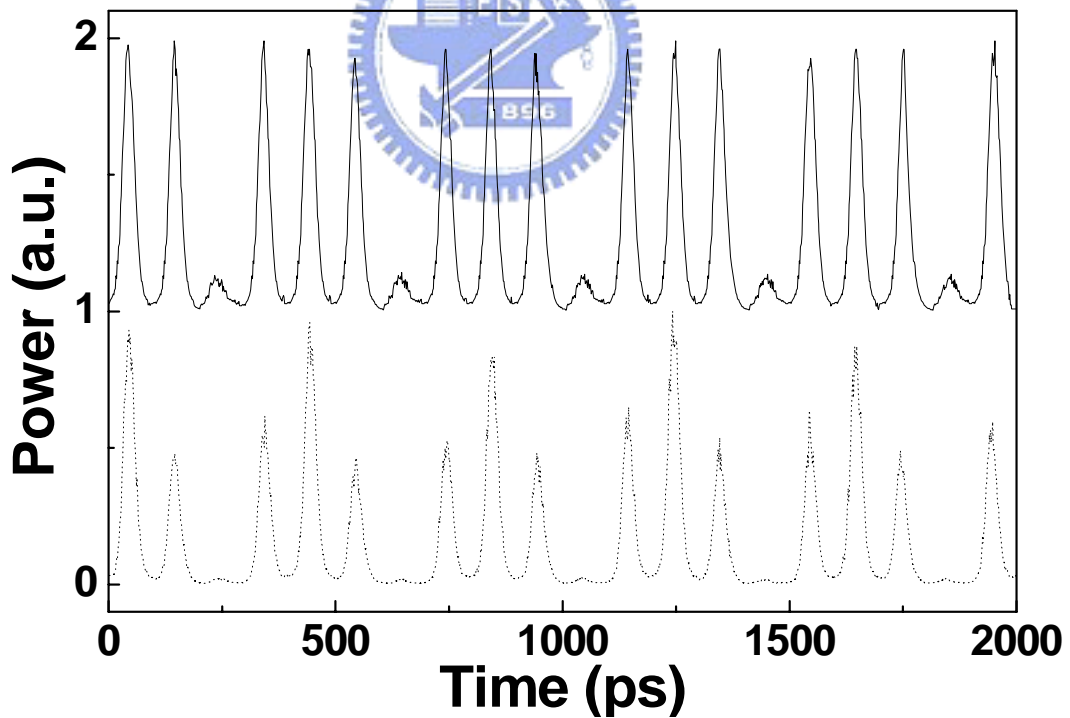


Fig. 4.6 The power-dependent (dotted trace) and power-independent (solid trace) logic OR output.

# Chapter 5

## Dynamic Chirp Characteristics in FPLD-based All-optical NRZ-to-RZ Data Format Converter

### Abstract

For long-haul transmission, soliton transmission is a promising technique. However, it is well known that the generation of transform-limited pulses from a directly modulated laser diode is difficult since a frequency downchirp inevitably occurs owing to carrier density modulation. A transform-limited pulse can further be obtained by using dispersion compensation fiber to compensate the chirp. On the other hand, injection locking has been proven that it can reduce the chirp in a gain-switched laser diode. In this Chapter, we measure static chirp (in injection-locking-induced gain-switching condition) and dynamic relative chirp (in NRZ-to-RZ condition) characteristics for the first time. A scenario of dynamic soliton is proposed for long-haul transmission.

### 5.1 Introduction

Directly modulated laser diodes (LD's) has red chirping of the LD carrier frequency, which is mainly responsible for limiting the bandwidth-distance product [133-136]. Over past years, many efforts [137, 138] have been devoted to enhancement of modulation bandwidth of semiconductor lasers. However, direct current modulation is inevitably accompanied by frequency chirping, which becomes the main limitation to utilize direct current modulation in high-bit-rate optical communication due to the chromatic dispersion of optical fibers.

This becomes more severe for higher modulation speed. Injection-locking offers a scheme to reduce the frequency chirping in modulated semiconductor lasers. Lately, it has been proposed [139-142] that, under stable injection locking where the frequency of the slave laser locks to that of the master laser, frequency chirping can be largely reduced. A few experiments have been conducted [142] to verify the theoretical prediction. However, they only emphasized on the condition of weak injection, where the stable locking range in terms of the frequency difference between the two lasers is relatively small. Under this condition, multi-gigabit-per-second direct modulation may unlock the originally injection-locked laser due to optical frequency variation that may exceed the frequency range of stable locking [142]. This may drive the laser system into periodic, or even chaotic, oscillations, resulting in degradation of the system performance. Hence, a larger range of stable locking is preferred for high modulation speed, which can be achieved by strong injection into the slave laser [143]. For strong injection locking, typically when the injection power is more than one percent of the circulating power inside the slave laser, the laser system not only has a larger range of stable locking but also has been demonstrated [140, 141, 144-146] to show significant enhancement in modulation bandwidth. A more than 3-fold enhancement has been theoretically predicted and experimentally verified. In 2003, Okajima *et al.* [147] demonstrated experimentally significant increase in the relaxation resonance frequency and substantial reduction in frequency chirping in an optically injection-locked semiconductor laser under direct current modulation. Significant bandwidth enhancement and chirp reduction are simultaneously achieved in their experiment. In this Chapter, we measure the static chirp (in injection-locking-induced gain-switching condition) and dynamic relative chirp (in NRZ-to-RZ condition) characteristics for the first time.

## 5.2 Evaluation of Chirp in FPLD-based NRZ-to-RZ Data Format Converter

Figure 5.1 is the experimental setup for measuring the static chirp (in injection-locking-induced gain-switching condition) and dynamic relative chirp (in NRZ-to-RZ condition) characteristics of the RZ-formatted pulse train. An optical chirpform test set (Advantest Q7606) connected with a digital sampling oscilloscope (Agilent 86100) is used to measure the dynamic relative chirp. A dispersion compensation module depicted in Fig. 5.1 is used for linear chirp compensation.

On the other hand, optical solitons in fibers are interesting because the fundamental soliton ( $N=1$  soliton) does not change its wave form along the fiber if the fiber has no loss [148]. In 1988, Mollenauer and Smith experimentally showed that optical solitons can propagate over 6000 km when a color-center laser is used [149]. They circulated 50-ps solitons in a 42-km fiber loop in which stimulated Raman scattering was used to compensate for the fiber loss. Later on, Nakazawa *et al.* showed an alternative way to amplify solitons by using an erbium-doped fiber amplifier (EDFA) [150, 151]. This is a powerful method of amplifying solitons because an average pump power of 100 mW is enough to achieve a gain of larger than 30 dB. By using a time-division-multiplexing technique, a 20-GHz soliton burst train is prepared and amplified with an EDFA [152], as shown in Fig. 5.2.

From a practical point of view, soliton generation from a laser diode is most desirable; however, it is well known that the generation of transform-limited pulses from a directly modulated laser diode is difficult since a frequency downchirp inevitably occurs owing to carrier density modulation [133-136]. Even in a distributed-feedback laser diode (DFBLD) transient spectral changes exist, which cause the nonlinear chirp-induced dispersion penalty. This is one of the important factors limiting the high-speed transmission of the DFB laser

signal in linear schemes. In addition, the transform-limit condition is also important in soliton transmission.

In 1990, Nakazawa *et al.* proposed a method to generate and transmit transform-limited solitons from a directly modulated bulk DFBLD, using a narrow-band optical filter and erbium-doped fiber amplifiers [153-155]. They successfully demonstrated an error-free soliton transmissions at 3.2 and 5 Gb/s over 100 km [153]. Their experimental setup is shown in Fig. 5.3.

A preemphasis technique [156] is used for repeating the soliton, in which  $N=1.2-1.4$  solitons are excited in each soliton fiber. Here we review their experimental arrangement briefly. The laser source used for soliton generation is a bulk-type distributed-feedback laser diode, which is gain-switched by a sinusoidal current modulation in the GHz range to generate a 27 ps pulse train with the average output power of 2-3 mW. However, the pulse is far being in a transform-limited condition. Furthermore, by using a Fabry-Perot resonator (FPR) as a narrow-band spectral filter, transform-limited pulses are obtained although such a filter decreases the average transmitted power to 1/10 of the input power. They observed that the overall chirp is nonlinear across the whole pulse width, although the center is linear. It is also evident that the chirp rate increases when a large ac modulation is applied. When the bandwidth of the FPR is set at 0.4-0.8 nm, linearly chirped pulses are observed, which will be completely compensated by a fiber with a positive group-velocity dispersion. The result after 0.2-nm spectral filtering shows that the pulse width is reduced from 27 ps to 17 ps and the chirp is negligible. By using such a spectral filtering technique, a transform-limited pulse train with the pulse width-bandwidth product of  $\Delta\tau\Delta\nu = \Delta\tau\left(\frac{\Delta\lambda\cdot c}{\lambda^2}\right) = 0.43 - 0.45$ , where  $\Delta\tau = 17$  ps and  $\Delta\lambda = 0.20 - 0.21$  nm, is obtained [155].

## 5.3 Results and Discussion

According to this scenario, we apply the preemphasis technique to our RZ-formatted data. Figure 5.4 is the temporal trace of our RZ-formatted pulse by injection-locking the synchronously-modulated FPLD just below threshold current. The pulse width is 71 ps and the data rate is 2.488 GHz. Figure 5.5 shows the corresponding optical spectrum with the 3-dB spectral width of 0.146 nm. The pulse width-bandwidth product ( $\Delta\tau\Delta\nu$ ) is 1.32, which is much larger than the value of 0.44 for a transform-limited Gaussian pulse.

Due to the nature of red-shifting chirping, compression of negatively chirped pulse in the time domain is possible if a fiber with normal dispersion ( $\beta_2 = d^2\beta/d\omega^2 > 0$ ,  $\beta$ : propagation constant,  $\omega$ : carrier angular frequency) is provided.

In such a fiber, the group velocity ( $v_g^{-1} = d\beta/d\omega$ ) of a shorter wavelength signal will be less than that of a longer wavelength signal. Thus, if we mentally break up the chirped pulse into a number of segments, each with a slightly different group velocity, the leading edge of the negatively chirped pulse will travel slower than the trailing edge, resulting in temporal compression. In 1991, Liu *et al.* [157] analyzed the propagation of a chirped pulse in a dispersive fiber by assuming the optical output from the gain-switched laser to be with a Gaussian profile and linear chirping [158]. They provided, at the first-order approximation, an explicit expression for the optimum compression condition as follows [157]:

$$-DL = \frac{\Delta t}{\Delta\lambda} \quad (5.1)$$

where  $D = -2\pi c\beta_2/\lambda^2$  is the fiber dispersion parameter in ps/nm-km,  $L$  is the fiber length,  $\Delta t$  is the full width at half maximum (FWHM) of the input pulse, and  $\Delta\lambda$  is the chirped spectral width. For the purpose of extracting more power, we chose a dispersion compensation fiber (DCF;  $D = -90.5$  ps/nm•km at 1537 nm) to perform temporal compression. Therefore, the optimum compression can be achieved when the propagation

distance is equal to 5.37 km. According to Liu's report [157], the optical spectrum will be invariable and the pulse width-bandwidth product will be reduced from 1.32 to 0.44. In such a condition, a transform-limited pulse with pulse width of 23.7 ps will be expected.

Furthermore, to excite  $N = 1.4$  soliton, the peak power  $P_0$  and the average power  $P_{avg}$  calculated from the listed formulas of Table 5.1 are 7.12 mW and 0.252 mW, respectively. Therefore, a soliton transmission using preemphasis technique [156] is expected to work, in which an erbium-doped fiber amplifier is installed every 25-km dispersion shifted fibers as a lumped amplifier, as shown in Fig. 5.6.

The linewidth of the modulated FPLD can be reduced by using injection locking technique. Figure 5.7 is the measured chirp characteristic in a conventional gain-switching pulse (*i.e.* free-running). Chirping toward shorter frequency corresponds to the direction from the leading edge to the trailing edge. The amount of red chirping is 14.252 GHz. When the synchronously modulated FPLD is injection-locked to generate an injection-locking-induced pulse, the chirp in such a pulse is largely reduced, as shown in Fig. 5.8. On the other hand, by injection-locking the FPLD via an NRZ data stream, the generated gain-switching pulse has a smaller chirp than that in free-running condition, as shown in Fig. 5.9. The chirp in injection-locking-induced gain-switching pulse is named as a back-to-back chirp (*i.e.*, without any chirp compensation). We can find that there is a down-chirp from 7 GHz to -5.17 GHz (*i.e.* the amount of red chirping is 12.17 GHz) at the central part of the pulse. By using a spool of 25-km Corning MetroCor fiber ( $D = -9.1 \text{ ps/nm-km}$ ) a chirp reduction in RZ-formatted data stream is measured. By contrast, a 25-km standard single mode fiber is used to observe the variation of the chirp in RZ-formatted data stream. However, we do not find an evident increase in chirp. Figure 5.10 shows curves of the dispersion parameter versus the wavelength for standard single mode fiber, Corning MetroCor fiber, and dispersion compensation fiber. According to this

figure, the estimated length of the dispersion compensation fiber for obtaining a chirp-free RZ using spectral windowing technique is 5.37 km. When an 8-km DCF is used to compensate the RZ-formatted data stream, an over-compensated result is found, as shown in Fig. 5.11. We can find that the RZ-formatted data stream is changed from red-chirping to blue-chirping with almost the same amount. In addition, the pulse widths after passing through different compensation fibers are shown in Fig. 5.12. Therefore, we may expect that half a length of DCF fiber may fully compensate the linear chirping of the RZ-formatted data stream. Furthermore, a scenario of dynamic soliton [159] may work for long-haul transmission using preemphasis technique.





**Table 5.1**Formulas of calculation for exciting  $N = 1.4$  soliton

Parameter	Symbol	Value	Unit	Ref.
Nonlinear refractive index	$n_2$	$3.2 \times 10^{-20}$	$\text{W/m}^2$	
Central wavelength	$\lambda_0$	1537.048	nm	
Central frequency	$\omega_0 = 2\pi c/\lambda_0$	1226.348	THz	
Width parameter	$w$	3.6	$\mu\text{m}$	JAP 66 (1989) 2803
Speed of light	$c$	$3 \times 10^8$	m/s	
Effective core area	$A_{\text{eff}} = \pi w^2$	$4.07 \times 10^{-11}$	$\text{m}^2$	
Pulse width (FWHM)	$T_{\text{FWHM}}$	23.7	ps	
Half-width (at 1/e-intensity point)	$T_0 = \frac{T_{\text{FWHM}}}{2(\ln 2)^{1/2}} \approx \frac{T_{\text{FWHM}}}{1.665}$	14.23	ps	
Nonlinear parameter	$\gamma = \frac{n_2 \omega_0}{c A_{\text{eff}}}$	3.21	1/W-km	
Soliton order	$N$	1.4		
Dispersion parameter	$D = -\frac{2\pi c}{\lambda^2} \beta_2$	$-1.89 @ 1537 \text{nm}$	ps/nm-km	
Group-velocity dispersion (GVD)	$\beta_2$	2.36	$\text{ps}^2/\text{km}$	
Peak power	$P_0 = \frac{ \beta_2  N^2}{\gamma T_0^2}$	7.12	mW	
Average power	$P_{\text{avg}} = P_0 \times f \cdot T_0$	0.252	mW	

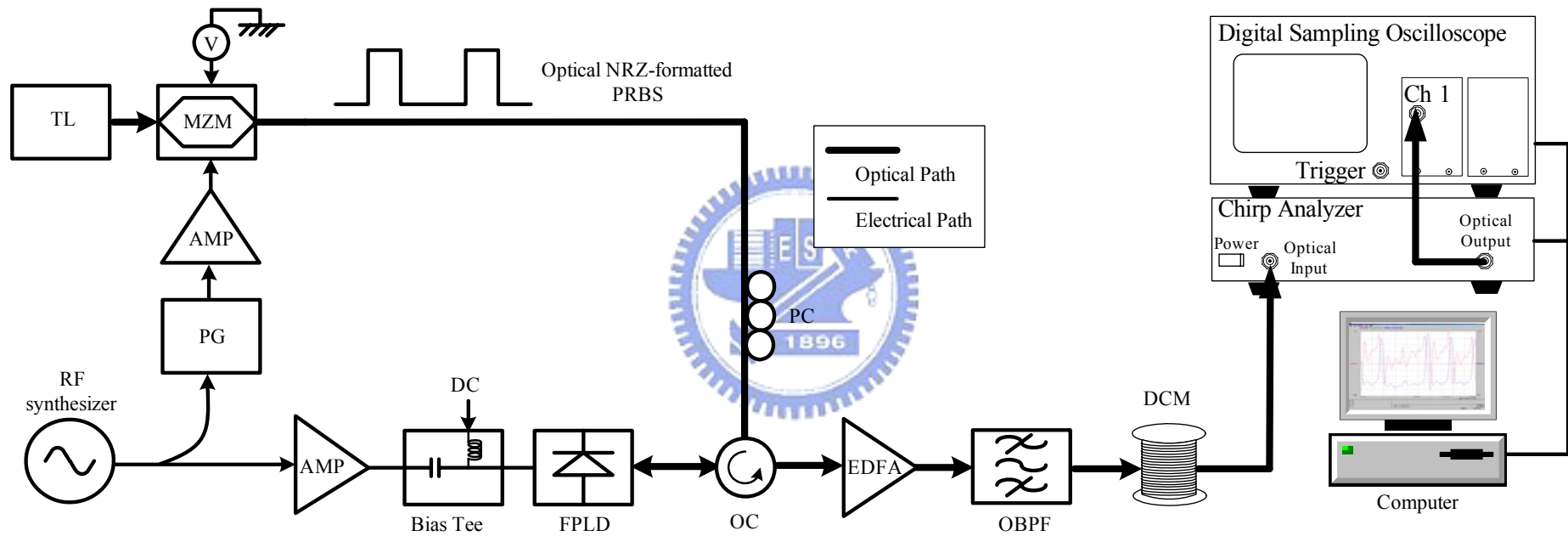


Fig. 5.1 Experimental setup for measurement of the dynamic chirp of the RZ-formatted data stream. DCM: dispersion compensation module.

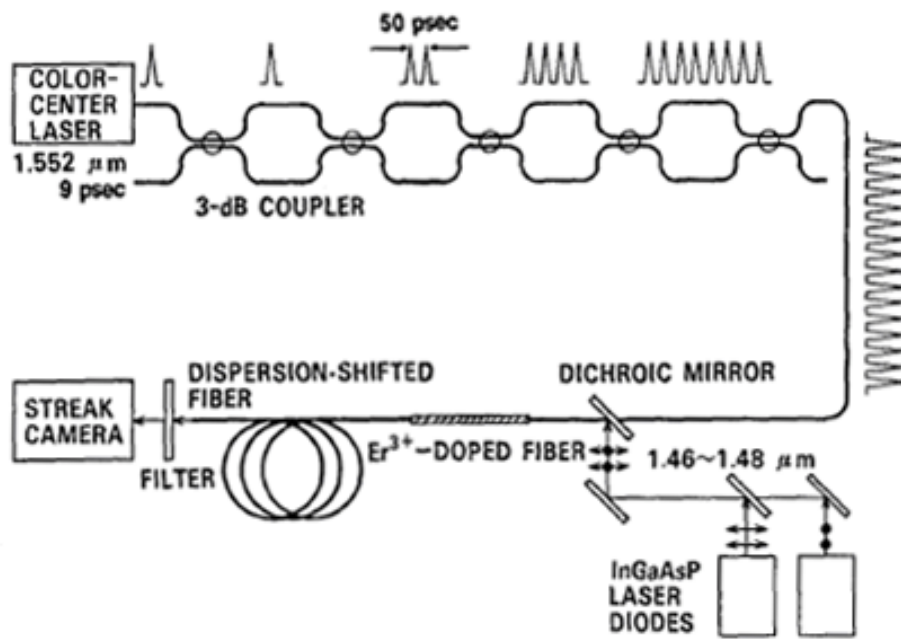


Fig. 5.2 Experimental setup for 20-GHz soliton amplification and transmission. [M. Nakazawa, K. Suzuki, and Y. Kimura, *Opt. Lett.* 14, 1065 (1989).]

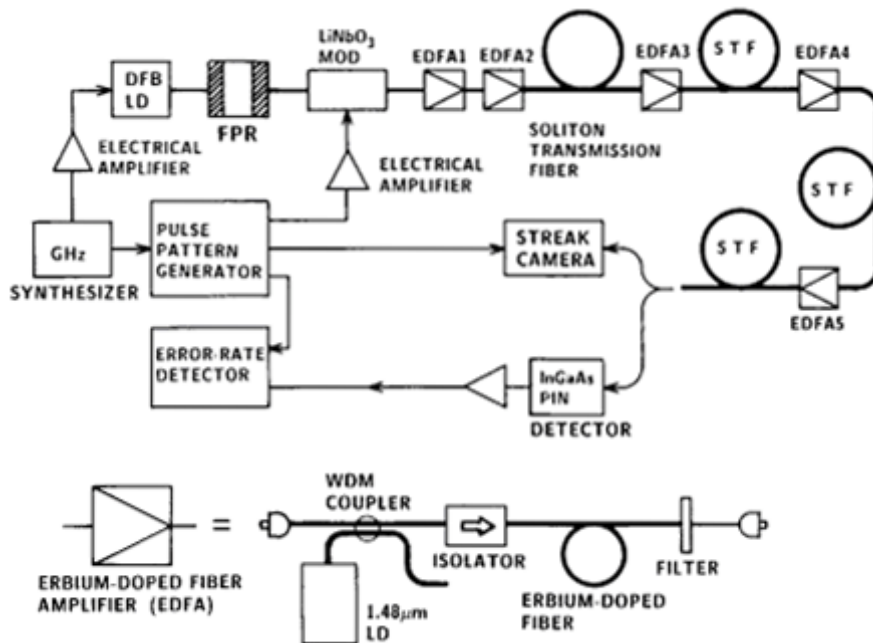


Fig. 5.3 Experimental setup for soliton transmission with a preemphasis technique using erbium-doped fiber amplifiers and repeaters. [M. Nakazawa, K. Suzuki, and Y. Kimura, "3.2-5 Gb/s, 100 km Error-Free Soliton Transmissions with Erbium Amplifiers and Repeaters," *IEEE Photon. Technol. Lett.* 2, 216 (1990).]

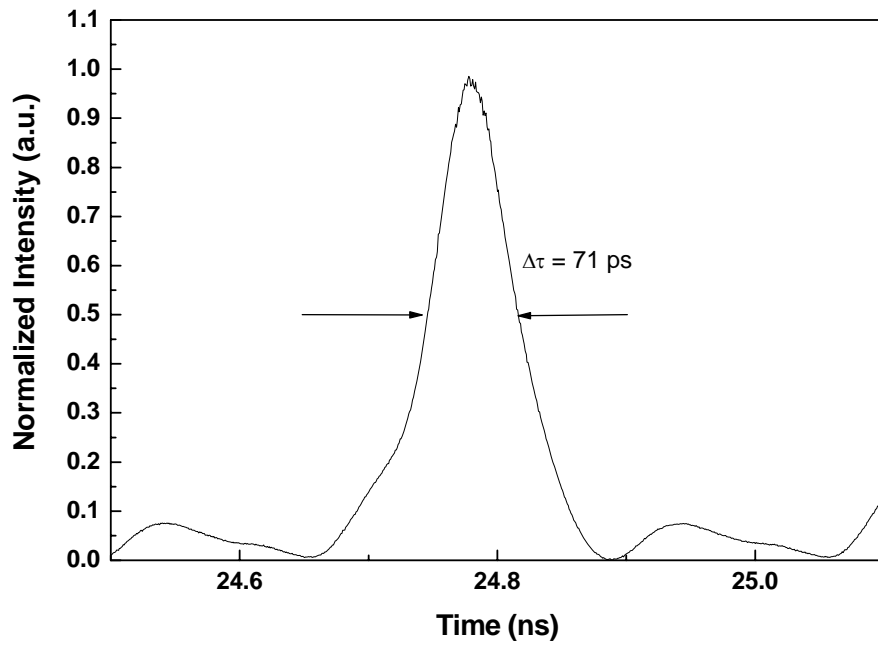


Fig. 5.4 Temporal trace of our RZ-formatted data by injection-locking the synchronously-modulated FPLD just below threshold current.

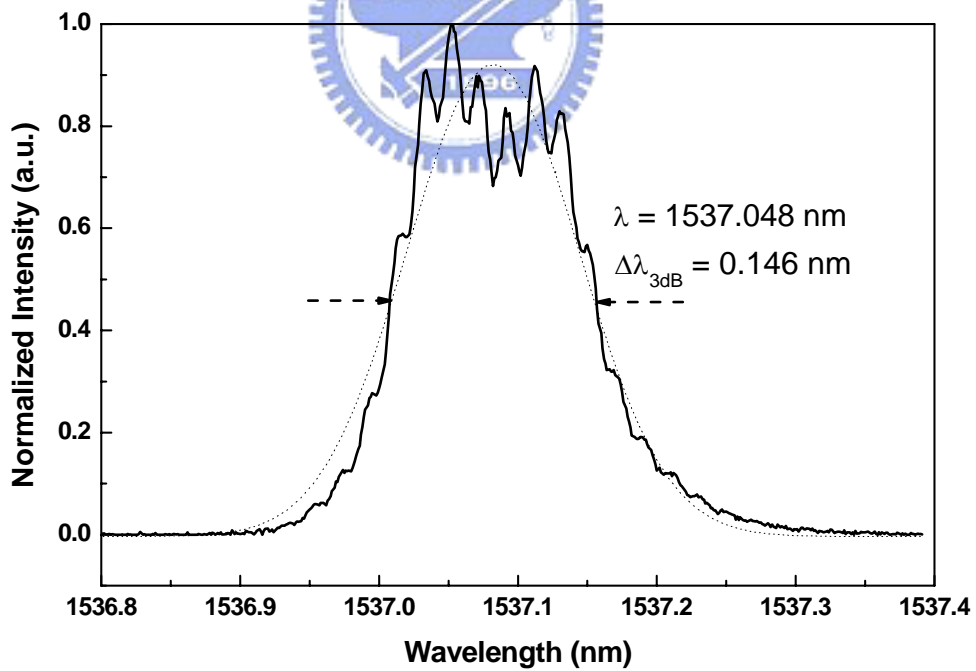


Fig. 5.5 Optical spectrum of the RZ-formatted data stream.

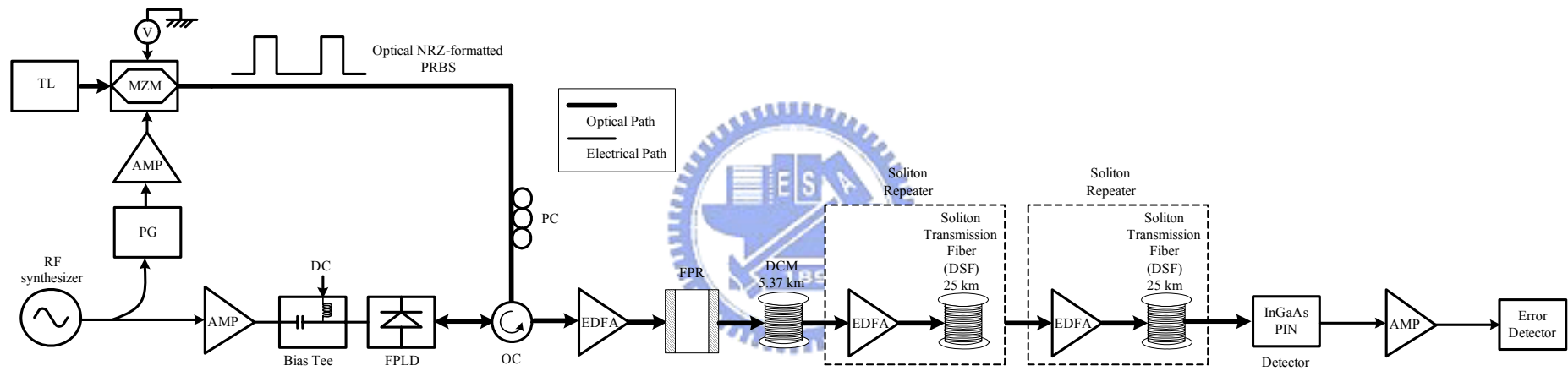


Fig. 5.6 Proposed experimental setup for soliton transmission for NRZ-to-RZ data format converter.

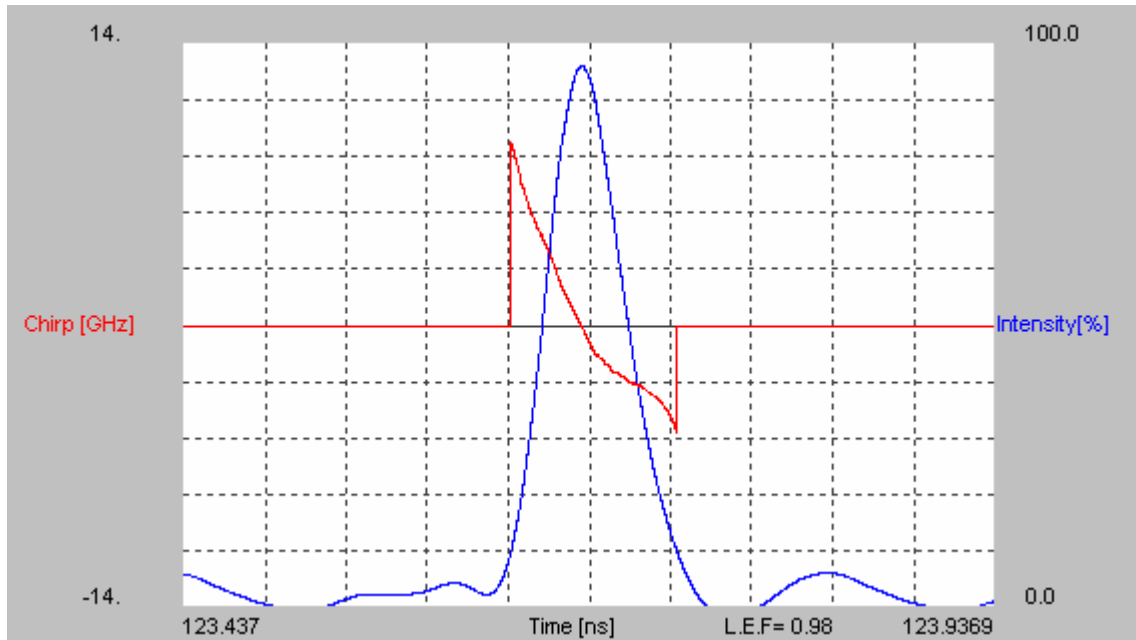


Fig. 5.7 Chirp characteristic in conventional gain-switching pulse.

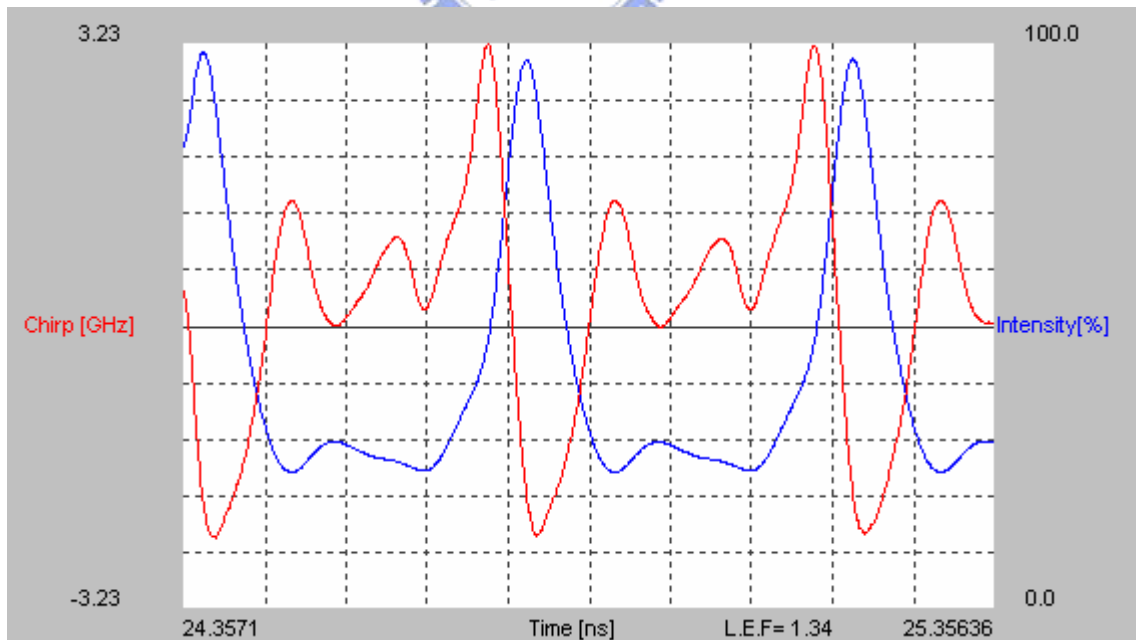


Fig. 5.8 Chirp characteristic of an injection-locking-induced pulse train.

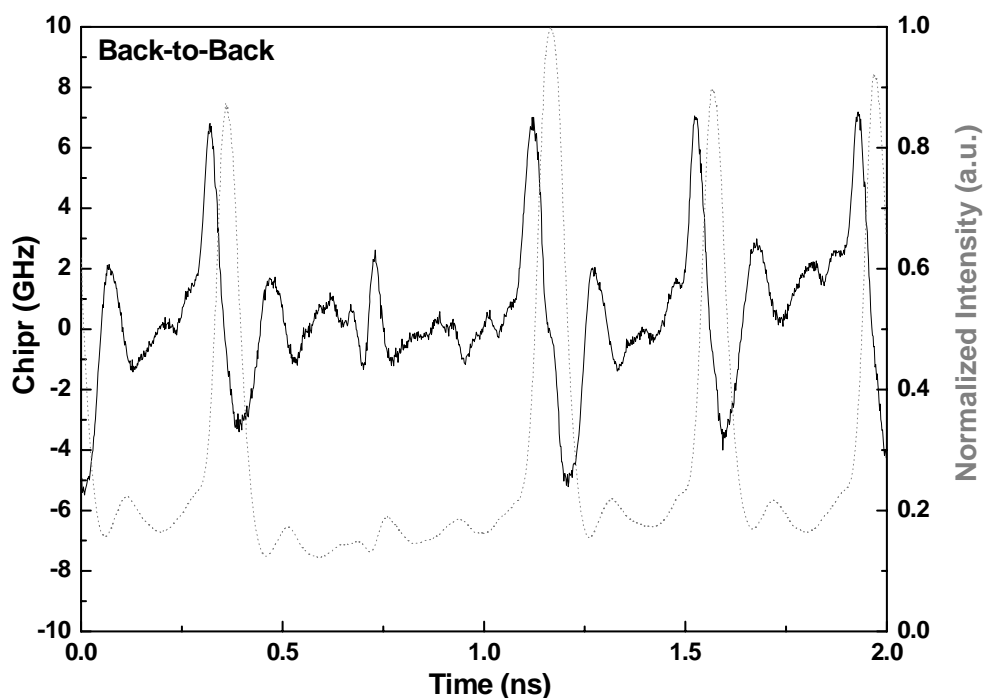


Fig. 5.9 Dynamic chirp of an injection-locking-induced data stream.

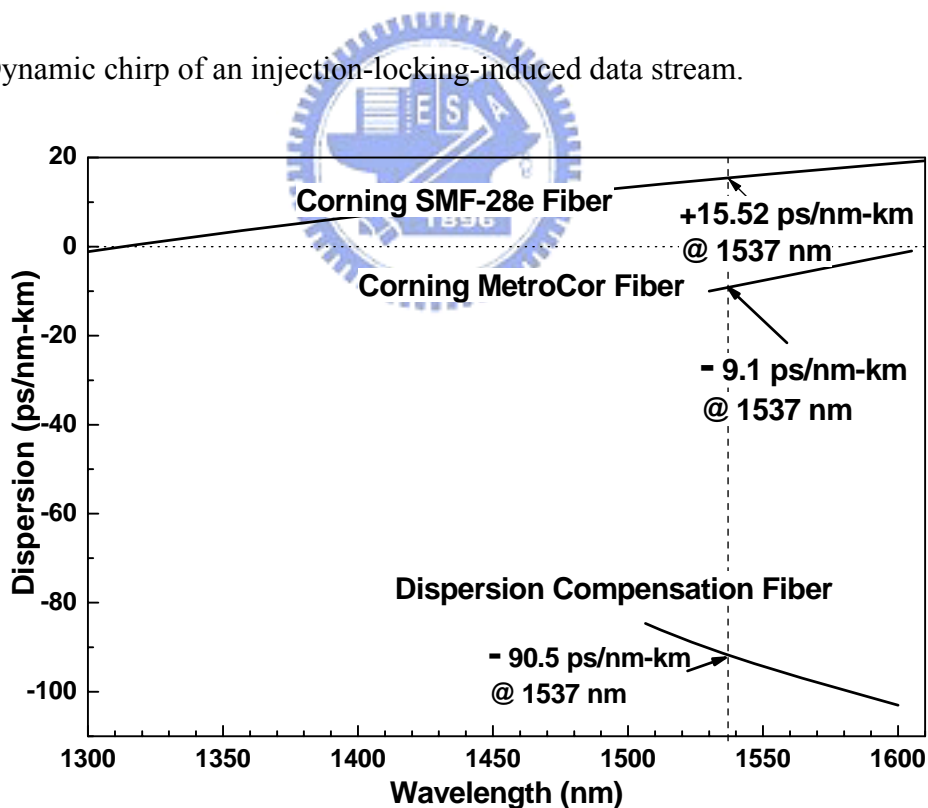


Fig. 5.10 Curves of the dispersion versus the wavelength for standard single mode fiber, Corning MetroCor fiber, and dispersion compensation fiber.

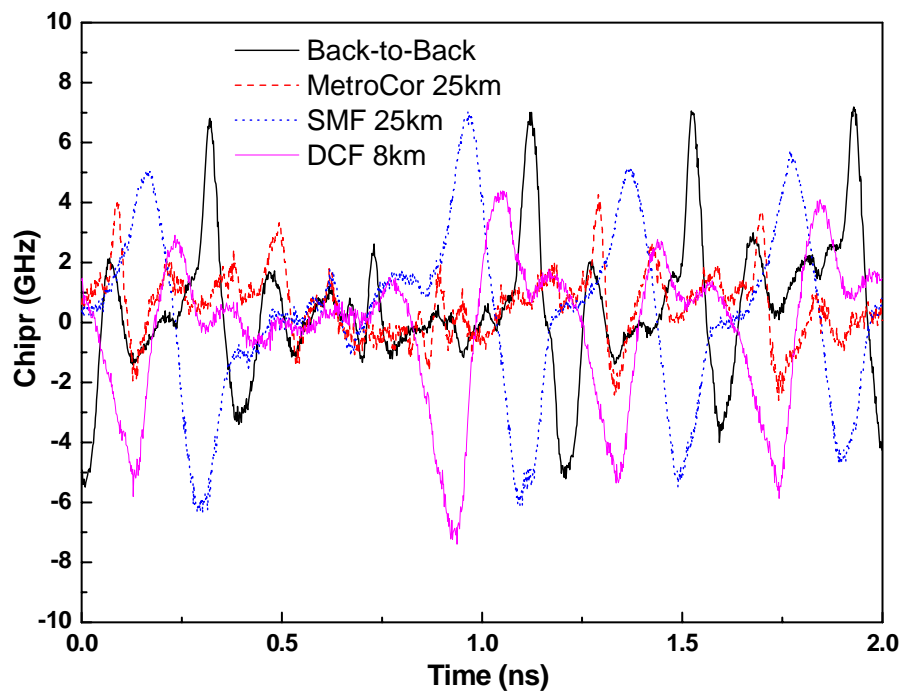


Fig. 5.11 Chirping results of RZ-formatted data stream after passing through different fibers.

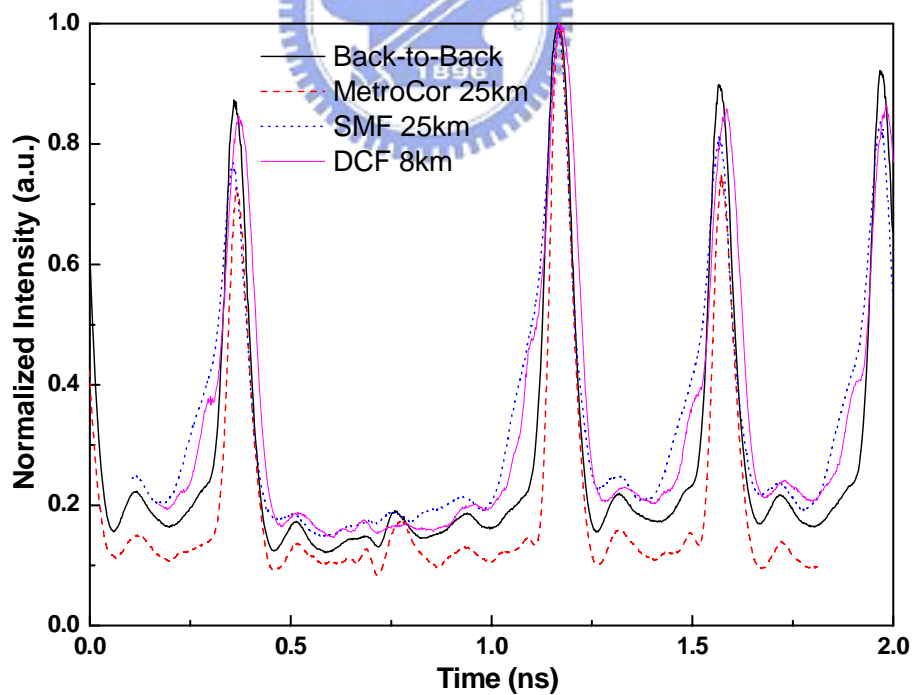


Fig. 5.12 Pulse widths of RZ-formatted data stream after passing through different fibers.



# Chapter 6

## Conclusions

### 6.1 Summary

To date semiconductor lasers have been considered the best light sources for high-bit-rate optical communication lines and fast optical data-processing systems. Compared to solid-state, gas, and dye lasers, the diode laser offers a considerably smaller size, higher efficiency, lower cost, and the unique ability to be modulated up to gigahertz rates by simply changing the driving current through the device. Concurrently, to realize the potentially very high capacity of lightwave system, the light source used should be able to generate short pulses at high repetition rates and capable of being modulated and encoded.

In metropolitan network a nonreturn-to-zero (NRZ) format is usually used for low bit-rate transmission due to the lower requirement of the electronic bandwidth. However, such a format is not a good candidate for long-haul transmission between two metropolitan networks. Therefore, a data format conversion from NRZ to return-to-zero (RZ) format is necessary. In general, such a conversion is carried out by using an optical electronic optical (OEO) conversion. The OEO conversion has some drawbacks such as small electronic bandwidth of available ICs, complexity, and high cost. To overcome these problems, an all-optical (OOO) conversion is proposed to release the issue of the speed bottleneck due to the limited bandwidth of ICs. Several all-optical NRZ-to-RZ format converter are proposed including a nonlinear active loop mirror (NALM), a cross-gain compression-based wavelength converter, a nonlinear optical loop mirror (NOLM), a cross-phase modulation based single travelling wave semiconductor laser amplifier (TWSLA), a gain-modulated semiconductor optical amplifier (SOA), self-phase modulation

(SPM) of SOA, a dual-wavelength injection locking in a FPLD, a cross-phase modulation in an SOA-based Mach-Zehnder interferometric wavelength converter, an optoelectronic oscillator, the transverse-magnetic mode absorption and SPM in a FPLD, an injection-locked FPLD at un-lasing condition, an SOA-loop-mirror, a Mach-Zehnder delay interferometer, and a dark-optical-comb injected SOA. Among these techniques, an NRZ-to-RZ format converter by using a semiconductor laser is a potential candidate due to its low cost. In 2002, Chow *et al.* demonstrated an all-optical NRZ-to-RZ data format conversion by using dual injection locking technique in a Fabry-Perot laser diode (FPLD). In 2004, Jeong *et al.* demonstrated an all-optical NRZ-to-RZ data format conversion for further clock extraction by using the transverse-magnetic mode absorption and self-phase modulation (SPM) in a FPLD. In my dissertation, we demonstrate an all-optical NRZ-to-RZ data format converter by adding a modulation current with appropriate amplitude to synchronously modulate the FPLD. By applying a injection-locking-induced threshold current reduction, an injection-locking-induced gain-switching is realized. That is, when the synchronously modulated FPLD receives the incoming NRZ data stream with bit one ('1'), the FPLD will change from un-lasing condition into gain-switching operation. Therefore, an all-optical NRZ-to-RZ data format converter is carried out. Furthermore, by operating the FPLD-based NRZ-to-RZ data format converter with larger modulation amplitude than threshold condition, an all-optical OR gate is also demonstrated in the dissertation. With strong injection locking, the injection-locking-induced RZ data has characteristics such as single mode operation, high side mode suppression ratio, enhanced modulation bandwidth, low chirp, and low timing jitter etc.

To realize soliton transmission, a gain-switched pulse with red chirping must be compensated to a transform-limited pulse. By using a spectral windowing, linear dispersion compensation, and a preemphasis technique, a scenario proposed by Nakazawa *et al.* provides a possible way to transmit the converted RZ-formatted data.

## 6.2 Suggestions for Future Work

There are several possible directions for future work:

1. The investigation of the threshold current reduction in vertical cavity surface emitting lasers (VCSELs) is a promising way due to its low threshold current, which implies that the required RF modulation amplitude can be greatly reduced.
2. By using dual-wavelength injection locking technique in another FPLD or SOA-based wavelength converters, a TDM-to-WDM function can be realized.
3. A soliton transmission experiment can be constructed for evaluation of the converted RZ-formatted data via a scenario of the dynamic soliton transmission.
4. Numerical analysis can answer which type of semiconductor laser is suitable for such a NRZ-to-RZ data format converter.



## References

- [1] G. P. Agrawal, and N. K. Dutta, *Long-wavelength Semiconductor Lasers*, New York: Van Nostrand Reinhold, 1986.
- [2] A. L. Schawlow, and C. H. Townes, "Infrared and optical masers," *Phys. Rev.* **112**, 1940 (1958).
- [3] T. H. Maiman, "Stimulated optical radiation in ruby masers," *Nature* **187**, 493 (1960).
- [4] A. Javan, W. R. Bennett, Jr., and D. R. Herriot, "Population inversion and continuous optical maser oscillation in a gas discharge containing an HeNe mixture," *Phys. Rev. Lett.* **6**, 106 (1961).
- [5] N. G. Basov, O. N. Krokhin, and Yu. M. Popov, *Sov. Phys. JETP* **13**, 1320 (1961).
- [6] M. G. A. Bernard, and G. Duraffourg, *Phys. Status Solidi* **1**, 699 (1961).
- [7] W. P. Dumke, "Interband Transitions and Maser Action," *Phys. Rev.* **127**, 1559 (1962).
- [8] R. N. Hall, G. E. Fenner, J. D. Kingsley, T. J. Soltys, and R. O. Carlson, "Coherent Light Emission from GaAs Junctions," *Phys. Rev. Lett.* **9**, 366 (1962).
- [9] M. I. Nathan, W. P. Dumke, G. Burns, F. H. Dill, Jr., and G. Lasher, "Stimulated Emission of Radiation from GaAs *p-n* Junctions," *Appl. Phys. Lett.* **1**, 62 (1962).
- [10] T. M. Quist, R. H. Rediker, R. J. Keyes, W. E. Krag, B. Lax, A. L. McWhorter, and H. J. Zeiger, "Semiconductor Maser of GaAs," *Appl. Phys. Lett.* **1**, 91 (1962).
- [11] N. Holonyak, Jr., and S. F. Bevacqua, "Coherent (visible) Light Emission from Ga(As<sub>1-x</sub>P<sub>x</sub>) Junctions," *Appl. Phys. Lett.* **1**, 82 (1962).
- [12] H. Kroemer, "A Proposed Class of Hetero-junction Injection Lasers," *Proc. IEEE* **51**, 1782 (1963).
- [13] Zh. I. Alferov, and R. F. Kazarinov, "Semiconductor Laser with Electrical Pumping," Authors certificate 181737 (U.S.S.R.), 1963.

- [14] H. Kressel, and H. Nelson, "Close-confinement Gallium Arsenide p-n Junction Lasers with Reduced Optical Loss at Room Temperature," *RCA Rev.* **30**, 106 (1969).
- [15] I. Hayashi, M. B. Panish, and P. W. Foy, "A Low-threshold Room-temperature Injection Laser," *IEEE J. Quantam Electron.* **QE-5**, 211 (1969).
- [16] Zh. I. Alferov, V. M. Andreev, E. L. Portnoi, and M. K. Trukan, "AlAs-GaAs Heterojunction Injection Lasers with a Low Room-Temperature Threshold," *Sov. Phys. Semicond.* **3**, 1107 (1970). [Translated from *Fiz. Tekh. Poluprovodn.* **3**, 1328 (1969)].
- [17] H. Rupprecht, J. M. Woodall, and G. D. Pettit, "Efficient Visible Electroluminescence at 300°K from Ga<sub>1-x</sub>Al<sub>x</sub>As p-n Junctions Grown by Liquid-phase Epitaxy," *Appl. Phys. Lett.* **11**, 81 (1967).
- [18] I. Hayashi, M. B. Panish, P. W. Foy, and S. Sumski, "Junction Lasers which Operate Continuously at Room Temperature," *Appl. Phys. Lett.* **17**, 109 (1970).
- [19] Zh. I. Alferov, V. M. Andreev, D. Z. Garbuzov, Yu. V. Zhilyaev, E. P. Morozov, E. L. Portnoi, and V. G. Trofim, "Effect of AlAs-GaAs Heterostructure Parameters on Threshold Current of Lasers and the Achievement of cw Generation at Room Temperature," *Sov. Phys. Semicond.* **4**, 1573 (1971). [Translated from *Fiz. Tekh. Poluprovodn.* **4**, 1826 (1970)].
- [20] M. Ettenberg, "Very Low-threshold Double-heterojunction Al<sub>x</sub>Ga<sub>1-x</sub>As Injection Lasers," *Appl. Phys. Lett.* **27**, 652 (1975).
- [21] J. C. Dymant, "Hermite-gaussian Mode Patterns in GaAs Junction Lasers," *Appl. Phys. Lett.* **10**, 84 (1967).
- [22] J. E. Ripper, J. C. Dymant, L. A. D'Asaro, and T. L. Paoli, "Stripe-geometry Double Heterostructure Junction Lasers: Mode Structure and cw Operation above Room Temperature," *Appl. Phys. Lett.* **18**, 155 (1971).

- [23] D. D. Cook, and F. R. Nash, "Gain-induced Guiding and Astigmatic Output Beam of GaAs Lasers," *J. Appl. Phys.* **46**, 1660 (1975).
- [24] H. Kressel, and J. K. Butler. *Semiconductor Lasers and Heterojunction LEDs*. New York: Academic Press, 1977.
- [25] H. C. Casey, Jr., and M. B. Panish. *Heterostructure Lasers*, Parts A and B. New York: Academic Press, 1978.
- [26] G. H. B. Thompson, *Physics of Semiconductor Laser Devices*. Chichester: John Wiley & Sons, 1980.
- [27] R. D. Dupuis, *J. Crys. Growth* **55**, 213 (1981).
- [28] A. Y. Cho, *J. Vac. Sci. Tech.* **16**, 275 (1979).
- [29] R. Dingle, W. Wiegmann, and C. H. Henry, "Quantum States of Confined Carriers in Very Thin  $\text{Al}_x\text{Ga}_{1-x}\text{As}$ -GaAs- $\text{Al}_x\text{Ga}_{1-x}\text{As}$  Heterostructures," *Phys. Rev. Lett.* **33**, 827 (1974); W. T. Tsang, C. Weisbuch, R. C. Miller, and R. Dingle, "Current Injection GaAs- $\text{Al}_x\text{Ga}_{1-x}\text{As}$  Multi-quantum-well Heterostructure Lasers Prepared by Molecular Beam Epitaxy," *Appl. Phys. Lett.* **35**, 673 (1979).
- [30] D. R. Scifres, W. Streifer, and R. D. Burnham, "Phase-locked Semiconductor Laser Array," *Appl. Phys. Lett.* **33**, 1015 (1978).
- [31] D. R. Scifres, C. Lindstrom, R. D. Burnham, W. Streifer, and T. L. Paoli, "Phase-locked. (GaAl)As Laser Diode Emitting 2.6 W CW from a Single Mirror," *Electron. Lett.* **19**, 169 (1983).
- [32] Y. Suematsu, "Long-wavelength Optical Fiber Communication," *Proc. IEEE* **71**, 692 (1983); T. Li, "Advances in Optical Fiber Communications: An Historical Perspective," *IEEE J. Sel. Areas Commun.* **SAC-1**, 356 (1983).
- [33] R. L. Moon, G. A. Antypas, and L. W. James, *J. Electron. Mater.* **3**, 635 (1974).
- [34] A. P. Bogatov, L. M. Dolginov, P. G. Eliseev, M. G. Mil'vidskii, B. N. Sverdlov, and

- E. G. Shevchenko, *Sov. Phys. Semicond.* **9**, 1282 (1975).
- [35] J. J. Hsieh, J. A. Rossi, and J. P. Donnelly, "Room-temperature cw Operation of GaInAsP/InP Double-heterostructure Diode Lasers Emitting at 1.1  $\mu\text{m}$ ," *Appl. Phys. Lett.* **28**, 709 (1976).
- [36] K. Oe, S. Ando, and K. Sugiyama, "1.3  $\mu\text{m}$  CW Operation of GaInAsP/InP DH Diode Lasers at Room Temperature," *Jpn. J. Appl. Phys.* **16**, 1273 (1977).
- [37] M. Horiguchi, and H. Osani, "Spectral Losses of Low-OH-Content Optical Fibers," *Electron. Lett.* **12**, 310 (1976).
- [38] T. Miya, Y. Terunuma, T. Hosaka, and T. Miyoshita, "Ultimate Low-loss Single-mode fibre at 1.55  $\mu\text{m}$ ," *Electron Lett.* **15**, 106 (1979).
- [39] N. Kobayashi, and Y. Horikoshi, "1.5  $\mu\text{m}$  InGaAsP/InP DH Laser with Optical Waveguide Structure," *Jpn. J. Appl. Phys.* **18**, 1005 (1979).
- [40] S. Akiba, K. Sakai, Y. Matsushima, and T. Yamamoto, "Room-temperature CW Operation of InGaAsP-InP Heterostructure Lasers Emitting at 1.56  $\mu\text{m}$ ," *Electron. Lett.*, 606 (1979).
- [41] G. D. Henshall, and P. D. Greene, "Low-threshold (Ga,In)(As,P) DH Lasers Emitting at 1.55  $\mu\text{m}$  Grown by LPE," *Electron Lett.* **15**, 621 (1979).
- [42] H. Kawaguchi, T. Takahei, Y. Toyoshima, H. Nagai, and G. Iwane, "Room-temperature CW Operation of InGaAsP-InP Double Heterostructure Diode-lasers Emitting at 1.55  $\mu\text{m}$ ," *Electron. Lett.* **15**, 669 (1979).
- [43] I. P. Kaminow, R. E. Nahory, M. A. Pollack, L. W. Stulz, and J. C. Dewinter, "Single-mode CW ridge-waveguide laser emitting at 1.55  $\mu\text{m}$ ," *Electron. Lett.* **15**, 763 (1979).
- [44] S. Arai, M. Asada, Y. Suematsu, and Y. Itaya, "Room Temperature CW Operation of GaInAsP/InP DH Laser Emitting at 1.51  $\mu\text{m}$ ," *Jpn. J. Appl. Phys.* **18**, 2333 (1979).

- [45] D. Botez, and G. Herskowitz, "Components for Optical Communications Systems: A Review," *Proc. IEEE* **68**, 689 (1980).
- [46] Y. Suematsu, K. Iga, and K. Kishino, in *GaInAsP Alloy Semiconductors*, ed. T. P. Pearsall. New York: John Wiley & Sons, 1982.
- [47] R. J. Nelson, and N. K. Dutta, in *Semiconductor and Semimetals*, Vol. 22, Part C, ed. W. T. Tsang. New York: Academic Press, 1985.
- [48] P. K. Runge, and P. R. Trischitta, "The SL Undersea Lightwave System," *J. Lightwave Tech.* **LT-2**, 744 (1984).
- [49] S. M. Sze, *Physics of Semiconductor Devices*, Second Ed. New York: John Wiley & Sons, 1981.
- [50] S. Bigo, E. Desurvire, S. Gauchard, and E. Brun, "Bit-rate enhancement through optical NRZ-to-RZ conversion and passive time-division multiplexing for soliton transmission systems," *Electron. Lett.* **30**, 984 (1994).
- [51] A. Sano, Y. Miyamoto, T. Kataoka, H. Kawakami, and K. Hagimoto, "10 Gbit/s 300 km repeaterless transmission with SBS suppression by the use of the RZ format," *Electron. Lett.* **30**, 1694 (1994).
- [52] S. Bigo, E. Desurvire and B. Desruelle, "All-optical RZ-to-NRZ format conversion at 10 Gbit/s with nonlinear optical loop mirror," *Electron. Lett.* **30**, 1868 (1994).
- [53] D. Norte and A. E. Willner, "Experimental demonstrations of all-optical conversions between the RZ and NRZ data formats incorporating noninverting wavelength shifting leading to format transparency," *IEEE Photon. Technol. Lett.* **8**, 712 (1996).
- [54] S.-G. Park, L. H. Spiekman, M. Eiselt, and J. M. Wiesenfeld, "Chirp consequences of all-optical RZ to NRZ conversion using cross-phase modulation in an active semiconductor photonic integrated circuit," *IEEE Photon. Technol. Lett.* **12**, 233 (2000).



- [55] L. Xu, B. C. Wang, V. Baby, I. Glesk, and P. R. Prucnal, "Performance-improved all-optical RZ to NRZ format conversion using duplicator and wavelength converter," *Opt. Commun.* **206**, 77 (2002).
- [56] C. W. Chow, C. S. Wong, H. K. Tsang, "All-optical RZ to NRZ data format and wavelength conversion using an injection locked laser," *Opt. Commun.* **223**, 309 (2003).
- [57] S. H. Lee, K. K. Chow, and C. Shu, "Spectral filtering from a cross-phase modulated signal for RZ to NRZ format and wavelength conversion," *Opt. Express* **13**, 1710 (2005).
- [58] Z. Jiang, D. E. Leaird, A. M. Weiner, "Width and wavelength-tunable optical RZ pulse generation and RZ-to-NRZ format conversion at 10 GHz using spectral line-by-line control," *IEEE Photon. Technol. Lett.* **17**, 2733 (2005).
- [59] A. D. Ellis and D. A. Cleland, "Ultrafast all optical switching in two wavelength amplifying nonlinear optical loop mirror," *Electron. Lett.* **28**, 405 (1992).
- [60] J. P. R. Lacey, M. V. Chan, R. S. Tucker, A. J. Lowery and M. A. Summerfield, "All-optical WDM to TDM transmultiplexer," *Electron. Lett.* **30**, 1612 (1994).
- [61] S. Bigo, E. Desurvire, S. Gauchard and E. Brun, "Bit-rate enhancement through optical NRZ-to-RZ conversion and passive time-division multiplexing for soliton transmission systems," *Electron. Lett.* **30**, 984 (1994).
- [62] H. K. Lee, K. H. Kim, J. T. Ahn, M.-Y. Jeon, and E.-H. Lee, "All-optical format conversion from NRZ to RZ signals using a walk-off balanced nonlinear fibre loop mirror," *Electron. Lett.* **32**, 2335 (1996).
- [63] L. Noel, X. Shan and A. D. Ellis, "Four WDM channel NRZ to RZ format conversion using a single semiconductor laser amplifier," *Electron. Lett.* **31**, 277 (1995).

- [64] D. Norte and A. E. Willner, "Demonstration of an all-optical data format transparent WDM-to-TDM network node with extinction ratio enhancement for reconfigurable WDM networks," *IEEE Photon. Technol. Lett.* **8**, 715 (1996).
- [65] H. J. Lee, H. G. Kim, J. Y. Choi and H. K. Lee, "All-optical clock recovery from NRZ data with simple NRZ-to-PRZ converter based on self-phase modulation of semiconductor optical amplifier," *Electron. Lett.* **35**, 989 (1999).
- [66] C. W. Chow, C. S. Wong, H. K. Tsang, "All-optical NRZ to RZ format and wavelength converter by dual-wavelength injection locking," *Opt. Commun.* **209**, 329 (2002).
- [67] L. Xu, B. C. Wang, V. Baby, I. Glesk, and P. R. Prucnal, "All-optical data format conversion between RZ and NRZ based on a Mach-Zehnder interferometric wavelength converter," *IEEE Photon. Technol. Lett.* **15**, 308 (2003).
- [68] L. Huo, Y. Dong, C. Lou, and Y. Gao, "Clock extraction using an optoelectronic oscillator from high-speed NRZ signal and NRZ-to-RZ format transformation," *IEEE Photon. Technol. Lett.* **15**, 981 (2003).
- [69] J. Lasri, P. Devgan, V. S. Grigoryan, P. Kumar, "Multiwavelength NRZ-to-RZ conversion with significant timing-jitter suppression and SNR improvement," *Opt. Commun.* **240**, 293 (2004).
- [70] Y. D. Jeong, H. J. Lee, H. Yoo, and Y. H. Won, "All-optical NRZ-to-PRZ converter at 10 Gb/s based on self-phase modulation of Fabry-Perot laser diode," *IEEE Photon. Technol. Lett.* **16**, 1179 (2004).
- [71] Y.-C. Chang, Y.-H. Lin, J. H. Chen, and G.-R. Lin, "All-optical NRZ-to-PRZ format transformer with an injection-locked Fabry-Perot laser diode at unlasing condition," *Opt. Express* **12**, 4449 (2004).

- [72] G.-R. Lin, Y.-C. Chang, Y.-H. Lin, and J. H. Chen, "All-optical data format conversion in synchronously modulated single-mode Fabry-Perot laser diode using external injection-locking-induced nonlinear threshold reduction effect," *IEEE Photon. Technol. Lett.* **17**, 1307 (2005).
- [73] Y.-C. Chang and G.-R. Lin, "Injection-locking laser-diode-based OC-192 optical non-return-to-zero-to-return-to-zero OR logic gate," *Opt. Lett.* **30**, 2074 (2005).
- [74] C. G. Lee, Y. J. Kim, C. S. Park, H. J. Lee, and C.-S. Park, "Experimental demonstration of 10-Gb/s data format conversions between NRZ and RZ using SOA-loop-mirror," *J. Lightwave Tech.* **23**, 834 (2005).
- [75] J. Yu, G. K. Chang, J. Barry, and Y. Su, "40 Gbit/s signal format conversion from NRZ to RZ using a Mach-Zehnder delay interferometer," *Opt. Commun.* **248**, 419 (2005).
- [76] G.-R. Lin, Y.-C. Chang, and K.-C. Yu, "All-optical pulse data generation in a semiconductor optical amplifier gain controlled by a reshaped optical clock injection," *Appl. Phys. Lett.* **88**, 191114 (2006).
- [77] G.-R. Lin, K.-C. Yu, and Y.-C. Chang, "10 Gbit/s all-optical non-return to zero-return-to-zero data format conversion based on a backward dark-optical-comb injected semiconductor optical amplifier," *Opt. Lett.* **31**, 1376 (2006).
- [78] R. Medina, "Photons vs. electrons [all optical network]," *IEEE Potentials* **21**, 9 (2002).
- [79] L. Chusseau, E. Hemery, and J. M. Lourtioz, "Period doubling in directly modulated InGaAsP semiconductor lasers," *Appl. Phys. Lett.* **55**, 822-824 (1989).
- [80] Y. Matsui, S. Kutsuzawa, S. Arahira, Y. Ogawa, and A. Suzuki, "Bifurcation in 20-GHz gain-switched 1.55- $\mu\text{m}$  MQW lasers and its control by CW injection seeding," *IEEE J. Quantum Electron.* **34**, 1213-1223 (1998).

- [81] H. Yoo, Y. D. Jeong, Y. H. Won, M. Kang, and H. J. Lee, "All-optical wavelength conversion using absorption modulation of an injection-locked Fabry-Perot laser diode," *IEEE Photon. Technol. Lett.* **16**, 536-538 (2004).
- [82] V. D. Kurnosov, V. I. Magalyas, A. A. Pleshkov, L. A. Rivlin, V. G. Trukhan, and V. V. Tsvetkov, "Self-modulation of emission from an injection semiconductor laser" *JETP Lett.* **4**, 303 (1966).
- [83] Y. A. Drozhbin, Y. P. Zakharov, V. V. Nikitin, A. S. Semenov, and V. A. Yakovlev, "Generation of ultrashort light pulses by a GaAs semiconductor laser," *JETP Lett.* **5**, 143 (1967).
- [84] N. G. Basov, V. N. Morozov, V. V. Nikitin, and A. S. Semenov, "Investigation of GaAs laser radiation pulsation," *Soviet Physics-Semiconductors* **1**, 1305 (1968).
- [85] C. Lin, P. L. Liu, T. C. Damen, D. J. Eilenberger, and R. L. Hartman, "Simple picosecond pulse generation scheme for injection lasers," *Electron. Lett.* **16**, 600 (1980).
- [86] T. Kobayashi, A. Yoshikawa, A. Morimoto, Y. Aoki, and T. Sueta, "Generation of ultrashort optical pulses by pulse driving of a semiconductor diode laser," *Technical Digest Papers 11th Int. Quantum Electronics Conference*, Boston, June 1980, Paper W1.
- [87] E. O. Gobel, G. Veith, J. Kuhl, H.-U. Habermeier, K. Lubke, and A. Perger, "Direct gain modulation of a semiconductor laser by a GaAs picosecond optoelectronic switch," *Appl. Phys. Lett.* **42**, 25 (1983).
- [88] P. M. Downey, J. E. Bowers, R. S. Tucker, and E. Ageukum, "Picosecond dynamics of a gain-switched InGaAsP laser," *IEEE J. Quantum Electron.* **23**, 1039 (1987).
- [89] D. Bimberg, K. Ketterer, H. E. Scholl, and H. P. Vollmer, "Generation of 4 ps light pulses from directly modulated V-groove lasers," *Electron. Lett.* **20**, 343 (1984).

- [90] H. Ito, H. Yokoyama, S. Murata, and H. Inaba, "Picosecond optical pulse generation from an RF modulated AlGaAs DH diode laser," *Electron. Lett.* **15**, 738 (1979).
- [91] J. AuYeung, "Picosecond optical pulse generation at gigahertz rate by direct modulation of a semiconductor laser," *Appl. Phys. Lett.* **38**, 308 (1981).
- [92] E. P. Harris, "Spiking in current-modulated CW GaAs external cavity laser," *J. Appl. Phys.* **42**, 892 (1971).
- [93] V. N. Morozov, V. V. Nikitin, and A. A. Sheronov, "Self-synchronization of modes in a GaAs semiconductor injection laser," *JETP Lett.* **6**, 256 (1968).
- [94] R. L. Fork, B. I. Green, and C. V. Shank, "Generation of optical pulses shorter than 0.1 ps by colliding pulse mode locking," *Appl. Phys. Lett.* **38**, 671 (1981).
- [95] P. P. Vasil'ev and A. B. Sergeev, "Generation of bandwidth-limited 2 ps pulses with 100 GHz repetition rate from multi-segmented injection laser," *Electron. Lett.* **25**, 1049 (1989).
- [96] Y. K. Chen, M. C. Wu, T. Tanbun-Ek, R. A. Logan, and M. A. Chin, "Subpicosecond monolithic colliding-pulse mode-locked multiple quantum well lasers," *Appl. Phys. Lett.* **58**, 1253 (1991).
- [97] R. Lang, "Injection locking properties of a semiconductor laser," *IEEE J. Quantum Electron.* **18**, 976 (1982).
- [98] J.-I. Nishizawa and K. Ishida, "Injection-induced modulation of laser light by the interaction of laser diodes," *IEEE J. Quantum Electron.* **11**, 515 (1975).
- [99] R. Lang and K. Kobayashi, "Suppression of relaxation oscillation in the modulated output of semiconductor lasers," *IEEE J. Quantum Electron.* **12**, 520 (1977).
- [100] S. Kobayashi and T. Kimura, "Coherent of injection phase-locked AlGaAs semiconductor laser," *Electron. Lett.* **16**, 668 (1980).
- [101] S. Kobayashi, J. Yamada, S. Machida, and T. Kimura, "Single mode operation of 500

- Mbit/s modulated AlGaAs semiconductor laser,” *Electron. Lett.* **16**, 746 (1980).
- [102] S. Kobayashi and T. Kimura, “Injection locking in AlGaAs semiconductor laser,” *IEEE J. Quantum Electron.* **17**, 681 (1981).
- [103] K. Otsuka and S. Tarucha, “Theoretical studies on injection locking and injection-induced modulation of laser diodes,” *IEEE J. Quantum Electron.* **17**, 1515 (1981).
- [104] K. Kobayashi, H. Nishimoto, and R. Lang, “Experimental observation of asymmetric detuning characteristics in semiconductor laser injection locking,” *Electron. Lett.* **18**, 54 (1982).
- [105] L. Li, “A unified description of semiconductor lasers with external light injection and its application to optical bistability,” *IEEE J. Quantum Electron.* **30**, 1723 (1994).
- [106] S. Sivaprakasam and R. Singh, “Gain change and threshold reduction of diode laser by injection locking,” *Opt. Commun.* **151**, 253 (1998).
- [107] S. Kobayashi and T. Kimura, “Injection locking in AlGaAs semiconductor laser,” *IEEE J. Quantum Electron.* **17**, 681 (1981).
- [108] R. Lang, “Injection locking properties of a semiconductor laser,” *IEEE J. Quantum Electron.* **18**, 976 (1982).
- [109] S. Kobayashi, J. Yamada, S. Machida, and T. Kimura, “Single mode operation of 500 Mbit/s modulated AlGaAs semiconductor laser,” *Electron. Lett.* **16**, 746 (1980).
- [110] O. Lidoyne, P.B. Gallion, D. Eransme, “Modulation properties of an injection-locked semiconductor laser,” *IEEE J. Quantum Electron.* **27**, 344 (1991).
- [111] J. I. Nishizawa, K. Ishida, “Injection-induced modulation of laser light by the interaction of laser diodes,” *IEEE J. Quantum Electron.* **11**, 515 (1975).
- [112] P. Spano, S. Piazzolla, M. Tamburrini, “Frequency and intensity noise in injection-locked semiconductor lasers: Theory and experiments,” *IEEE J. Quantum*

- Electron.* **22**, 427 (1986).
- [113] L. Li, "Static and dynamic properties of injection-locked semiconductor lasers," *IEEE J. Quantum Electron.* **30**, 1701 (1994).
- [114] R. Hui, S. Benedetto, I. Montrosset, "Optical bistability in diode-laser amplifiers and injection-locked laser diodes," *Opt. Lett.* **18**, 287 (1993).
- [115] F. Srobar, "Feedback relationships and threshold current in semiconductor injection lasers: old problems revisited," *Opt. Quant. Electron.* **25**, 27 (1993).
- [116] W. Sharfin, M. Dagenais, "Dynamics of optically switched bistable diode laser amplifiers," *IEEE J. Quantum Electron.* **23**, 303 (1987).
- [117] L. Li, "A unified description of semiconductor lasers with external light injection and its application to optical bistability," *IEEE J. Quantum Electron.* **30**, 1723 (1994).
- [118] S. Sivaprakasam and R. Singh, "Gain change and threshold reduction of diode laser by injection locking," *Opt. Commun.* **151**, 253 (1998).
- [119] L. A. Coldren, and S. W. Corzine, *Diode Lasers and Photonic Integrated Circuits*, New York: Wiley Interscience, 1995.
- [120] K. Petermann, *Laser Diode Modulation and Noise*. Publishers Dordrecht, The Netherlands: Kluwer Academic, 1988 (corrected 1991).
- [121] F. Mogensen, H. Olesen, and G. Jacobsen, "Locking conditions and stability properties for a semiconductor laser with external light injection," *IEEE J. Quantum Electron.*, vol. QE-21, pp. 784-793, 1985.
- [122] R. Hui, A. D'Ottavi, A. Mecozzi, and P. Spano, "Injection locking in distributed feedback semiconductor lasers," *IEEE J. Quantum Electron.* **27**, 1688 (1991).
- [123] C. H. Henry, N. A. Olsson, and N. K. Dutta, "Locking range and stability of injection locked 1.54  $\mu\text{m}$  InGaAsP semiconductor lasers," *IEEE J. Quantum Electron.* **21**, 1152 (1985).

- [124] I. Petitbon, P. Gallion, G. Debarge, and C. Chabran, "Locking bandwidth and relaxation oscillations of an injection-locked semiconductor laser," *IEEE J. Quantum Electron.* **24**, 148 (1988).
- [125] B. R. Bennett, R. A. Soref, and J. A. Del Alamo, "Carrier-induced change in refractive index of InP, GaAs, and InGaAsP," *IEEE. J. Quantum Electron.* **26**, 113 (1990).
- [126] A. E. Siegman, *Lasers* (Oxford University Press, London, UK, 1986).
- [127] J. Horner and E. Patzak, "Large-signal analysis of all-optical wavelength conversion using two-mode injection-locking in semiconductor lasers," *IEEE Quantum Electron.* **33**, 596 (1997).
- [128] N. S. Patel, K. L. Hall, and K. A. Rauschenbach, *Opt. Lett.* **21**, 1466 (1996).
- [129] A. J. Poustie, K. J. Blow, A. E. Kelly, and R. J. Manning, *Opt. Commun.* **156**, 22 (1998).
- [130] T. Durhuus, B. Mikkelsen, C. Joergensen, S. L. Danielsen, and K. E. Stubkjaer, *J. Lightwave Technol.* **14**, 942 (1996).
- [131] L. Zucchelli, G. Bendelli, D. Raspollini, M. Puelo, P. Gambini, M. Schilling, W. Idler, and K. Wunstel, *CSELT Technical Reports* **25**, 357 (1997).
- [132] T. Fjelde, D. Wolfson, A. Kloch, C. Janz, A. Coquelin, I. Guillemot, F. Gaborit, F. Poingt, B. Dagens, and M. Renaud, *Electron. Lett.* **36**, 813 (2000).
- [133] C. Lin, T. P. Lee, and C. A. Burrus, "Picosecond frequency chirping and dynamic line broadening in InGaAsP injection lasers under fast excitation," *Appl. Phys. Lett.* **42**, 141 (1983).
- [134] T. L. Koch and R. A. Linke, "Effect of nonlinear gain reduction on semiconductor laser wavelength chirping," *Appl. Phys. Lett.* **48**, 613 (1986).
- [135] R. A. Linke, "Modulation induced transient chirping in single frequency lasers,"



- IEEE J. Quantum Electron.* **21**, 593 (1985).
- [136] A. Takada, T. Sugie, and M. Saruwatari, "High-speed picosecond optical pulse compression from gain-switched 1.3- $\mu\text{m}$  distributed feedback-laser diode (DFB-LD) through highly dispersive single-mode fiber," *Lightwave Tech.* **LT-5**, 1525 (1987).
- [137] J. D. Ralston, S. Weisser, I. Esquivias, E. C. Larkins, J. Rosenzweig, P. J. Tasker, J. Fleissner, "Control of differential gain, nonlinear gain and damping factor for high-speed application of GaAs-based MQW lasers," *IEEE J. Quantum Electron.* **29**, 1648 (1993).
- [138] Y. Matsui, H. Murai, S. Arahira, Y. Ogawa, A. Suzuki, "Enhanced modulation bandwidth for strain-compensated InGaAlAs-InGaAsP MQW lasers," *IEEE J. Quantum Electron.* **34**, 1970 (1998).
- [139] S. Piazzolla, P. Spano, M. Tamburrini, "Small signal analysis of frequency chirping in injection-locked semiconductor lasers," *IEEE J. Quantum Electron.* **22**, 2219 (1986).
- [140] G. Yabre, "Effect of relatively strong light injection on the chirp-to-power ratio and the 3 dB bandwidth of directly modulated semiconductor lasers," *J. Lightwave Technol.* **14**, 2367 (1996).
- [141] H. F. Chen, J. M. Liu, T. B. Simpson, "Response characteristics of direct current modulation on a bandwidth-enhanced semiconductor laser under strong injection locking," *Opt. Commun.* **173**, 349 (2000).
- [142] N. A. Olsson, H. Temkin, R. A. Logan, L. F. Johnson, G. J. Dolan, J. P. Van DerTiel, J. C. Campbell, "Chirp-free transmission over 82.5 km of single mode fibers at 2 Gbit/s with injection locked DFB semiconductor lasers," *J. Lightwave Technol.* **LT-3**, 63 (1985).
- [143] S. K. Hwang, J. M. Liu, "Dynamical characteristics of an optically injected

- semiconductor laser,” *Opt. Commun.* **183**, 195 (2000).
- [144] T. B. Simpson, J. M. Liu, “Enhanced modulation bandwidth in injection-locked semiconductor lasers,” *IEEE Photon. Technol. Lett.* **9**, 1322 (1997).
- [145] X. J. Meng, T. Chau, M. C. Wu, “Experimental demonstration of modulation bandwidth enhancement in distributed feedback lasers with external light injection,” *Electron. Lett.* **34**, 2031 (1998).
- [146] J. M. Liu, H. F. Chen, X. J. Meng, T. B. Simpson, “Modulation bandwidth, noise, and stability of a semiconductor laser subject to strong injection locking,” *IEEE Photon. Technol. Lett.* **9**, 1325 (1997).
- [147] Y. Okajima, S. K. Hwang, J. M. Liu, “Experimental observation of chirp reduction in bandwidth-enhanced semiconductor lasers subject to strong optical injection,” *Opt. Commun.* **219**, 357 (2003).
- [148] A. Hasegawa and F. Tappert, “Transmission of stationary nonlinear optical pulses in dispersive dielectric fibers. I. Anomalous dispersion,” *Appl. Phys. Lett.* **23**, 142 (1973).
- [149] L. F. Mollenauer and K. Smith, “Demonstration of soliton transmission over more than 4000 km in fiber with loss periodically compensated by Raman gain,” *Opt. Lett.* **13**, 675 (1988).
- [150] M. Nakazawa, Y. Kimura, and K. Suzuki, “Soliton amplification and transmission with Er<sup>3+</sup>-doped fibre repeater pumped by GaInAsP diode,” *Electron. Lett.* **25**, 199 (1989).
- [151] M. Nakazawa, Y. Kimura, and K. Suzuki, “Efficient Er<sup>3+</sup>-doped optical fiber amplifier pumped by a 1.48 μm InGaAsP laser diode,” *Appl. Phys. Lett.* **54**, 295 (1989).
- [152] M. Nakazawa, K. Suzuki, and Y. Kimura, “20-GHz soliton amplification and

- transmission with an  $\text{Er}^{3+}$ -doped fiber,” *Opt. Lett.* **14**, 1065 (1989).
- [153] M. Nakazawa, K. Suzuki, and Y. Kimura, “3.2-5 Gb/s, 100 km Error-Free Soliton Transmissions with Erbium Amplifiers and Repeaters,” *IEEE Photon. Technol. Lett.* **2**, 216 (1990).
- [154] M. Nakazawa, K. Suzuki, and Y. Kimura, “Generation and transmission of optical solitons in the gigahertz region using a directly modulated distributed-feedback laser diode,” *Opt. Lett.* **15**, 588 (1990).
- [155] M. Nakazawa, K. Suzuki, and Y. Kimura, “Transform-limited pulse generation in the gigahertz region from a gain-switched distributed-feedback laser diode using spectral windowing,” *Opt. Lett.* **15**, 715 (1990).
- [156] M. Nakazawa, Y. Kimura, K. Suzuki, and H. Kubota, “Wavelength multiple soliton amplification and transmission with an  $\text{Er}^{3+}$ -doped optical fiber,” *J. Appl. Lett.* **66**, 2803 (1989).
- [157] H.-F. Liu, Y. Ogawa, S. Oshiba, and T. Nonaka, “Picosecond pulse generation from a 1.3  $\mu\text{m}$  distributed feedback laser diode using soliton-effect compression,” *IEEE J. Quantum Electron.* **27**, 1655 (1991).
- [158] D. Marcuse, “Pulse distortion in single-mode fibers. 3: chirped pulses,” *Appl. Opt.* **20**, 3573 (1981).
- [159] M. Nakazawa, H. Kubota, K. Suzuki, E. Yamada, and A. Sahara, “Ultrahigh-speed long-distance TDM and WDM soliton transmission technologies,” *IEEE J. Sel. Top. Quantum Electron.* **6**, 363 (2000).

## 簡歷

姓名：張詠誠

生日：民國 65 年 1 月 24 日

出生地：台灣省彰化市

學歷：

學 校 / 科 系	學位	起訖年月
國立中山大學/電機系	學士	83 年 9 月 ~ 87 年 6 月
私立大同大學/光電所	碩士	87 年 9 月 ~ 89 年 6 月
國立交通大學/光電所	博士	91 年 9 月 ~ 95 年 6 月



(A) 著作目錄一期刊論文

SCI 與 EI 選錄期刊論文

SCI EI NO. Author/Title/Journal

- ❖ \* 16. Gong-Ru Lin, Yung-Cheng Chang, and Kun-Chieh Yu, "All-optical pulse data pattern transformation in a semiconductor optical amplifier gain controlled by a reshaped optical clock injection", *Applied Physics Letters*, Vol. 88, No. 19, 1-3, May 2006.
- ❖ \* 15. Gong-Ru Lin, Kun-Chieh Yu, and Yung-Cheng Chang, "10 Gbit/s all-optical non-return to zero-return-tozero data format conversion based on a backward dark-optical-comb injected semiconductor optical amplifier", *Optics Letters*, Vol. 31, No. 10, pp. 1376-1378, May 2006.
- ❖ \* 14. Tze-An Liu, Gong-Ru Lin, Yung-Cheng Chang, and Ci-Ling Pan, "A Wireless Audio and Burst Communication Link with Directly Modulated THz Photoconductive Antenna", *Optics Express*, Vol. 13, No. 22, pp., November 2005.
- ❖ \* 13. Gong-Ru Lin, Ming-Chung Wu, Yung-Cheng Chang, and Ci-Ling Pan, "Ultrahigh supermode noise suppressing ratio of a semiconductor optical amplifier bandpass filtered harmonically mode-locked Erbium-doped fiber laser", *Optics Express*, Vol. 13, No. 18, pp. 7215-7224, September 2005.
- ❖ \* 12. Yung-Cheng Chang and Gong-Ru Lin, "Optically gain-switched laser diode based 10Gbit/s all-optical data format converter", *Optics Letters*, Vol. 30, No. 16, pp. 2704-2706, August 2005.
- ❖ \* 11. Gong-Ru Lin, Ming-Chung Wu, and Yung-Cheng Chang, "Suppression of Phase and Supermode Noises in a Harmonic Mode-Locked Erbium-Doped Fiber Laser with a Semiconductor Optical Amplifier Based High-Pass Filter", *Optics Letters*, Vol. 30, No. 14, pp. 1834-1836, July 2005.
- ❖ \* 10. Gong-Ru Lin, Yung-Cheng Chang, Yu-Huang Lin, and J. H. Chen, "All Optical Data Format Conversion in Synchronously Modulated Single-Mode Fabry-Perot Laser Diode Using External Injection-Locking Induced Nonlinear Threshold Reduction Effect", *IEEE Photonics Technology Letters*, Vol. 17, No. 6, pp. 1307-1309, June 2005.
- ❖ \* 9. Yung-Cheng Chang, Yu-Huang Lin, Yu-Sheng Liao, and Gong-Ru Lin, "Switchable dual-wavelength NRZ-to-RZ data-format transformer using non-DC-biased and synchronously modulated laser diode", *IEICE Transactions on Electronics*, Vol. E88-C, No. 5, pp. 981-983, May 2005.
- ❖ \* 8. Gong-Ru Lin and Yung-Cheng Chang, "10 Gbit/s tunable dual-wavelength nonreturn-to-zero -to-return-to-zero data-format transformer based on a non-direct-current-biased Fabry-Perot laser diode", *Applied Optics*, Vol. 44, No. 15, pp. 3058-3062, May 2005.
- ❖ \* 7. Yung-Cheng Chang, Yu-Huang Lin, J. H. Chen, and Gong-Ru Lin, "All-optical NRZ-to-PRZ format transformer with an injection-locked Fabry-Perot laser diode at unlasing condition", *Optics Express*, Vol. 12, No. 19, pp. 4449-4456, September 2004.
- ❖ \* 6. Gong-Ru Lin, Jung-Rung Wu, and Yung-Cheng Chang, "Photonic millimeter-wave generation from frequency-multiplied Erbium-doped fiber laser pulse-train using purely sinusoidal-wave modulated laser diode", *Optics Express*, Vol. 12, No. 17, pp. 4166-4171, August 2004.
- ❖ \* 5. Gong-Ru Lin, J.-R. Wu, and Yung-Cheng Chang, "Rational Harmonic Mode-Locking of Erbium-Doped Fiber Laser at 40 GHz Using a Loss-Modulated Fabry Perot Laser Diode", *IEEE Photonics Technology Letters*, Vol. 16, No. 8, pp. 1810-1812, August 2004.
- ❖ \* 4. Gong-Ru Lin, Yu-Huang Lin, and Yung-Cheng Chang, "Theory and Experiments of a Mode Beating Noise Suppressed and Mutually Injection-Locked Fabry-Perot Laser Diode and Erbium-Doped Fiber Amplifier Link", *IEEE Journal of Quantum Electronics*, Vol. 40, No. 8, pp. 1014-1022, August 2004.
- ❖ \* 3. Gong-Ru Lin, Yung-Cheng Chang, Tze-An Liu, and Ci-Ling Pan, "Piezoelectric-transducer-based optoelectronic frequency synchronizer for control of pulse delay in a femtosecond passively mode-locked Ti:sapphire laser", *Applied Optics*, Vol. 42, No. 15, pp. 2843-2848, May 2003. 國科會補助編號 NSC 90-2215-E-027-008
- ❖ \* 2. Gong-Ru Lin and Yung-Cheng Chang, "Phase-Locked-Loop-Based Delay-Line-Free Picosecond Electro-Optic Sampling System", *Review of Scientific Instruments*, Vol. 74, No. 4, pp. 2255-2261, April 2003. 國科會補助編號 NSC 90-2215-E-027-008
- ❖ \* 1. Gong-Ru Lin and Yung-Cheng Chang, "A Novel Electro-Optic Sampling System with an Optoelectronic Phase-Locked Phase Shifter as a Delay-Time Controller", *Japanese Journal of Applied Physics*, Part. 1, Vol. 41, No. 10, pp. 6003-6006, October 2002. 國科會補助編號 NSC90-2215-E-027-008